

ABSTRACT

Title of dissertation: **EXPERIMENTAL CHARACTERIZATION OF
LASER-INDUCED PLASMAS AND APPLICATION
TO GAS COMPOSITION MEASUREMENTS**

Francesco Ferioli, Doctor of Philosophy, 2005

Dissertation directed by: **Professor Steven G. Buckley
Department of Mechanical Engineering**

In this dissertation new applications of Laser Induced Breakdown Spectroscopy (LIBS) are investigated. When a powerful laser beam is focused to a high enough fluence breakdown occurs and a hot, short-lived plasma is formed. In the first part of this dissertation, an experimental study of laser plasmas generated in air and argon is presented. The breakdown is investigated starting from the formation of the plasma, through the subsequent phase of adiabatic expansion, until the final decay. The results are interpreted on the basis of an hydrodynamic model that describes the plasma as a strong shock wave propagating through the fluid. Simple dimensional and energy considerations allow derivation of the general scaling laws that govern the regimes of motion. The time and length scales appropriate to describe the motion of the fluid at different stages are defined and, for every regime, the comparison between experimental observations and theory is presented. The proposed model appears to be consistent with the observations, and the theory outlined in the paper can be used to derive estimates of the fluid properties.

In the second part of the dissertation, atomic emission from the plasma is used to perform direct measurements of atomic species in mixtures of hydrocarbons and air. Atomic emission from the laser-induced plasma is observed and ratios of elemental lines are used to infer composition in reactants and in flames. Equivalence ratio can be determined from the spectra obtained from a single shot of the laser, avoiding time averaging of signals with a spatial resolution on the order of a few mm. The strength of the C, O, and N lines in the 700 - 800 nm spectral window is investigated for binary mixtures of C_3H_8 , CH_4 , and CO_2 in air. The dependence of the atomic emission on the concentration of carbon and hydrogen is investigated, as well as the influence of experimental parameters such as the laser power and the temporal gating of the detector.

Finally the technique is demonstrated on a reciprocating engine. The measurements on the engine provide insight into the sensitivity that may be achieved in real-world applications. It is demonstrated that the precision of the measurements can be enhanced using the statistical technique of principal component analysis.

EXPERIMENTAL CHARACTERIZATION OF
LASER-INDUCED PLASMAS AND APPLICATION
TO GAS COMPOSITION MEASUREMENTS

by

Francesco Ferioli

Dissertation submitted to the Faculty of the Graduate School of the
University of Maryland, College Park in partial fulfillment
of the requirements for the degree of
Doctor of Philosophy
2005

Advisory Committee:

Associate Professor Steven G. Buckley, Chair/Advisor
Associate Professor Kenneth T. Kiger
Associate Professor Ken Yu
Assistant Professor Andre W. Marshall
Professor Richard V. Calabrese

© Copyright by
Francesco Ferioli
2005

To Federica

ACKNOWLEDGMENTS

I'm sincerely thankful to the many people that helped make this work possible. Professor Paul Puzinauskas from the University of Alabama for his invaluable help with the engine measurements. Dr. Sivanandan Harilal from the Center for Energy Research of the University of California San Diego, for his advice on measuring plasma radiation as well as for the access to his unpublished images of the plasma. David Hoffmann, for his support performing shadowgraphy, and Dr. Farahat Beg for helping measuring extreme U.V. radiation.

Finally I wish to thank my advisor, professor Steven G. Buckley for his mentoring and the University of Modena e Reggio Emilia for its support and funding throughout these years.

Contents

1	Introduction	1
1.1	Scope of the present work	1
1.2	Motivation and background	3
1.3	Outline of the manuscript	5
2	Experimental Study of the Laser-Induced Breakdown	7
2.1	Introduction	7
2.2	Measurement of the Radiated Energy	11
2.3	The Laser Supported Wave	13
2.3.1	Dimensional analysis of the laser supported wave	15
2.3.2	Maximum plasma temperature and average plasma temperature	21
2.4	Post Breakdown Evolution	27
2.4.1	The idealized point explosion	31
2.4.2	The self-similar region: comparison with the experimental re- sults	35
2.4.3	The numerical solution: comparison with the experiments . . .	38
2.5	Later Stages of the Expansion	44

2.6	Radiation from the Plasma	47
2.6.1	Spontaneous emission from a hot plasma	49
2.6.2	Lifetime of the atomic emission	51
2.7	Conclusions	54
3	Spectroscopic Measurements of Hydrocarbons	58
3.1	Optical Measurements of Gas Composition	58
3.2	Method	59
3.3	Spectroscopic Measurements of the Equivalence Ratio	62
3.3.1	LIBS Measurements in a Combustible Mixture	64
3.3.2	Effect of laser pulse energy on atomic emission	69
3.3.3	Lifetime of the atomic emission as a function of laser pulse energy	71
3.3.4	Quenching of atomic emission via radiationless transitions . . .	74
3.4	Conclusions	81
4	Real Time Measurement of the Fuel-to-Air ratio	83
4.1	Measurements on a Reciprocating Engine	83
4.2	Engine Setup	85
4.3	Real Time Exhaust Gas Measurements	87
4.4	Chemometric Analysis of LIBS Spectra	90
4.5	Conclusions	93
5	Future Work	96

5.1	An Outline for Future Research	96
5.2	Extreme U.V. Emission from the Laser-Induced Plasma	97
5.3	Shock Wave Effect on a Dense Aerosol	99
5.3.1	Drag of a nanometer-sized particle in a spherical shock wave	101
5.3.2	Particle trajectory in a spherical shock wave	103
5.3.3	Implications for Aerosol Measurements	106
6	Conclusions	108
6.1	Summary of the Present Work	108
6.2	Experimental Study of Laser Plasmas	108
6.3	Measurements of Hydrocarbons	111
A	Experimental Setup	113
A.1	Measurement of the Radiated Energy	113
A.2	Shadowgraphy Setup	115
A.3	Spectroscopic measurements of the equivalence ratio	117
A.4	Engine experiments	119

List of Tables

2.1	Energy Radiated by Laser Plasmas in Air	12
2.2	Position of the Shock Wave as a Function of Time, Numerical Simulation	34
4.1	Combinations of Spectral Features that can be Related to Φ	91

List of Figures

2.1	Image of the Laser Plasma in Argon	14
2.2	Scaling of the Laser Spark in Argon	17
2.3	Scaling of the Laser Spark in Air	18
2.4	More Images of the Laser Spark in Air	19
2.5	Lateral Expansion of the Plasma	20
2.6	Contour of the Plasma in Air	22
2.7	Contour of the Plasma in Argon	22
2.8	Volume of the Plasma as a Function of the Laser Pulse Energy	23
2.9	Plasma Temperature as a Function of Laser Pulse Energy	26
2.10	Images of the First Instants of the Plasma Expansion	29
2.11	Evolution of the Shock Wave Generated by the Laser Breakdown in Air	30
2.12	Position of the Shock Wave in Time in the Self-Similar Region	36
2.13	Ratio of the Length Scales $\frac{r_0}{r_a}$	38
2.14	Profiles of Velocity Behind the Shock Wave at Different Times	40
2.15	Shock Position in Time, Comparison with the Numerical Solution	41

2.16 Region Studied Experimentally and the Whole Extent of the Numerical solution	41
2.17 Shock Radius at Different Energies, Comparison with the Numerical Solution	42
2.18 Shock Propagation in Argon	42
2.19 Flow Field Behind the Shock Wave at Different Times	43
2.20 Onset of Instability in the Hot Fluid	45
2.21 Final Distribution of Temperature and Internal Energy in Air	46
2.22 X-ray and Extreme UV Radiation Emitted from the Plasma	48
2.23 Emission Spectrum of the Balmer- α Line of Hydrogen	51
2.24 Evolution in Time of the Balmer- α Line of Hydrogen	52
2.25 Intensity of the H and N Lines as a Function of Time	53
2.26 Normalized Intensity of the 656 nm H Line	53
3.1 Emission Spectrum in the 690-790 nm Region	61
3.2 Single Shot Gas Composition Measurements	63
3.3 Transmitted Laser Pulse Energy as a Function of Propane Concentration	66
3.4 Averaged LIBS Signal as a Function of the Mole Fraction of Propane	67
3.5 Absolute Intensity of the N Line as a Function of Laser Pulse Energy	69
3.6 Ratio of Atomic Lines (C/N+O) as a Function of Laser Pulse Energy	70
3.7 Ratio of the Normalized C to N Spectral Lines as a Function of Time	72
3.8 LIBS Measurements Taken in a Flame	73

3.9	Effect of Propane Concentration on the Lifetime of the N Atomic Line	75
3.10	Intensity of the N, O and C Lines as a Function of C ₃ H ₈ Concentration	76
3.11	Comparison Between Methane, Propane and Helium	77
3.12	Comparison of the Emission Spectra of methane and carbon dioxide .	78
3.13	Ratio of the C to N Lines as a Function of the Mole Fraction of CH ₄ and CO ₂	79
3.14	N and O Line Intensities as a Function of the Equivalence Ratio for CH ₄ and C ₃ H ₈	80
4.1	Ratio of the Spectral Lines as a Function of the Engine Equivalence Ratio	84
4.2	Comparison of the Single Shot Spectra	86
4.3	Ratio of the N and O Line to the C Line as a Function of Φ	88
4.4	Single Shot LIBS Spectrum from the Engine Exhaust	89
4.5	LIBS Measurements Plotted in Function of the Principal Components	92
4.6	Principal Component Analysis of LIBS Spectra	94
5.1	X-ray and E.U.V. Plasma Radiation for Different Pulse Energies	97
5.2	X-ray Emission from a Laser Plasma	98
5.3	Shock Wave-Induced Coagulation of an Aerosol	99
5.4	Trajectory of a Nanometer-Sized Particle in the Shock Wave	103
5.5	Relative Reynolds and Mach Numbers for Particle Through the Shock Wave	104
5.6	Displacement of an 800 nm Particle in the Shock Wave	105

A.1 Measurement of the Radiated Energy: Experimental Setup	114
A.2 Setup for Shadowgraphy	115
A.3 Setup for gas Composition Measurements	117
A.4 Setup for Measurements on the Engine	120

LIST OF SYMBOLS

A_{ik}	Einstein spontaneous transition coefficient, s^{-1}
c_{ij}	Number of collisions between particles i and j
c_p	Specific heat at constant pressure, J/kgK
c_v	Specific heat at constant volume, J/kgK
C	Cunningham coefficient
d	Particle diameter, m
D	Velocity of the shock wave, m/s
E	Energy, J
q_i	Degeneracy of the state i
h	Enthalpy, J; Planck constant, Js
J_0	Light flux, J/m^2s
k	Boltzmann constant, J/K
kn	Knudsen number
I_{ik}	Radiant power, W
n	Number concentration
N	Number per unit volume, m^{-3}
P_{ik}	Transition probability
p	Pressure, N/m^2
r	Radius of the spherical shock wave, m
r_0	Characteristic length of the laser wave, m
r_a	Acoustic radius, m

T	Temperature, K
t	Time, s
t_0	Duration of the laser pulse, s
t_a	Acoustic time, s
u	Fluid velocity, m/s
v	Particle velocity, m/s
\mathbb{V}	Non-dimensional volume of the plasma
\mathbf{V}	Volume of the plasma, m^3
W_q	Ionization probability
Z	Partition function

Greek Letters

β	Lateral expansion of the plasma, experimental constant
γ	Ratio of the specific heats
δ	Experimental exponent, internal energy of the fluid
ϵ	Internal energy, J/kg
θ	Angle
λ	Mean free path, m
μ	Dynamic viscosity, kgm^2/s^2
ν	Kinematic viscosity, m^2/s
ξ	Similarity variable for the point explosion
ρ	Density, kg/m^3
σ	Experimental coefficient, energy coupling into the shock wave

ν	Frequency, s^{-1}
ϕ	Angle
Φ	Equivalence ratio (normalized air to fuel ratio)
χ	Thermal diffusivity, m^2/s
ζ	Experimental exponent, internal energy of the fluid
ω	Angular frequency, s^{-1}

Chapter 1

Introduction

1.1 Scope of the present work

This dissertation discusses the application of Laser Induced Breakdown Spectroscopy (LIBS) to the analysis of combustion processes. LIBS is a plasma spectroscopy technique that employs the focused radiation of a relatively high peak power laser pulse to produce a hot plasma in the medium to be analyzed. As the plasma cools, electrons decay from excited quantum levels, emitting energy in the form of monochromatic radiation. The position of the atomic emission lines depends on the energy gap between the quantum levels involved in the transition and, therefore, on the electronic structure of the atoms. If the light coming from the plasma is spectrally resolved, the position of the atomic lines allows detection of the elements present in the target medium. The intensity of the atomic lines depends, among other things, on the number of atoms present and therefore on the concentration of the analyte. LIBS has been used as an analytical technique for more than thirty years and ap-

plied to gas, solid and liquid targets [1, 2, 3, 4]. The unique advantages of LIBS over other diagnostic techniques is the ability to provide real-time measurements with almost no sample preparation. LIBS has been applied to most of the elements on the periodic table and the detection limits are on the order of parts-per-million on a mass basis for most atoms. Detection limits are highly dependent on the matrix and on the plasma parameters. Despite extensive research, possible applications of LIBS to the fields of combustion and fluid dynamics are still largely unexplored and will be the subject of the present work.

In this dissertation a new method to optically measure optically the fuel-to-air ratio in a combustible mixture is developed. A pulsed laser is focused in a mixture of air and hydrocarbons and the emission lines of carbon, nitrogen and oxygen are detected simultaneously to quantify the fuel-to-air ratio. In order to investigate the potential of LIBS as a diagnostic tool for combustion, the technique is demonstrated both in a laboratory setup and on a reciprocating engine. Due to the strength of the emission from the plasma, the proposed technique proves to have an excellent signal-to-noise ratio. The main problems encountered during the experiments concern reproducibility and quantification of the results. The concentration of a chemical element in the plasma is only one of many factors influencing the strength of an atomic line. For this reason, measuring concentration from the strength of spectral lines alone is often a complex task.

In order to improve the accuracy of LIBS for measuring hydrocarbons, a detailed study of the main factors influencing the measurements is carried out. The research is two-pronged: the basic physics responsible for the formation, expan-

sion and recombination of the plasma are investigated, and then the influence of the experimental parameters more relevant to measurements of hydrocarbons are discussed.

1.2 Motivation and background

Methods of quickly and rapidly measuring gas composition in combustion systems are of great practical interest. In particular, optical techniques can be used effectively in many situations where intrusive measurements are not convenient. The real-time, in situ nature of many optical measurement techniques make them amenable to control applications requiring on-line data streams, while simultaneously avoiding probe effects that may perturb the sample. In combustion processes, fuel efficiency and emission of pollutants depends dramatically on the local fuel-to-air ratio. For this reason, time-resolved measurements of fuel/air distributions may be used to improve existing combustion systems. Raman spectroscopy is widely used to measure turbulent mixing of fuel and oxidizer in nonpremixed flames [5]; this technique has recently been used to measure unburned fuel, N_2 , and O_2 concentrations inside a cylinder of a reciprocating engine [6]. Further work on engines has included the use of tracer laser-induced fluorescence [7] for temperature and equivalence ratio measurements. Other combustion diagnostic techniques include the use of tunable diode lasers, FTIR spectroscopy, and spray diagnostics [8].

Most existing techniques for equivalence ratio measurements can only be applied in a known regime, i.e. either before, during, or after the combustion event

occurs, since the methods determine equivalence ratio by measurement of 1) mixture fraction of reactant or product species, 2) condensed-phase concentration, or 3) flame emission. In this work, the use of LIBS is demonstrated in reactants, products and flames, for different types of hydrocarbons, over a wide range of concentration. In combustion process exhaust streams, LIBS has primarily been used to measure inorganic species such as toxic metals, which typically occur in particulate form [9] [10] [11]. Few studies have been undertaken to directly measure hydrocarbons. Related to the work presented in this dissertation, Phuoc and White used simultaneous measurements of the H line at 656.3 nm and the O triplet near 777 nm to determine averaged equivalence ratio in nonreacting and reacting jets of CH₄ and air [12]. Recently, Sturm and Noll [13] have examined averaged LIBS emission of various C, H, O, and N ratios in mixtures of air, CO₂, N₂, and C₃H₈ to determine calibration curves for various elements, and elemental ratios as a function of mixture composition.

The interest in the laser breakdown is not limited to spectroscopy. Application of laser induced plasmas includes laser ablation, material processing and nuclear fusion. Since the early 1960, extensive theoretical and experimental research has been undertaken to describe the physical process involved in the laser breakdown [19]. The first part of the present research is dedicated to the study of the basic phenomena that occur during the formation, expansion and decay of laser-induced plasmas.

1.3 Outline of the manuscript

Chapter 2 of this manuscript is devoted to an experimental study of the laser breakdown. The evolution of the plasma is investigated from the initiation, during the laser pulse, to the subsequent expansion and decay. The main objective of the research is to derive a detailed energy balance on the laser spark. In the first part of the Chapter, an hydrodynamic model of the plasma expansion is presented. Dimensional analysis allows to derive the general scaling laws that control the different phases of the gasdynamic process. Equations are derived to estimate important parameters, including dimensions and temperature of the plasma, and the final energy distribution. The theoretical results are compared with the experimental observations. In the second part of the Chapter, the basic phenomena leading to the emission of atomic lines from the plasma are discussed.

The results described in Chapter 2 are applied in Chapter 3 to measurements of different hydrocarbons. In a laboratory set up, air is mixed with different hydrocarbons over a wide range of concentrations. LIBS is used to obtain a quantitative measure of the fuel-to-air ratio in the mixture. The relative accuracy and the experimental calibration of the technique is discussed. In order to demonstrate the reliability of the technique and to improve the sensitivity, the influence of the main experimental parameters is analyzed. In particular, the effect laser power and detector timing on the recorded spectra is investigated. Finally nonlinear effects that have an influence on the strength of atomic emission are discussed.

In Chapter 4 optical measurements of the fuel-to-air ratio are demonstrated

in a situation of actual interest. LIBS is used to analyze the exhaust gas of a reciprocating engine in real time. The purpose of these measurements is to demonstrate the technique in a real combustion system. The data acquired from the engine are processed using the tool of Principal Component Analysis, which improves the accuracy of the measurements.

Some interesting phenomena that were observed during the experiments are presented in the fifth Chapter. The exhaustive analysis of these findings is left to future research. Finally, the sixth Chapter summarizes the main results and findings of the research.

Chapter 2

Experimental Study of the Laser-Induced Breakdown

2.1 Introduction

When a powerful pulsed laser beam is focused to a small spot in a gas, a breakdown may occur. If the electromagnetic field generated by the incident beam exceeds a threshold value, ions are generated. The absorption cross section of ions is much larger than that of neutral atoms and photons are absorbed as a result of free-free transitions of electrons in the ion field. As energy is absorbed other electron-ion pairs are generated, further increasing the absorption coefficient of the fluid. The result is a cascade phenomenon which results in substantial absorption of the laser pulse, forming a hot plasma which rapidly expands in the cold gas. A detailed description of the physics of laser-induced ionization is given in references [14] [15] [16] [17] [18], and is not within the scope of the present work. Among the first to

research the laser breakdown, Russian physicist Yu. P. Razier identified two possible mechanisms to describe the plasma expansion subsequent to the breakdown [19]:

1. A small absorbing layer of the gas is heated by the laser radiation and rapidly expands. A shock wave propagates in the undisturbed gas in every direction. The gas behind the shock wave is heated and ionized, creating an optically thick layer that absorbs more energy from the laser beam. In this way the absorption zone moves in the direction of the laser beam while a strong shock wave is sent into the fluid. As noted by Razier, this phenomenon is similar to the detonation of explosive materials, in which a shock wave is driven by the release of chemical energy, and has been defined a Laser Supported Detonation [14].
2. The heated gas becomes incandescent. The emitted radiation heats a layer of gas in the proximity of the plasma, which ionizes and becomes optically thick. In this case the energy is transported not by a hydrodynamic disturbance, but by radiation. A "radiation wave" is formed that propagates in the fluid, moving the absorption zone towards the laser beam.

Both mechanisms result in a wave that propagates in the direction of the laser beam and both mechanisms are governed by the same energy balance. The laser energy increases the internal energy of the fluid engulfed by the expanding wave. In a quasi-steady, one-dimensional formulation, the mass rate of gas addition per unit surface in the growing plasma is $\rho_0 D$, where D is the velocity of the wave and ρ_0 is the density of the undisturbed gas. Consequently the energy balance can be written

as:

$$\rho_0 D\epsilon(T) = J_0 \tag{2.1}$$

where J_0 is the absorbed light flux (in J/m^2s) and $\epsilon(T)$ (J/kg) is the specific internal energy of the fluid (this energy balance ignores the kinetic energy of the fluid set in motion).

From these considerations, Razier derived estimates for the plasma temperature behind the wave and for the velocity of the wave that are in good agreement with experimentally measured values. Both the Laser Detonation and the Radiation Wave mechanisms predict a temperature of the plasma behind the wave on the order of 10^5 K and a velocity of the wave close to 10^5 m/s (for the experimental conditions described in [19]). As noted in [19], under the experimental conditions commonly encountered (laser pulse energy < 10 J and pulse duration ~ 10 ns) both mechanisms predict similar results, most often within the margin of experimental error, and it is difficult to distinguish between them on the basis of experimental measurements. Today it is believed that both regimes can be attained during laser breakdown, but the conditions determining the controlling mechanism are not completely understood [14].

Despite their similarities, Laser Supported Detonations and Radiation Waves are governed by different sets of equations. In the first case the equations of hydrodynamics apply, and a shock wave is coincident with a back-propagating wave. In the case of a Radiation Wave, the energy transport can be described by the heat equation (including transport by radiation), but with temperatures of the order of

10^5 K, the radiation thermal diffusivity coefficient χ (m^2/s), should be considered a nonlinear function of temperature [20]. The strong dependence of χ on temperature gives the transport of energy by radiation the character of a wave, although a proper shock wave might not be present in the fluid. In particular, a Radiation Wave can travel faster than the normal detonation velocity, and during the first stages of the expansion, the pressure behind the wave might not be in local equilibrium. For these reasons the distribution of temperature, density and pressure behind the two types of waves is considerably different [14]. Transport mechanisms for the laser supported wave have been studied extensively (although mainly with one-dimensional models that do not fully account for the lateral expansion of the plasma described in the remainder of the Chapter) and detailed descriptions can be found in references [21] [22] [23] [24] [25] [26] [27] [28] [29]. As described by Razier, after sufficient time has passed following the end of the laser pulse, the shock wave that emerges from the breakdown assumes the character of a point explosion and can be described by the theory developed by G. I. Taylor [30] and L. I. Sedov [31].

In this chapter the results of an experimental investigation of the laser breakdown are presented. The plasma formation, expansion, and subsequent dissipation are investigated, and the results are interpreted on the basis of simple energy and dimensional considerations. We describe the formation of the plasma during the laser pulse as a Laser-Supported Detonation. Such a model is consistent with the experimental observations. As discussed in [14], scaling laws similar to those presented can also be derived also in the case of a Radiation Wave [14]. Later sections describe the fate of the energy in the fluid after the laser pulse.

2.2 Measurement of the Radiated Energy

For laser pulse energies sufficiently exceeding the breakdown threshold, approximately 90% of the laser energy is absorbed in the plasma [32] [33], while the rest is either transmitted through the plasma or reflected by the focussing optics. The energy deposited in the plasma is dissipated by different mechanisms: part is radiated into the cold environment, part is coupled into the expanding shock wave, and part is dissipated by conduction and convection.

Electromagnetic radiation is generated in the highly ionized gas by Bremsstrahlung, at the expense of the kinetic energy of the electrons. To assess the fate of the energy released in the fluid during the laser breakdown, it is necessary to determine the amount radiated as a function of the laser pulse energy. The radiated energy is measured by an energy meter facing 90° with respect to the direction of the laser beam. A Nd:YAG laser with pulse width $t_0 = 10$ ns FWHM generates the plasma in air. A detailed description of the experiment is given in the Appendix. To estimate the energy radiated over the whole 4π solid angle it is assumed that the plasma radiates like a point source with spherical symmetry. Table 1 shows the estimated total radiated energy obtained from measurements.

For laser pulse energies in the range between 70 and 550 mJ, the radiated energy is only $4 \sim 5\%$ of the energy deposited in the plasma. In order to validate the hypothesis of spherical symmetry the detector is moved in the direction perpen-

Table 2.1: *Energy radiated by laser plasmas in air, for different values of the laser pulse energy.*

Deposited energy	Total radiated energy	Percentage radiated
mJ	mJ	%
74.4	4.6	6.2
168.3	6.9	4
258.7	10.4	4
311.3	15.2	4.9
524.6	17.9	3.4

dicular to the laser beam using a precision translation stage with a total travel of 38 mm. In the case of a point source, the energy radiated on the surface of the detector should exhibit a $1/r$ dependence on the distance from the plasma. Due to the finite dimensions of the plasma, the measured energy departs a little (less than 10%) from this rule. Nevertheless, it is estimated that, in the absence of dramatic variations in the gradient of the radiation field (in the second derivative of the radiative energy with respect to space), the total radiated energy should not differ greatly from the values reported in Table 2.1. Overall, the values reported represent an order-of-magnitude estimate and express the fact that only a small fraction of the total energy is dissipated by radiation. Similarly, the x-rays and extreme-UV radiation emitted by the plasma were measured with a diamond photodiode (from Alameda Applied Science Corporation). Although x-ray radiation is clearly detectable, the energy radiated at these wavelengths is much less than 1% of the total deposited

energy.

2.3 The Laser Supported Wave

The amount of energy radiated by the plasma appears to be modest. To a first approximation, for the purpose of writing a detailed energy balance on the laser spark, it is thus possible to ignore radiation and to consider the process adiabatic within a suitable control volume. In the present section, a description is given of the gas-dynamic phenomena taking place during the energy deposition time, t_0 . Assuming an adiabatic flow and an inviscid fluid [46], the plasma is governed by the Euler equations for conservation of mass, momentum and energy, supplemented by an equation of state. The set of governing equations can be written in the customary way [20]:

$$\frac{D\rho}{Dt} + \rho \nabla \cdot \mathbf{u} = 0, \quad (2.2)$$

$$\frac{\partial \mathbf{u}}{\partial t} + \mathbf{u} \cdot \nabla \mathbf{u} = \frac{1}{\rho} \nabla p, \quad (2.3)$$

$$\frac{\partial}{\partial t} \left(\rho \epsilon + \frac{\rho \mathbf{u}^2}{2} \right) = -\nabla \cdot \left[\rho \mathbf{u} \left(\epsilon + \frac{\mathbf{u}^2}{2} \right) + p \mathbf{u} \right] + \rho Q, \quad (2.4)$$

where Q (J/kg s) is the energy released in the fluid per unit mass, per unit time. Assuming an equation of state similar to the perfect gas law, the internal energy of the fluid ϵ (J/kg) can be written as:

$$\epsilon = c_v T = \frac{1}{\gamma - 1} \frac{p}{\rho}, \quad (2.5)$$

where γ is the effective ratio of the specific heats, assumed to be constant. Using these equations we are interested in finding the position of the Laser Supported Wave in space at the end of the laser pulse.

Figure 2.1 shows an image of the strongly luminous plasma generated in an atmosphere of argon (at atmospheric pressure), at the end of the laser pulse. The images were taken with a Roper Scientific PI-Max camera, able to acquire pictures with nanosecond resolution, and the energy deposited into the plasma was approximately 89 mJ. The experiment is described in more detail elsewhere [33] [34]. After 10 ns the plasma is already several mm in length. The direction of the laser is from the left to the right, in the plane of the pictures, and the laser supported wave propagates from right to left as it expands radially.

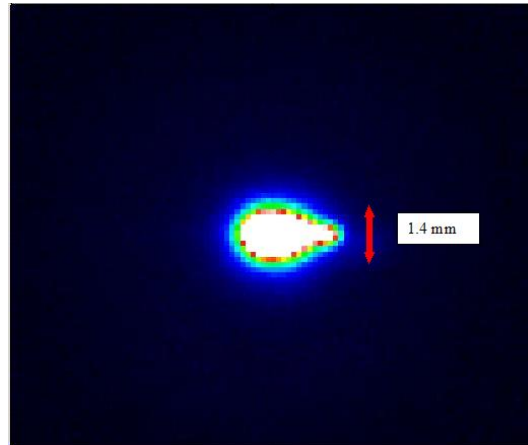


Figure 2.1: *Image of the laser plasma in Ar, 10 ns after the initiation of breakdown, with a deposited energy of 89 mJ.*

2.3.1 Dimensional analysis of the laser supported wave

We are interested in finding the position of the wave, r , at the end of the laser pulse. In spherical coordinates, the radius r and time t are the dimensional variables of the problem while longitudinal and azimuthal angle, θ and φ , are dimensionless variables. After time t_0 has passed, energy E has been deposited in the fluid. With the formulation given by Equations 2.2-2.4, if the ambient pressure is negligible compared with the pressure behind the shock wave, the only dimensional parameters of the problem are t_0, E , and the density of the undisturbed gas ρ_0 , while γ is a non-dimensional parameter. The problem can be described in terms of the non-dimensional parameter γ and the non-dimensional variables:

$$\frac{r}{\left(\frac{E}{\rho_0}\right)^{1/5}(t_0)^{2/5}}, \quad \frac{t}{t_0}, \quad \theta \quad \text{and} \quad \varphi. \quad (2.6)$$

In particular, the angles θ and φ are needed, since the laser comes from a definite direction in space, and, as shown in Figure 2.1, the Laser Supported Wave is not spherically symmetric. The problem has a characteristic time, t_0 , and a characteristic length, $r_0 = \left(\frac{E}{\rho_0}\right)^{1/5}(t_0)^{2/5}$. Applying the Buckingham II theorem, the distance travelled by the wave in a given direction, in the time t_0 is given by:

$$r = \left(\frac{E}{\rho_0}\right)^{1/5} (t_0)^{2/5} g\left(\frac{t}{t_0}, \theta, \varphi, \gamma\right) \quad (2.7)$$

where g is an unknown non-dimensional function. At the end of the laser pulse the value of the independent variable is $\frac{t}{t_0} = 1$. The value of $g(\theta, \varphi, \gamma)$ is still unknown, but with these assumptions, Equation 2.7 provides a scaling law for the Laser Sup-

ported Wave. In particular, at the end of the laser pulse, the dimensions of the plasma should scale with the fifth root of the deposited energy. Figure 2.2 shows, in the left column, the images of a luminous plasma generated in argon at the end of a 10 ns laser pulse ($p = 1 \text{ atm}$), for different values of deposited energy. To verify the scaling law of Equation 2.7, the images on the left column were normalized, dividing by the fifth root of the deposited energy. Figures 2.3 and 2.4 show similar images for a plasma generated in air at ambient pressure. When normalized, the plasmas generated by laser pulses with different energies appear similar, and it is possible to obtain a quantitative agreement with the scaling law of Equation 2.7 (as shown in the remainder of this section). The evident difference in the shape of the plasma between air and argon is probably due to the different thermodynamic properties that determine, among other things, the speed of sound in the two gases. More research is needed to model in detail the behavior of the different gases.

For a 10 ns laser pulse with a deposited energy of 100 mJ, the characteristic length r_o (for a gas at standard density) is 0.38 mm in air and 0.35 mm in argon. The dimension of the plasma at the end of the laser pulse will be proportional to r_o . For example, the dimension of the plasma at the point of maximum lateral expansion (i.e., the distance travelled by the Laser Supported Wave in the direction perpendicular to the beam, at the point of maximum lateral expansion) will be $r = \beta r_o$ where the constant of proportionality β , is found experimentally to be 2.76 for air and 2.34 for argon. Figure 2.5 shows the comparison of the radial expansion measured experimentally to the theoretical scaling law for, plasmas in air and argon. The boundary of the wave in the images from Figures 2.2, 2.3 and 2.4

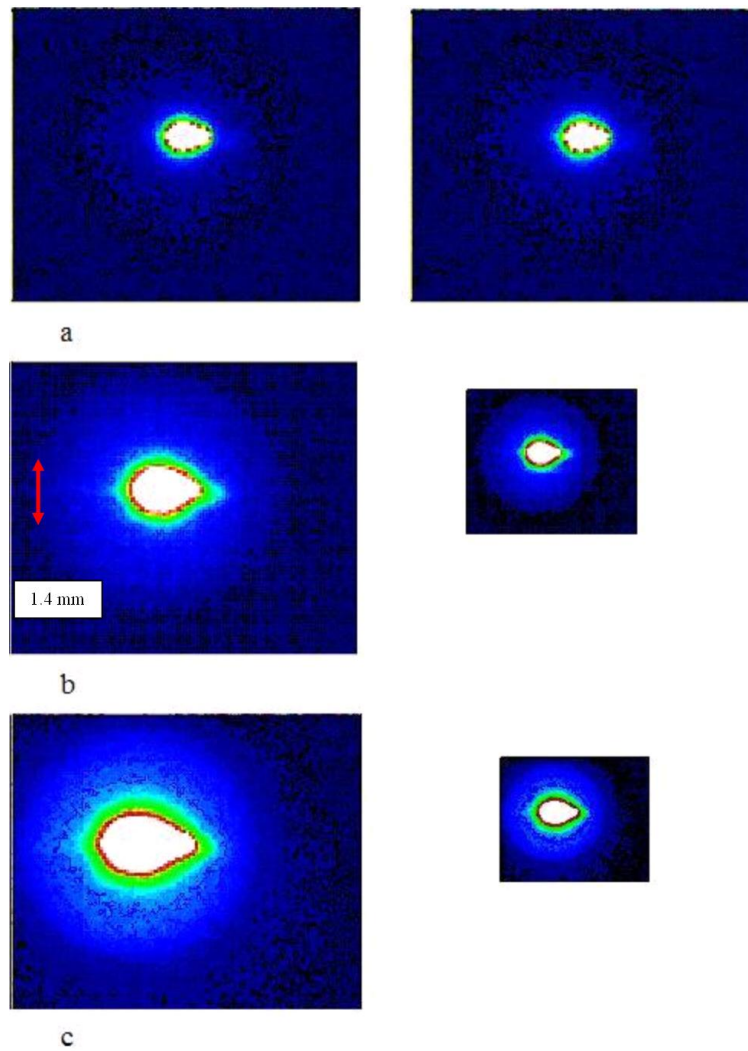


Figure 2.2: Images on the left column show the laser plasma in argon, after 10 ns, for different value of deposited energy: a) $E = 7$ mJ, b) $E = 89$ mJ, c) $E = 199$ mJ. The right column shows the same images normalized.

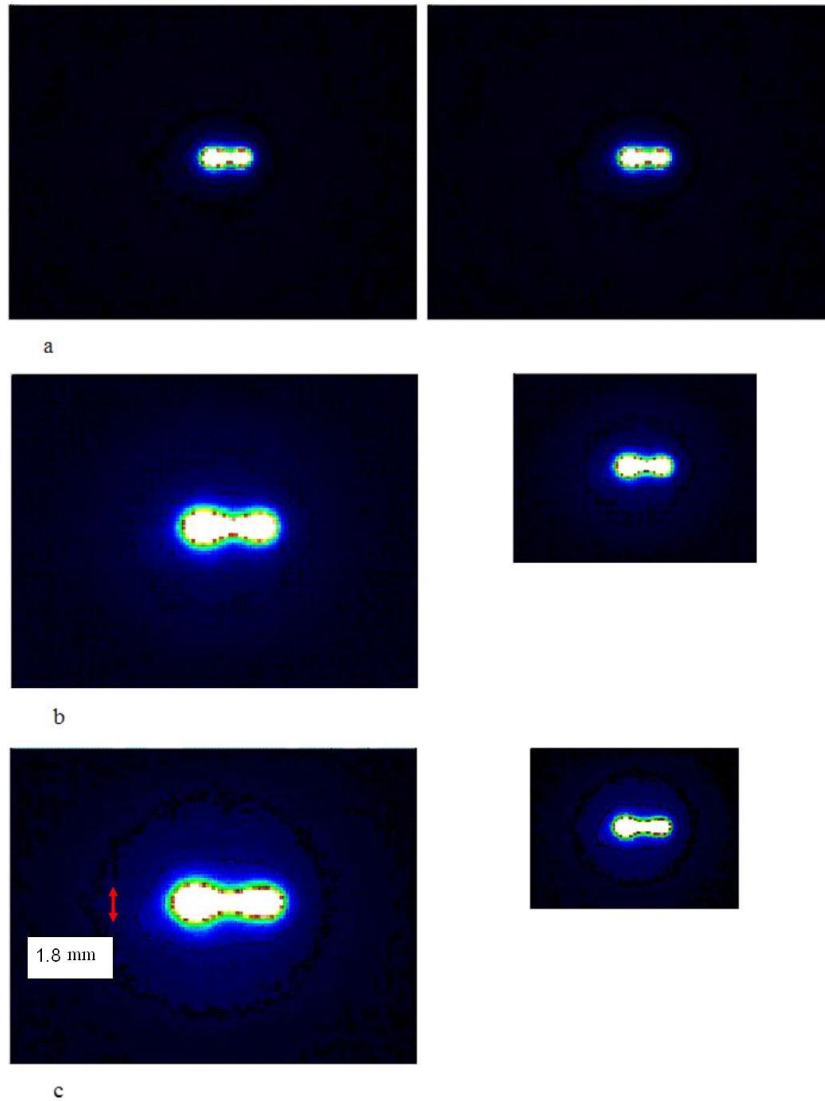


Figure 2.3: *Images on the left column show the laser plasma in air, after 10 ns, for different value of deposited energy: a) $E = 3$ mJ, b) $E = 36$ mJ, c) $E = 74$ mJ. The right column shows the same images normalized.*

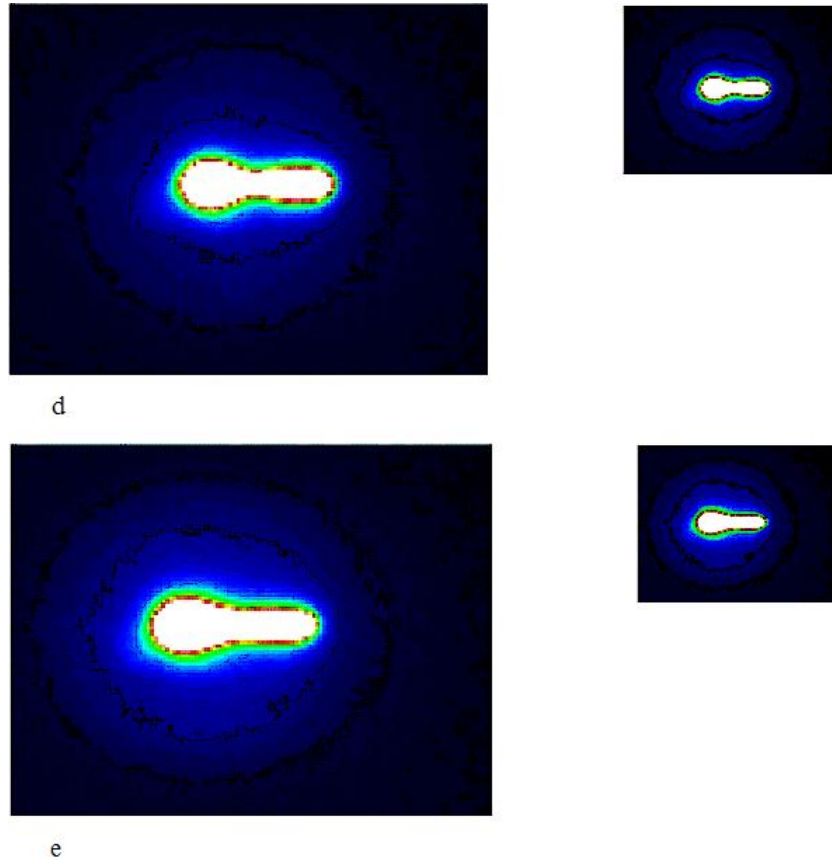


Figure 2.4: *More images of the laser plasma in air. Deposited energy d) $E = 147$ mJ e) $E = 206$ mJ.*

is not perfectly sharp and the exact wave position is defined, somewhat arbitrarily, as the point where the light intensity drops below the 5% of the maximum value.

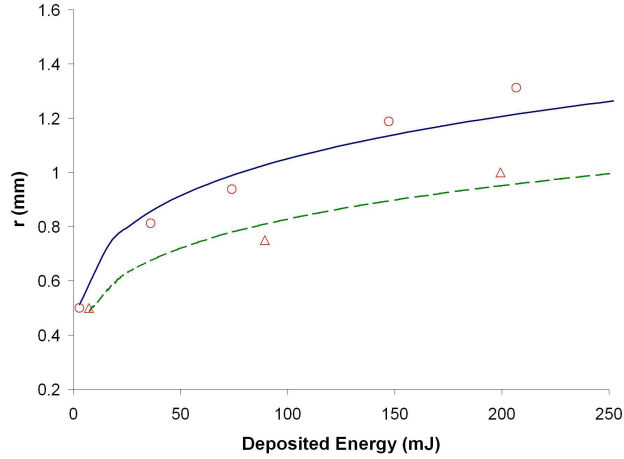


Figure 2.5: *Lateral expansion of the plasma as a function of the deposited energy. Comparison of the theoretical scaling law (lines) with the experimental data for air (circles) and argon (triangles).*

The data presented in Figures 2.2-2.5 suggest that the scaling law in Equation 2.7 agrees well with experimental observations for laser pulses with energies in the range between 10 and 250 mJ. The scaling law (2.7) appears valid for both air and argon, although the simple analysis proposed cannot explain the different shapes of the plasma obtained in air and argon. There are, however, other length scales that might be considered in the formulation of the problem, and their relevance should be discussed. One is the beam waist at the focal spot. Due to optical aberration the diameter of the beam at the focus is finite and depends on the focusing optics used. This length can be evaluated using approximations from Gaussian optics

[36]. For the experimental conditions presented in this paper, the beam waist is on the order of $10 \mu m$, much smaller than the characteristic length r_0 . A second length scale is the absorption mean free path of the photons in the optically thick plasma. This quantity determines the length of the energy absorption zone behind the Laser Wave. There is no simple way to estimate this length scale; we note that, for gas pressure close to ambient, the absorption of the laser by the plasma is almost complete, suggesting that the mean free path of the photons is considerably smaller than the dimensions of the plasma. It is possible that the existence of other length scales is responsible for the small differences in the shape of the plasma that can be observed in Figures 2.2-2.4, especially for the breakdown in air at high energy.

2.3.2 Maximum plasma temperature and average plasma temperature

Figures 2.6 and 2.7 show the measured contour of plasmas in non-dimensional coordinates for air and argon (derived from one of the images in Figure 2.2-2.4). As above, the contour of the plasma is defined as the position where the radiated intensity drops below 5% of the maximum value. Assuming cylindrical symmetry, it is possible to determine the volume of the plasma in non-dimensional coordinates by numerical integration. This non-dimensional volume \mathbb{V} relates the characteristic length r_0 to the physical volume, \mathbf{V} , such that $\mathbf{V} = \mathbb{V}r_0^3$; we find $\mathbb{V} = 110$ for air and $\mathbb{V} = 60$ for argon. With the non-dimensional volume we can predict the plasma volume as a function of deposited energy from r_0 (Equation 6), as shown in Figure

2.8.

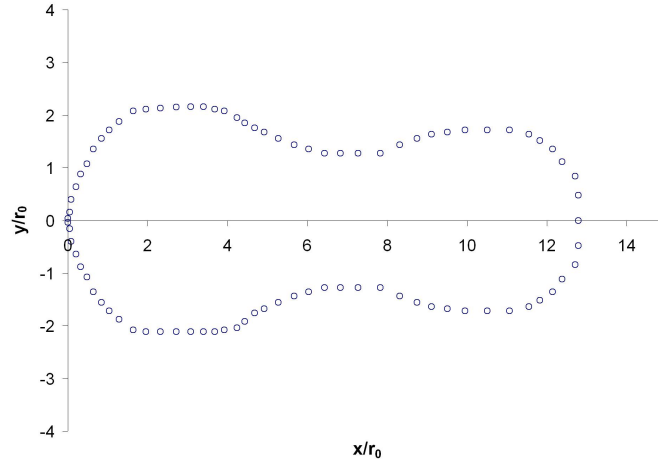


Figure 2.6: *Contour of the plasma in air at $t=10$ ns.*

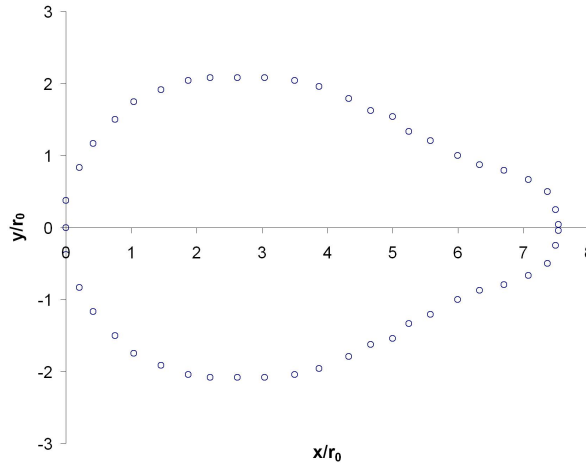


Figure 2.7: *Contour of the plasma in argon at $t=10$ ns.*

As pointed out in [14], the values of temperature, density and pressure are not constant throughout the volume of the plasma. The temperature of the plasma in the absorption layer was estimated by Razier [19] who used an experimental measurement of the beam waist at the focal spot to determine the light flux J_0 in Equation 2.1. The conditions of conservation of mass, momentum and energy

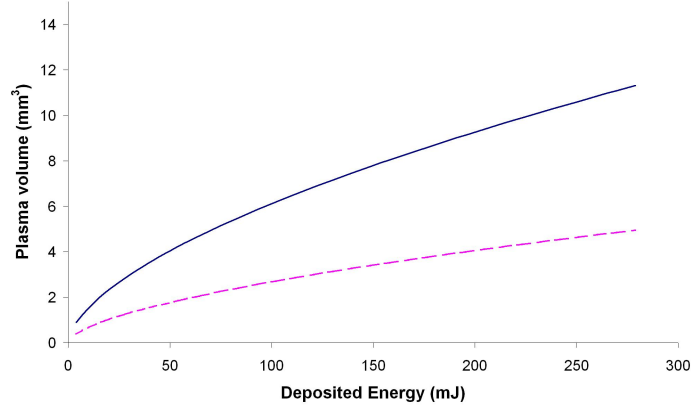


Figure 2.8: *Volume of the plasma as a function of the laser pulse energy based on the experimentally determined \mathbb{V} (for gases at standard density). Air: solid line; Ar: dashed line.*

through the shock wave lead to the relations:

$$\rho u = \rho_0 D, \quad p + \rho u^2 = \rho_0 D^2, \quad \text{and} \quad \epsilon + \frac{p}{\rho} + \frac{1}{2}u^2 = \frac{1}{2}D^2 + \frac{J_0}{\rho_0 D} \quad (2.8)$$

where D is the velocity of the Laser Supported Wave and ρ, p, u , and ϵ are the density, pressure, velocity and internal energy of the gas behind the wave. Using the equation of state (2.5) it is possible to derive the shock adiabat of the wave and determine the value of D and ϵ . In particular, the wave travels with sonic velocity with respect to the gas behind it, satisfying the Chapman-Jouguet condition, and there is a maximum value of the compression ratio of the gas behind the front (depending on the effective ratio of the specific heats, see [19] and also [20] for more details). From the internal energy it is possible to estimate temperature assuming equilibrium. Once the energy balance in Equation 2.1 is corrected to account for lateral expansion of the plasma, multiplying J_0 by an empirical coefficient close

to 0.5 [19], the calculated values agree well with the temperature value measured experimentally. In particular, for the experimental conditions used in [19], the plasma temperature (measured spectroscopically) was found to be on the order of $\sim 10^5$ K. The model of a laser-driven shock wave assumes that the fluid expands adiabatically behind the wave (see also [14]), and the average temperature of the plasma is at least one order of magnitude smaller than the maximum temperatures attained in the absorption zone.

The volume of the plasma at the end of the laser pulse defines the region where the known energy E is deposited. Since the expansion wave is supersonic with respect to the undisturbed fluid, conservation of mass requires that the average density of the plasma is equal to that of the undisturbed gas. Knowing the volume of the plasma \mathbf{V} , at the end of the laser pulse, the average internal energy of the fluid can be calculated from the relation:

$$\rho_0 \mathbf{V} \bar{\epsilon} = E. \quad (2.9)$$

For gases at high temperature the internal energy can be approximated with interpolation formulae of the form [20]:

$$\epsilon = a T^\delta \rho^\zeta, \quad (2.10)$$

where ζ and δ are empirical coefficients that can also be used to determine an effective ratio of the specific heats:

$$\gamma = 1 + \frac{\zeta}{1 - \delta}. \quad (2.11)$$

In particular, for air in the temperature range from 10000 K to 250000 K, the internal energy can be approximated with the formula [20]:

$$\epsilon = 3.34 \cdot 10^6 \left(\frac{T}{10^4} \right)^{1.5} \left(\frac{\rho}{\rho_0} \right)^{-0.12}, \quad J/kg \quad (2.12)$$

corresponding to $\gamma = 1.24$. The local value of the density is not known (only the average value ρ_0), but it cannot exceed the limiting value of $\rho = \rho_0 \frac{1+\gamma}{1-\gamma}$ ($\approx 9.3\rho_0$). Moreover, Equation 2.9 ignores the fact that the fluid is set in motion and some energy is converted in kinetic energy. With these approximations, it is possible to estimate a reference average temperature. Inserting Equation 2.12 into Equation 2.9 and substituting the expression for \mathbf{V} one obtains:

$$\bar{T} = 10^4 \left(\frac{E}{3.34\rho_0 \nabla r_0^3} \right)^{2/3}, \quad K. \quad (2.13)$$

The plasma temperature was measured spectroscopically in [33] a few tens of ns after the breakdown initiation. The ratio of atomic emission lines of N^+ was used to determine the electron population distribution among different quantum energy levels. Assuming the distribution to be in Boltzmann equilibrium between the energy levels, an estimate of the bulk electronic temperature was obtained. The experiment and the technique are described in more detail in [33]. Figure 2.9 shows the comparison between the measured temperatures and the estimates obtained from Equation 2.13. The temperatures predicted by Equation 2.13 are approximately 8%

lower than the experimental value, but, overall, Equation 2.13 describes the relation between deposited energy and bulk plasma temperature at the end of the laser pulse quite well. Both the theoretical and the experimental values reported for temperature should be regarded as estimates; for example the experimental values are spatially distributed but might not exactly represent the average value for the whole plasma. In addition, when considering the spatial distribution of temperature, radiation flux should be considered. Because energy is transferred by radiation at the speed of light, even if the total radiated energy is modest, the radiative heat flux might be considerable. The temperature distribution inside the plasma, where the absorption mean free path of the emitted photons is short, might depend significantly on energy transfer by radiation.

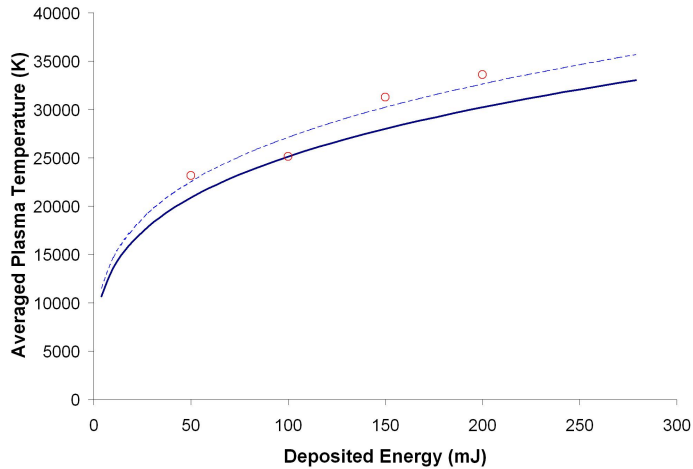


Figure 2.9: *Plasma temperature as a function of laser pulse energy. Comparison between experimental measurements (dots) and theoretical estimates (solid line). The dashed line represents the fit of Equation 2.13 to the experimental data with an empirical parameter.*

2.4 Post Breakdown Evolution

After the end of the laser pulse the shock wave expands in the undisturbed gas, cooling the plasma by adiabatic expansion. When the characteristic length r_0 becomes much smaller than the radius attained by the shock wave, the wave assumes the character of a Taylor-Sedov Blast Wave i.e., a spherically symmetric point explosion. There are two distinct regimes of motion with different dimensional constraints. Due to the localized energy release in the absorption zone, the Laser Supported shock wave travels much faster than the Taylor-Sedov shock wave corresponding to instantaneous release of the same amount of energy, see also the next section. We note that for every kind of energy release, there exists a finite energy release time scale and a corresponding energy release length scale. For example, during the first moments of a nuclear explosion, an extremely hot plasma appears, often called the “fireball” [37]. The fireball is normally described as a radiation wave. For the nuclear test explosion in New Mexico in July 1945, where the energy released was approximately 10^{14} J, the fireball had reached the radius of 14 m after 0.1 ms (with an expansion velocity of $1.4 \cdot 10^5$ m/s). Only at this point did a shock wave emerge from the radiation wave. In this respect, the Taylor-Sedov solution of the point explosion should be considered an asymptotic theory that is valid at distances sufficiently large that the dimensional argument of Taylor and Sedov can be applied.

To investigate the gas-dynamic evolution of the laser breakdown, shadow-graphic measurements are performed. A sheet of light from a second laser is used to illuminate the plasma at right angles. The two lasers are accurately synchro-

nized and, for measurements taken closer to the breakdown event where precision is more critical, the timing is accurate within ± 30 ns (at later stages the timing was checked less frequently, but it is still considered accurate within ± 100 ns). A detailed schematic of the experiment is given in the Appendix. The technique of shadowgraphy measures variations in the index of refraction of a gas due to density gradients. In particular, shadowgraphy is sensitive to the second derivative of density with respect to space. After the end of the laser pulse the shock wave rapidly loses strength and the temperature behind the wave drops. The gas engulfed by the shock wave following the laser pulse ionizes (see also Section 4.2), but is far less luminous than the very hot gas in the absorption zone of the Laser Supported Wave, and does not appear in the images taken with an exposure time of few nanoseconds (such as Figures 2.2 or 2.3). The shock wave rapidly leaves the plasma core formed during the laser pulse, which stops expanding. The strongly luminous plasma completes the greatest share of its expansion during the first 10 ns. After few tens of nanoseconds the continuous radiation emitted by the plasma begins to dim, as a consequence of the adiabatic expansion.

Figure 2.10 compares the plots of the measure radiated intensity, the nanosecond exposure photographic images (from the same plasma) and the shadowgraphs. Figure 2.11 shows the evolution of a shock wave generated by a laser breakdown in air with a total absorption of 93 mJ in air. After approximately 100 nanoseconds from breakdown initiation, the gas expansion can be detected in the shadowgraphic images. This is consistent with a strong acoustic disturbance emerging from the plasma at the end of the laser pulse, i.e., with the model of a shock wave that is

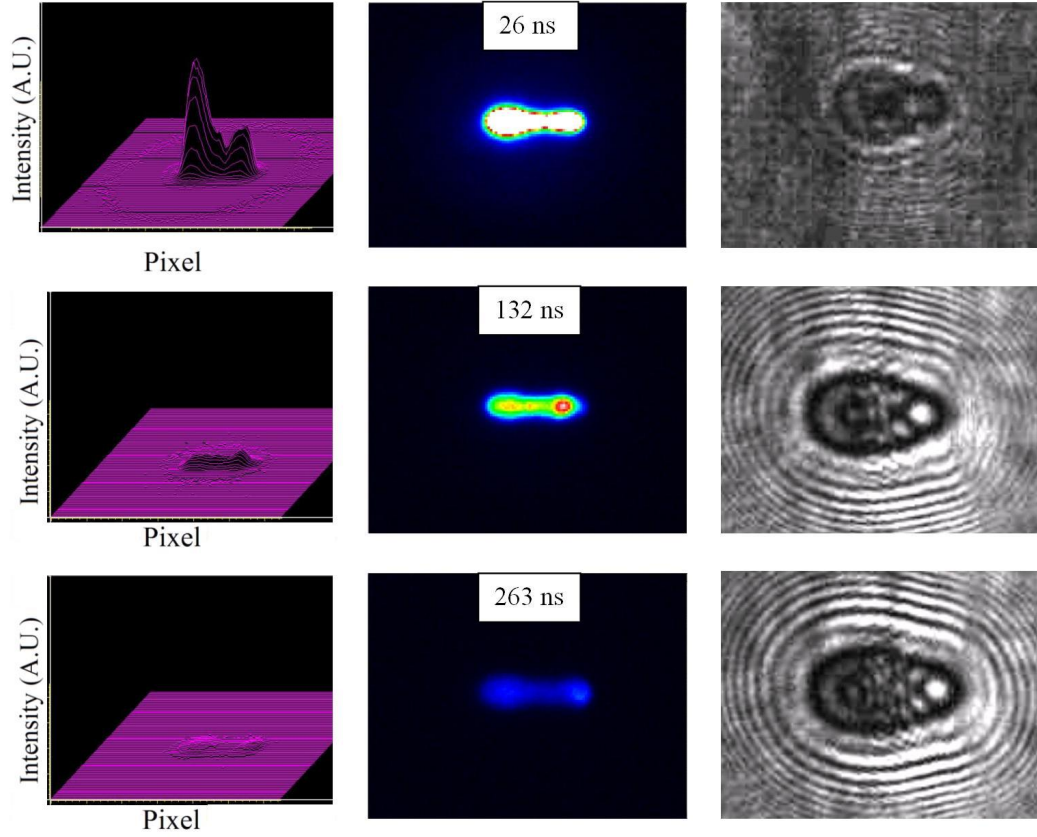


Figure 2.10: Comparison of the radiated intensity, the 1 nanosecond exposure photographs, and the shadowgraphs during the first instants of the plasma expansion. Images correspond to an energy release of approximately 93 mJ and are approximately to scale.

coincident with or ahead of the edge of the luminous plasma. As we will see below, it is at this point that the Taylor-Sedov theory becomes useful.

Most of the continuous radiation emanating from plasma core has faded after few hundreds of nanoseconds. During this period energy is transferred to the layer of gas surrounding the plasma core. Atomic emission, from both neutral and ionic lines, persists much longer in time, several μs for ionic lines, and tens of μs for

neutral line emission.

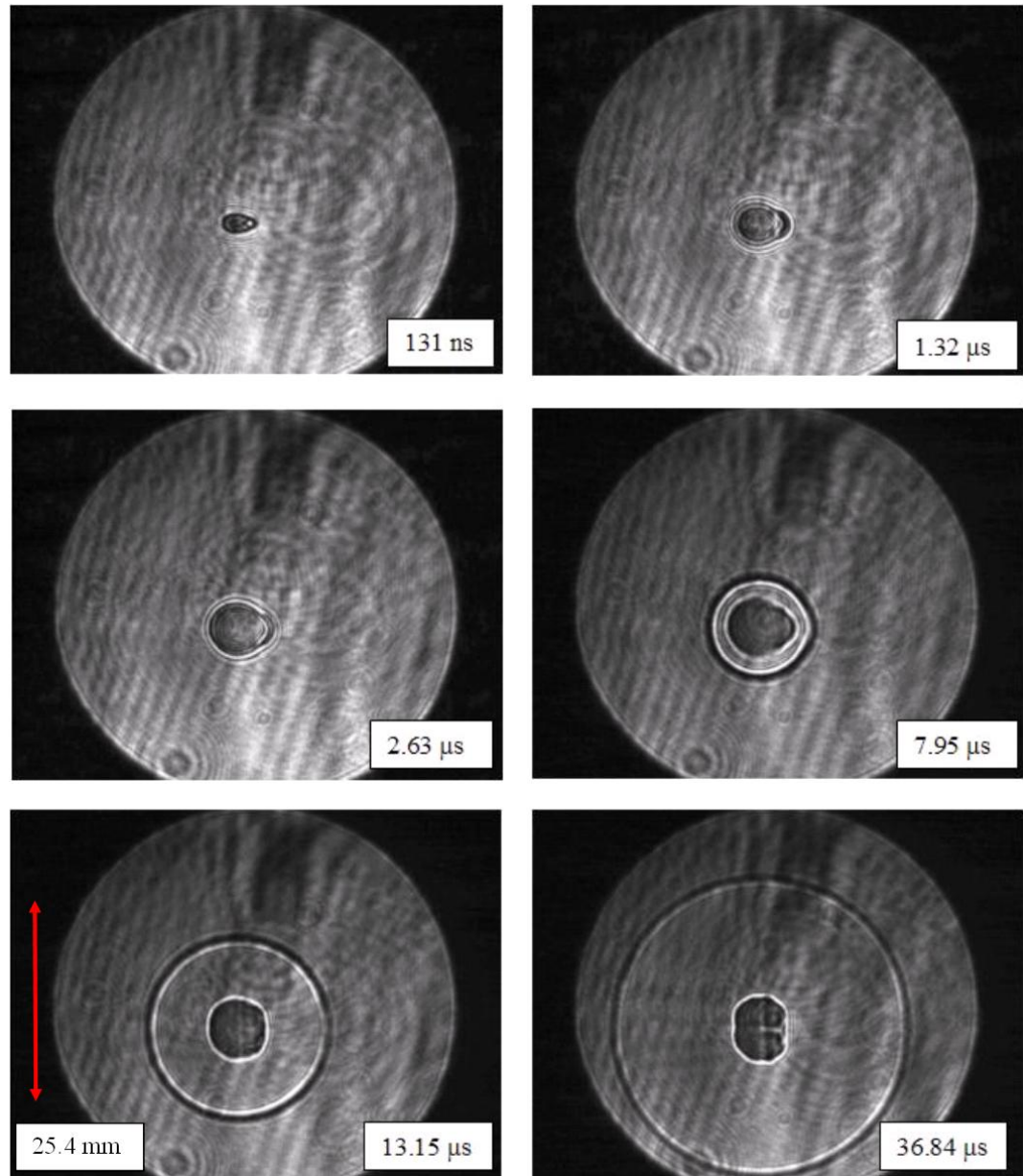


Figure 2.11: *Evolution of the shock wave generated by the laser breakdown in air ($E = 93 \text{ mJ}$).*

To explain with more clarity the behavior of the expanding shock wave, we recall briefly the relevant parts of the theory of point explosions. An exhaustive

description of Similarity methods in applied sciences is given in [31], [35] and also in [38] [39] [40].

2.4.1 The idealized point explosion

When the the length and time scales r_0 and t_0 become small compared with radius of the shock wave, the solution of the propagating wave can be found as if the energy were released instantaneously from a point source. The formulation of this problem is given in Equations 2.2-2.5. If we assume that the ambient pressure is negligible with respect to the pressure behind the shock wave, the only dimensional parameters of the problem are the deposited energy, E , and the ambient density, ρ_0 . As above, γ is a non-dimensional parameter. Assuming spherical symmetry, the radial coordinate, r , and time, t , are the only variables. Defining the similarity variable

$$\xi = r \left(\frac{\rho_0}{Et^2} \right)^{1/5}, \quad (2.14)$$

the Buckingham II theorem requires the radius attained by the shock wave at the time t to be [20]:

$$R = \left(\frac{E}{\rho_0} \right)^{1/5} (t)^{2/5} g(\xi_0, \gamma), \quad (2.15)$$

where g is a non-dimensional function and $g(\xi_0, \gamma)$ a particular value of this function that does not depend on r or t independently. For each value of the similarity variable ξ , the value of $g(\xi_0, \gamma)$ is a constant. Customarily the value of the constant is grouped with the energy, and the position and velocity of the shock wave are

given by the relations:

$$R = \left(\frac{\alpha E}{\rho_0} \right)^{1/5} (t)^{2/5}, \quad D = \frac{dR}{dt} = \frac{2}{5} \left(\frac{\alpha E}{\rho_0} \right)^{1/5} (t)^{-3/5}. \quad (2.16)$$

Since the function g does not depend on the variables, the problem is self-similar. This means that the shapes of the distribution of ρ , p and u do not change in time and scale in a similar way (i.e., satisfy the same one-parameter group of scaling transformations [35]). In order to obtain a complete solution it is necessary to determine the distribution of the fluid variables at a particular time, $t = t_1$, which yields the value of the function g for every value of r . After this,, the property of self-similarity can be exploited to scale the results for every t [31]. Briefly, it is possible to express the distribution of velocity and pressure as a function the velocity and pressure behind the shock front, leaving the non-dimensional parameter $\alpha = \alpha(\gamma)$ in Equation 2.16 as the only unknown. The value of α is found from the energy balance on the sphere encompassed by the shock wave:

$$\int_0^R \left(\frac{\rho u^2}{2} + \frac{p}{\gamma - 1} \right) 4\pi r^2 dr = E \quad (2.17)$$

The first term on the left-hand-side of Equation 2.17 represents the kinetic energy of the fluid and the second term describes the internal energy. Substituting the analytical expressions for u and p (as a function of α) into (2.17), the value of α is found to be 1.175 for air with $\gamma = 1.4$ and ~ 2 for a perfect gas with $\gamma = 1.66$ [31], [47]. The density, pressure and velocity of the gas behind the discontinuity are given by the limiting formulas for strong shocks:

$$\rho = \rho_0 \frac{\gamma + 1}{\gamma - 1}, \quad p = \frac{2}{\gamma + 1} \rho_0 D^2, \quad \text{and} \quad u = \frac{2}{\gamma + 1} D. \quad (2.18)$$

Behind the wave the gas is compressed to a temperature of the order of:

$$T = \frac{T_0 \rho_0}{p_0} \frac{2(\gamma - 1)}{(\gamma + 1)^2} D^2, \quad (2.19)$$

where T_0 is the ambient temperature. As $t \rightarrow 0$, $D \rightarrow \infty$ and $T \rightarrow \infty$. The presence of a plasma core that does not obey the scaling symmetry of Taylor and Sedov avoids this non-physical singularity. For an energy release of 100 mJ in air, Equation 2.16 predicts a plasma radius of 0.39 mm after 10 ns, at least three times smaller than that attained by the (non-spherical) Laser Supported Wave at the end of the laser pulse and with an error in the energy density of the fluid of a factor of 24. As noted above the self-similar Taylor-Sedov solution is only valid following the point at which the shock wave travels far away from the kernel of hot gas

As the blast wave expands, it loses its strength. Once the ambient pressure, p_0 , is comparable with the pressure behind the wave it cannot be disregarded, and the dimensional parameter p_0 enters in the formulation of the problem. Now the problem has a characteristic length and a characteristic timescale given by [31]:

$$r_a = \left(\frac{E}{p_0} \right)^{1/3}, \quad t_a = \frac{(E)^{1/3} \rho_0^{1/2}}{p_0^{5/6}} \quad (2.20)$$

where the acoustic radius, r_a , represents the radius of the sphere whose internal energy is comparable with the energy release E (and which is proportional to the acoustic radius defined recently by Liñán et al. [41]). At this stage of the expansion,

Table 2.2: *Position of the shock front as a function of time, in non-dimensional coordinates (from [31]).*

r/r_a	t/t_a	r/r_a	t/t_a
0.1867	0.01403	0.9801	0.6296
0.2669	0.0323	1.2524	0.6811
0.3342	0.05431	1.321	0.8299
0.489	0.1231	1.5171	1.108
0.6003	0.1842	1.8751	1.4636
0.6003	0.2333	2.3222	1.8973
0.6812	0.2807	2.8641	2.7763
0.7566	0.3667	3.6983	5.3764
0.9566	0.4323	7.0791	7.518

the problem can be expressed in terms of the non-dimensional variables r/r_a , t/t_a . When the radius of the shock wave is comparable with r_a (more precisely, when $r \sim 0.18 r_a$, as discussed in [31]), Equation 2.16 ceases to be a good approximation for the position and velocity of the shock wave. The position of the shock in time is given by:

$$r = r_a f(r/r_a, t/t_a, \gamma) \tag{2.21}$$

Since the non-dimensional function, f , depends on the non-dimensional radius and non-dimensional time, the problem is no longer self-similar. Once the solution

for g is known as a function of the non-dimensional variables, Equation 2.21 can be used as a scaling law for every blast wave. At the end of the Second World War, calculations were carried out to numerically solve the propagation of the weak blast wave, using the self-similar solution as initial condition for the one-dimensional gas-dynamic problem. To arrive at a solution, J. Von Neumann used the pioneering idea of a stored computer program to perform one of the very first Computational Fluid Dynamics simulations in 1955 [42]. The results of an equivalent simulation, carried out by Soviet scientist Korobeĭnikov and co-workers in the late fifties [47], and presented in great detail in the book by Sedov [31], will be used in this paper. For air with $\gamma = 1.4$, the position of the weak blast wave as a function of time, in non-dimensional coordinates, is given in Table 2.2.

2.4.2 The self-similar region: comparison with the experimental results

For a 100 mJ laser pulse in air at standard conditions, the characteristic acoustic radius is approximately $r_a = 9.4 \text{ mm}$ and the characteristic time is $t_a = 33.1 \mu\text{s}$. To compare the experiments with theory, the position of the shock wave in time is estimated from the shadowgraphs. As discussed above, at the end of the laser pulse the plasma is considerably bigger than the dimensions predicted by Equation 2.16. The experimentally measured dimensions of the plasma can be used to determine the radius attained by the shock wave at 10 ns. Figure 2.12 shows the fitting of the experimental data to a relation of the form of Equation 2.16, once the dimensions

of the plasma core are taken into account to provide the correct initial conditions (that is, the radius at $t = 10$ ns). Figure 2.12 and the measurements of the shock wave velocity published in [43] and [44] show that the the Laser Supported Wave acquires the character of a Taylor-Sedov blast wave after few hundred ns. However, the fit to the experimental results is an approximation and cannot be used to derive accurate information on the distribution of velocity and temperature. In first place, the presence of interference fringes in the shadowgraphs are a source of experimental errors. Moreover, the presence of a non-spherical plasma core is not contemplated by the ideal blast wave solution.

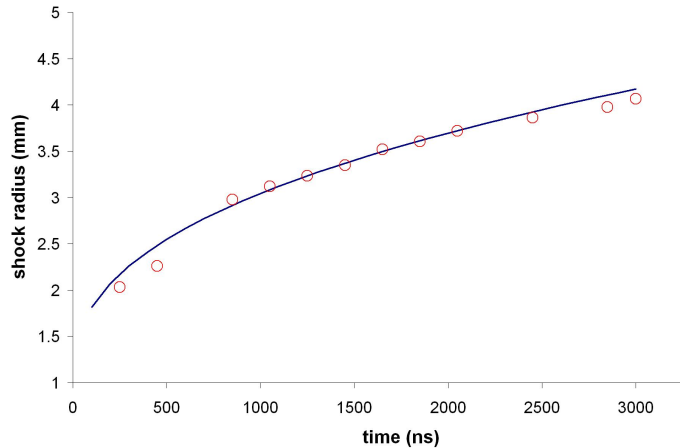


Figure 2.12: *Comparison of the experimental measurements of the shock position (circles) with the Taylor-Sedov self-similar solution. $E = 93$ mJ in air at standard conditions.*

As a result of the breakdown geometry, the shock wave is not perfectly symmetric and the definition of the shock radius is somewhat arbitrary. More importantly, the distribution of velocity and pressure in the region of the plasma core is not as

prescribed by the self-similar solution which is used in Equation 2.17 to estimate the value of the constant α . The range of validity of the self-similar solution is only a fraction of r_a and may become comparable with the dimension of the plasma core. Interestingly, the two characteristic length do not scale in the same way. Taking the ratio of Equation 2.7 to the first of Equations 2.20 one finds:

$$\frac{r_0}{r_a} = b \frac{p_0^{1/3} t_0^{2/5}}{E^{2/15} \rho_0^{1/5}}, \quad (2.22)$$

where b is a constant close to unity. Figure 2.13 shows the ratio of the characteristic lengths $\frac{r_0}{r_a}$ as a function of the deposited energy for air in standard conditions and a 10 ns laser pulse. As shown, for high laser pulse energies, the dimension of the plasma core is very small compared to the range of the self-similar solution. The shock wave leaving the plasma core becomes stronger with increasing value of the deposited energy. The strong shock induces ionization in the surrounding gas and this phenomenon should become more important at high pulse energies. Preliminary experimental observations confirmed this last consideration.

Finally, in the region where the self-similar solution holds, the thermodynamic properties are difficult to describe, due to high levels of roto-vibrational excitation, molecular fragmentation and excitation. This effects are often corrected by defining a effective ratio of the specific heats, used for example in the original description of the nuclear explosion in New Mexico [31] [20]. In reality the ratio of the specific heats varies with r and with t , but considering a variable ratio of the specific heats would invalidate the scaling symmetries that led to the solution, as Equation 2.5 could not

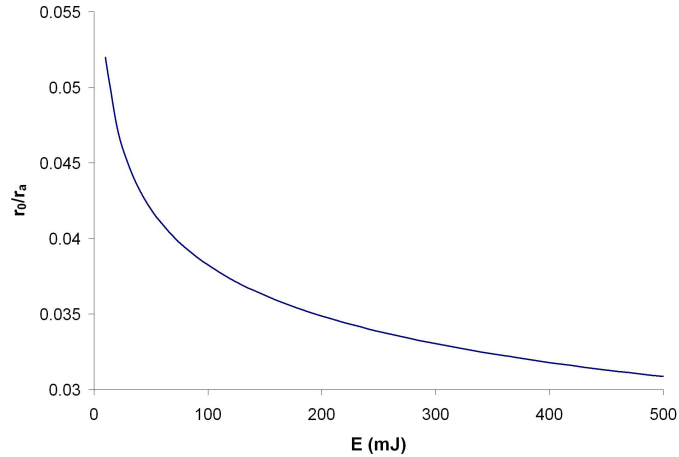


Figure 2.13: *Ratio of the length scales $\frac{r_0}{r_a}$ as a function of the deposited energy for a 10 ns laser pulse in air at standard conditions.*

be used to eliminate the unit of temperature from the formulation of the problem. A numerical study of point explosions accounting for real-gas thermodynamic effects is given in [45].

2.4.3 The numerical solution: comparison with the experiments

In the region described by the numerical solution, where the radius reached by the shock wave is comparable with r_a , the structure of the shock wave is considerably different. As the wave expands over the region of self-similar motion, it becomes more spherical and an expansion wave appears behind the discontinuity. The shock wave is followed by a region of back-flow where the fluid moves toward the center. This expansion wave eventually detaches leaving a region of quiet fluid near the center. These different regions of motion are clearly shown in the shadowgraphs.

The expansion wave appears transparent in the shadowgraphic images, except in a region near the center where the fluid appears as a dark disc due to the high gradients of temperature and density. Figure 2.14 compares the profile of velocity behind the shock wave (from the solution published in [31]) at the two different times corresponding to the different regimes of motion with the corresponding shadowgraphs shown. In these Figures, the region corresponding to the plasma core, where the solution is not accurate, has not been plotted. Since the shock wave travels at sonic velocity with respect to the gas behind it, the motion of the shock wave is not influenced by the behavior of the hot gas in the core. Under these conditions, it is possible to describe the discontinuity as a shock wave propagating in air with standard thermodynamic properties generated by an energy release:

$$E_{eff} = \sigma E. \quad (2.23)$$

The energy E_{eff} is the effective initial energy that would produce the shock observed at large distances in an idealized point explosion with constant $\gamma = 1.4$. The characteristic length and time scales for this portion of the problem will be:

$$r_a = \left(\frac{E_{eff}}{p_0} \right)^{1/3}, \quad t_a = \frac{(E_{eff})^{1/3} \rho_0^{1/2}}{p_0^{5/6}} \quad (2.24)$$

The results of the numerical solution reported in [31] can then be used to describe the flow field far away from the center.

Due to the simplification of the model, the constant σ is much less than 1. Figure 2.15 shows the position of the shock front as a function of time for a deposited energy of 52 mJ in air. The experimental data are compared to the numerical

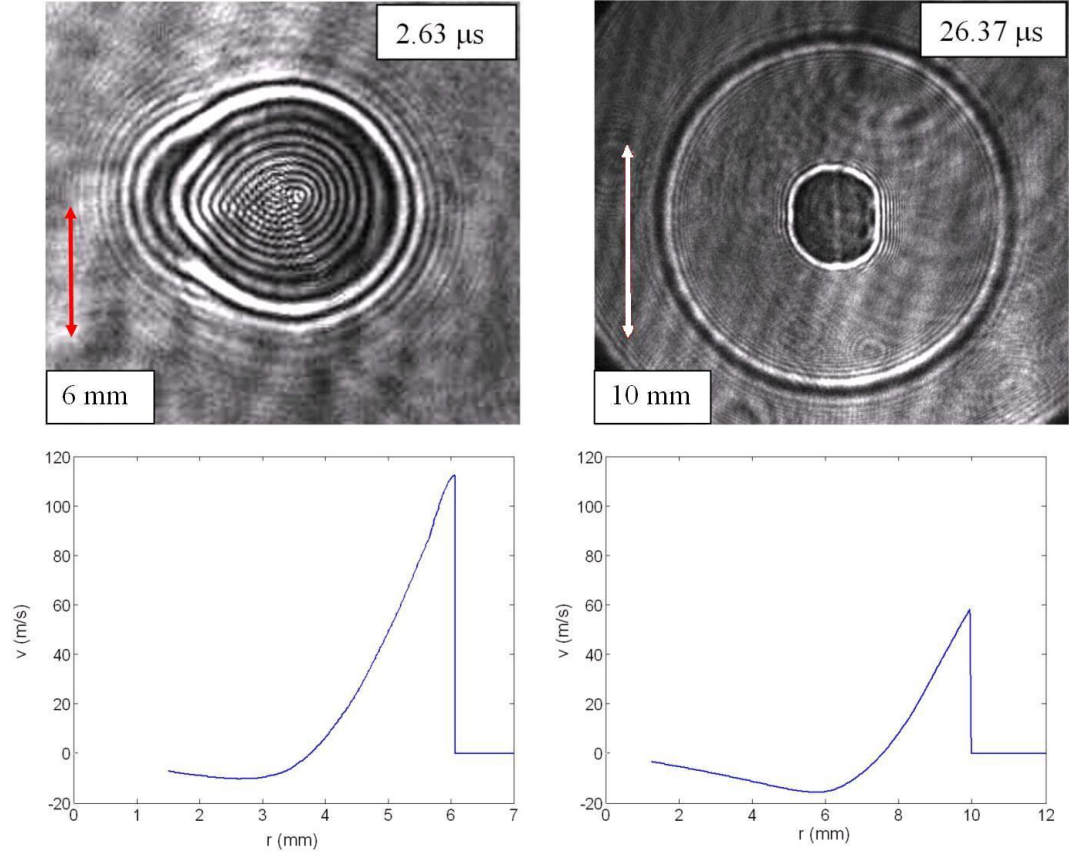


Figure 2.14: *Approximate profiles of velocity behind the shock wave as pictured above in the early stages of the expansion (left column) and in the weak shock region as derived from the solution in [31] assuming spherical symmetry. $E = 87$ mJ in air. The region occupied by the plasma core has not been plotted.*

solution interpolated from Table 2.2, and the constant σ is found to be 0.29. Figure 2.16 shows the full extent of the region encompassed by the numerical solution in Table 2.2, compared to the region analyzed experimentally. Laser plasmas with coupled energies in the range between 52 and 478 mJ are shown in Figure 2.17, which illustrates the experimentally measured shock radius and the nondimensional solution from Table 2.2.

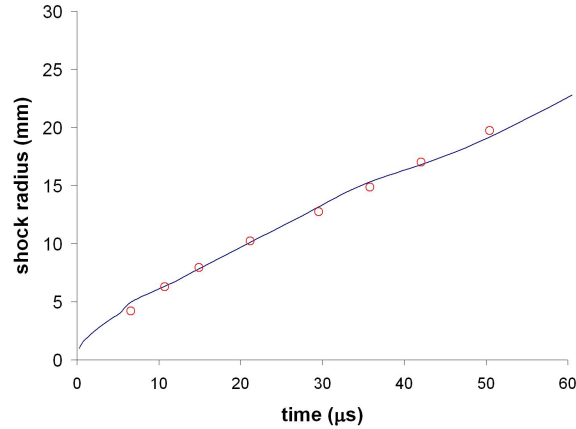


Figure 2.15: *Shock position in air as a function of time. Comparison it of the experimental data (circles) to the numerical solution (solid line, interpolated from Table 2.2). Deposited energy: $E = 52 \text{ mJ}$.*

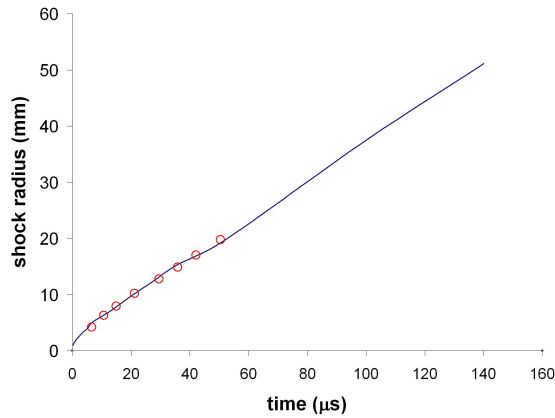


Figure 2.16: *Comparison of the region studied experimentally with the extent of the numerical solution. Deposited energy: $E = 52 \text{ mJ}$ in air.*

More study is needed to gain complete understanding of the shock propagation in real gases; the value of the constant σ changes slightly with high values of deposited energy. For a deposited energy of 478 mJ $\sigma = 0.33$ is the value that best

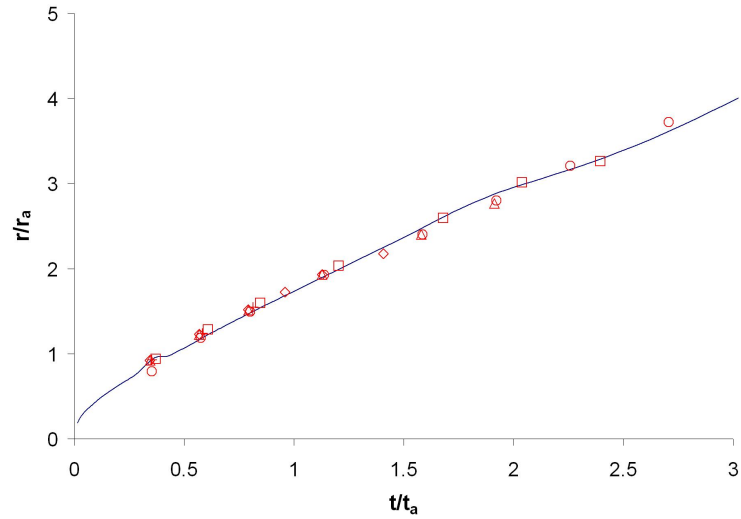


Figure 2.17: *Experimental measurement of the shock radius in air and comparison with the numerical solution. Deposited energies: $E = 52$ mJ circles, $E = 87$ mJ squares, $E = 174$ mJ triangles, $E = 261$ mJ diamonds, $E = 478$ mJ crosses.*

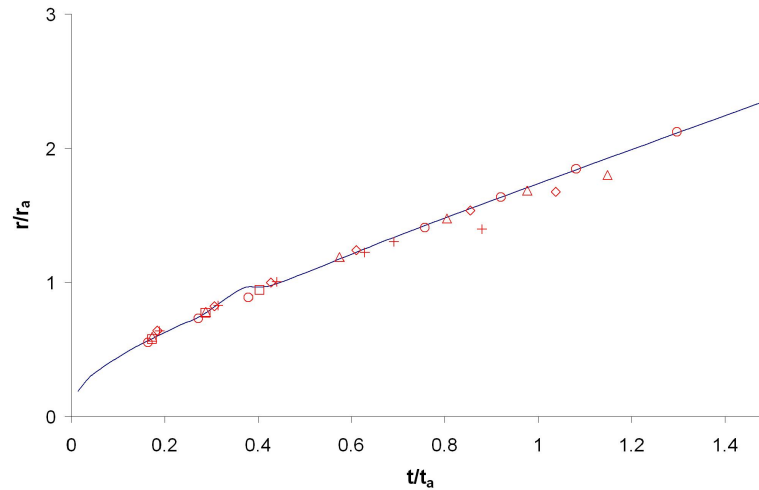


Figure 2.18: *Shock propagation in argon. Deposited energies: $E = 52$ mJ circles, $E = 87$ mJ squares, $E = 174$ mJ triangles, $E = 261$ mJ diamonds, $E = 478$ mJ crosses.*

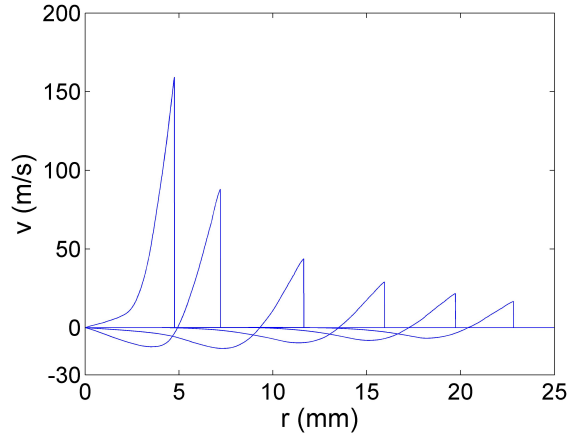


Figure 2.19: *Flow field behind the shock wave at different times as determined from the numerical solution. $E = 87$ mJ in air.*

fit the experimental results. As noted, the numerical simulation makes use of the self-similar solution to derive initial conditions, which is a limitation. Nevertheless, in the range of experimental conditions considered, the numerical simulation can be used to obtain an accurate description of the shock wave generated by laser discharges, provided that the correct value for the coupled energy is used. For example, the data published in [46] fit the simulation with a value of $\sigma = 0.3$. As discussed in [47], results similar to those obtained for air can be used to describe blast waves in gases with ratio of the specific heats in the range between 1.2 and 3. Although the original simulation was carried out for air (with constant $\gamma = 1.4$), plots similar to those presented in Figures 2.15, 2.16 and 2.17 describe, with only the change of a multiplicative constant, the propagation of the shock wave in argon. Figure 2.18 shows the position of the shock wave as a function of time in argon for energy releases in the range between 52 and 478 mJ. In this case the value of the experimental constant σ is found to be 0.96. The apparent difference between air and

argon cannot be interpreted since the multiplicative constant necessary to adapt the numerical results to the case of a monoatomic gas is not given explicitly in [31] and [47]. Figure 2.19 shows the the fluid velocity behind the wave at different instants in time (as derived from the tables in [31]).

2.5 Later Stages of the Expansion

As it expands, the shock wave slows down, matching the speed of sound in the undisturbed gas at long distances. Asymptotic formulas for the blast wave at very large distances from the detonation point were derived by L. D. Landau [50] (see also [51] for a discussion of the the shock wave evolution at large distances). Reflected shocks are still visible in shadowgraphic pictures after they travel for tens of centimeters, as shown particularly in the third image in Figure 2.20. The compressed gas behind the shock wave expands and cools, and the pressure behind the expansion wave is close to ambient. Most of the absorbed laser energy is irreversibly converted into heat and remains deposited in a small region close to the center. Shadowgraphs show a dark, spherical region close to the center, as shown in Figure 2.14 (shadowgraph on the right) and also in the last images of Figure 2.11; the dark region is most probably due to high gradients of temperature and density. In air, the radius of this opaque region is approximately $r = 0.5r_a$ (where r_a is calculated using the effective energy defined in Equation 2.23) over the whole range of pulse energy investigated. A simple model for the distribution of temperature and internal energy can be obtained considering an ideal point explosion with energy release E_{eff} , in a

gas with constant ratio of the specific heats $\gamma = 1.4$. For these conditions, the final distribution of temperature and internal energy was derived by Liñán et. al. [41].

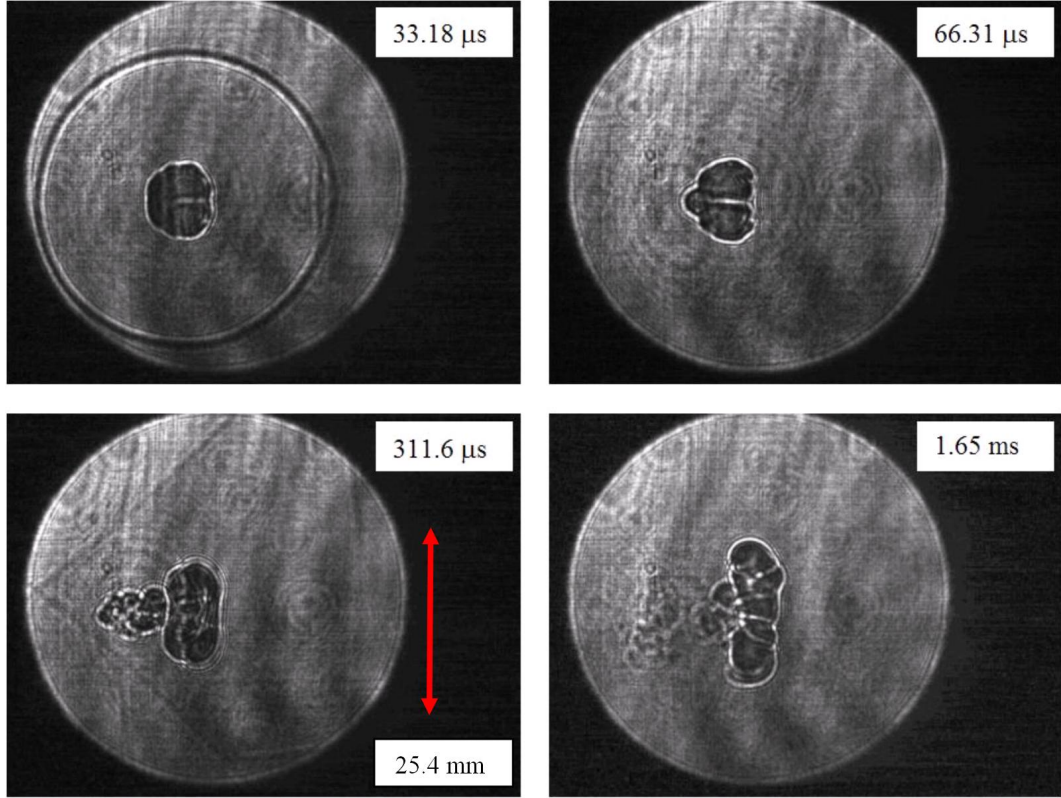


Figure 2.20: *Onset of instability in the hot fluid. $E = 174$ mJ in air; weak reflected shocks are visible in the third shadowgraph.*

The left plot in Figure 2.21 shows the final distribution of temperature as a function of the nondimensional radius. The radius of the opaque region in shadowgraphs, $r = 0.5r_a$, is also shown (with vertical dotted lines). Such distance corresponds to the region where the gradients of temperature tapers off, providing an experimental indication that the temperature distribution is approximately correct. The step profile of the temperature distribution is responsible for the sharp boundary of the opaque disk observed in the shadowgraphs. The plot on the right

shows the fraction of energy stored in the fluid up to the radius r , defined as (see [41] for more details):

$$h = \frac{\int_0^r 4\pi\rho c_p(T - T_0)r^2 dr}{E_{eff}}. \quad (2.25)$$

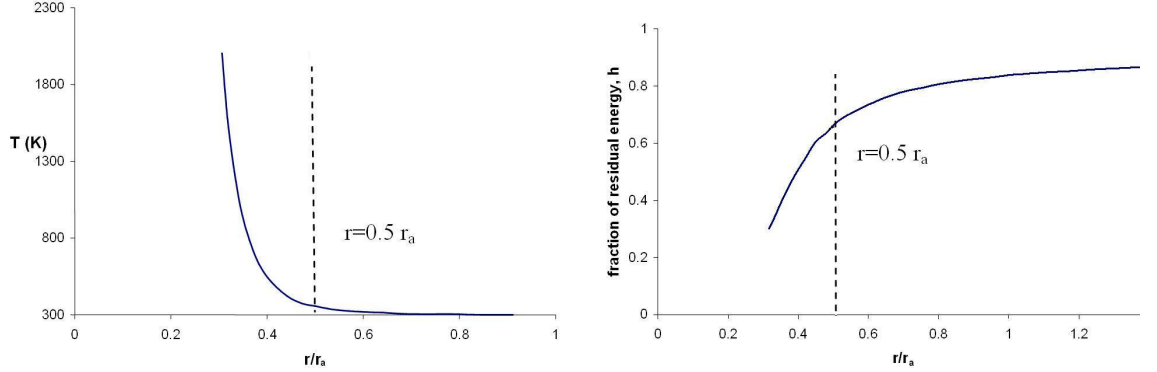


Figure 2.21: *Final distribution of temperature and internal energy for air at standard conditions from [41]. The dotted lines show the radius of the opaque disk.*

These plots are not accurate for small values of r due to real gas effects and the presence of the plasma core, but are more precise at long distances, where the solution matches the experimental observations well. The experimental data suggest that an amount of energy equal approximately $0.33E_{eff} = 0.1E$ is transported by the shock wave farther than $r = 0.5r_a$ and is consumed, producing a relatively small temperature increase in a relatively large mass of gas. After the expansion wave detaches from the central region of fluid, approximately 90% of the deposited energy (85% considering radiation losses similar to those estimated in section 2.2) is still stored in the dark region that appears in the shadowgraphs. The energy used to dissociate the molecules will be released during recombination as discussed

in [45].

The small region of hot gas rapidly cools. At this stage heat conduction and viscosity become important, changing the formulation of the problem. The spherical mass of gas rapidly develops instability (in a time of the order of few tens of μs for the laser energies used in this study) collapsing along the direction of the laser beam with a jet of gas moving toward the laser beam (see also [46]) while a toroidal vortex perpendicular to the direction of the laser beam appears. Figure 2.20 shows the onset of instability in the fluid. The turbulence that is generated dissipates the deposited energy. The time scales involved are too short for the onset of natural convection.

2.6 Radiation from the Plasma

The gas heated by the laser to high temperatures emits bright radiation due to bremsstrahlung and ionic and atomic relaxation. The high temperature associated with the laser breakdown becomes the source for atomic emission spectroscopy. It is useful to analyze the emission of radiation from the plasma and compare it to the time scales identified earlier in this Chapter. Figure 2.22 shows the emission from the plasma during the first few hundred ns. The radiation was detected using a diamond photodiode connected to a fast oscilloscope. Diamond has a large energy gap between two conduction bands. Only the most energetic photons (with energy in the 200 - 2200 eV range [65]) can promote an electron into the empty conduction band, producing an electric signal. For this reason diamond photodiodes are

sensitive only to x-rays and extreme ultraviolet radiation.

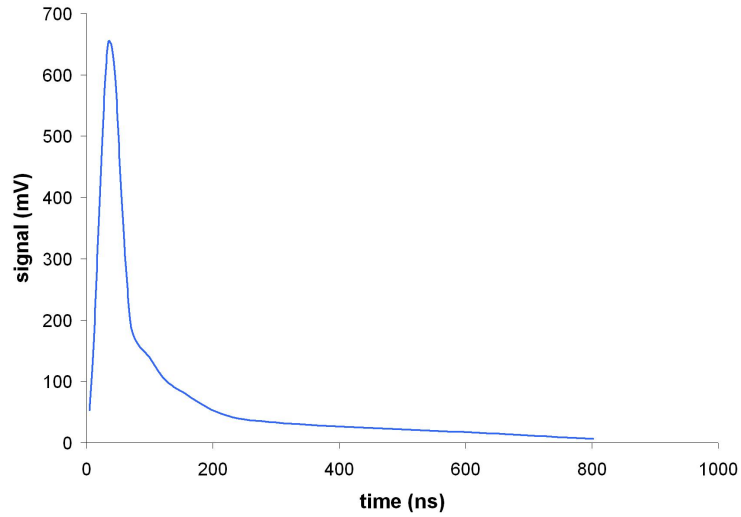


Figure 2.22: *X-ray and extreme UV radiation emitted from the plasma for a 100 mJ laser pulse (approximately 93 mJ of deposited energy).*

As already suggested by the short-time (ns) images of the breakdown, the plasma emits an intense continuum radiation that lasts only few hundred ns, that is, for the very first stages of the fluid expansion. As the plasma expands and cools the continuum radiation fades. Atomic emission lines emerge from the background in less than 1 μs . The intense background radiation promotes a rapid energy exchange within the plasma. A simple model for the atomic emission can be derived assuming the plasma reaches local thermodynamic equilibrium after few hundred ns as a consequence of this energy flux. Although the hypothesis of local equilibrium is not verified for the experimental conditions investigated in this study (see [52] for a recent discussion on the subject), such model is useful for qualitative understanding of some features of the atomic emission from a laser plasma.

2.6.1 Spontaneous emission from a hot plasma

In a cooling plasma the electrons tend to reach equilibrium transferring energy by two mechanisms: spontaneous decay from excited energy levels with the emission of photons and collision with less energetic atoms. A simple model is sometimes used in the literature to describe atomic emission from a laser plasma [48] [49]. Considering a partially-ionized, monoatomic gas where some electrons are promoted to the excited quantum state i , assume that the only relevant electronic process is spontaneous decay from the upper state i to lower states. Further assume that the mechanism of stimulated emission is negligible. The probability per second that a photon with energy $h\nu = E_i - E_k$ (where h is the Planck's constant and ν the frequency of the photon) is emitted, due to the decay of an electron from the upper state i to the lower level k , is:

$$\frac{dP_{ik}}{dt} = A_{ik} \quad (2.26)$$

where A_{ik} (s^{-1}) is the Einstein coefficient of spontaneous emission (see also [53] and [54]).

Assuming the plasma to be in Boltzmann equilibrium at the temperature T at the end of the breakdown, the number of atoms in the state i will be:

$$n_i = n \frac{g_i}{Z(T)} e^{-E_i/kT}, \quad (2.27)$$

where n is the total number of atoms in the plasma volume, g_i is the degeneracy of the state i , Z the partition function and k the Boltzmann constant. For a partially-

ionized gas it is important to consider the probability W_q of an atom to be in the ionization state q . The number of atoms per second that undergo a transition between the states i and k is:

$$n_i \frac{dP_{ik}}{dt} = n \frac{g_i}{Z(T)} e^{-E_i/kT} A_{ik} W_q \quad (2.28)$$

In the case that absorption is much slower than spontaneous emission (for example in a rapidly cooling plasma), the radiant power per steradian can be approximated by multiplying Equation 2.28 by the photon energy, $h\nu = h\omega/2\pi$ and dividing by the solid angle 4π giving:

$$I_{ik} = n \frac{g_i}{Z(T)} e^{-E_i/kT} \frac{h\omega}{8\pi^2} A_{ik} W_q \quad (2.29)$$

It appears that, all other parameters being equal, the intensity of an atomic line depends on the number of atoms of a given element in the plasma volume, and therefore on the analyte concentration. The approximate model of Equation 2.29 implies that the number of transitions (and therefore the line strength) depends on two parameters: the instantaneous plasma temperature and the transition probability A_{ik} . The experimental measurements presented in the next section show that the lifetime of atomic emission depends on both parameters.

The plasma temperature determines the equilibrium distribution of the electron population between the various energy levels [55]. It will be shown that emission of spectroscopic lines from laser-produced plasmas cannot be explained without taking into account transient phenomena related to the plasma temperature evolution.

2.6.2 Lifetime of the atomic emission

The light from the plasma is focused on the tip of an optical fiber connected to the entrance slit of a 0.3 m Acton spectrometer. The light is dispersed by a 600 grove/mm grating and imaged on the chip of a Roper Scientific PI-Max ICCD camera. The electronic shutter of the camera is synchronized with the laser. a detailed description of the experiment is given in Appendix A.3.

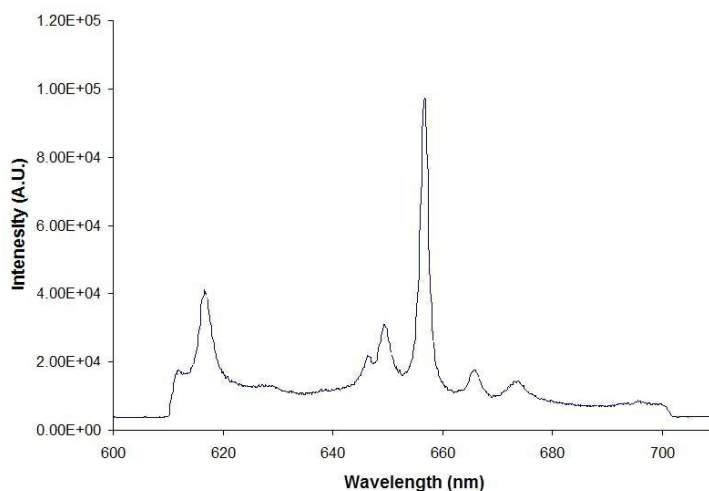


Figure 2.23: *Emission spectrum of the Balmer- α line of hydrogen, taken few μs after the breakdown.*

Figure 2.23 shows the emission spectrum from a laser-induced plasma in air. The most prominent line is the 656 nm Balmer- α line of hydrogen from the water vapor in the atmosphere. Figure 2.24 shows the time evolution of the Balmer- α line. Each spectra in the graph was acquired with 1 μs exposure of the camera, starting 1 μs after the breakdown and increasing the delay 1 μs each time (i.e., camera gating 1 μs , delay 1 μs , 2 μs , 3 μs ...).

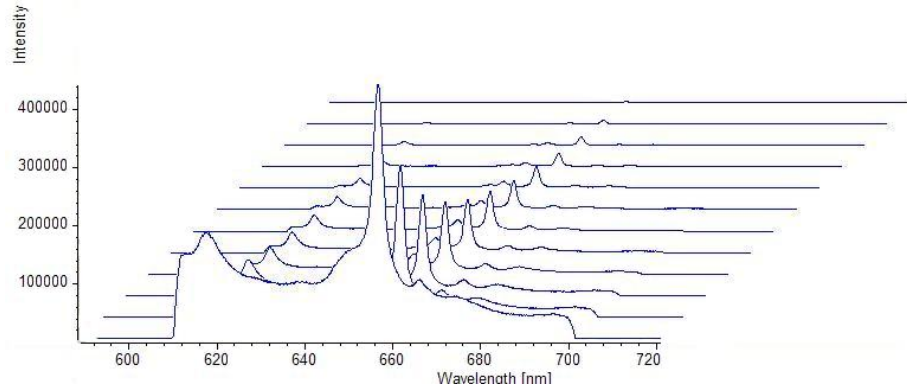


Figure 2.24: *Evolution in time of the Balmer- α line of hydrogen.*

The line rapidly diminishes over a few tens of μs . Figure 2.25 shows the intensity as a function of time for the Balmer- α line and for the 745 nm line of nitrogen (from atmospheric nitrogen), for different laser pulse energies. As the energy deposited increases, the plasma temperature and volume increase, as described by in Section 2.3.2. Hence at a given time the local temperature is increased with greater energy deposition, increasing the number of excited atoms within the plasma volume and intensifying the atomic emission.

The lifetime of the atomic emission also increases with increasing laser energy. Both N and H lines share the same behavior. For every laser pulse energy investigated, the emission lasts through the first stages of the plasma expansion, when the rarefaction wave develops behind the spherical shock wave. In each case the emission decays well before the onset of instability in the fluid. The lifetime of the emission depends on the quantum properties of the transition (such as A_{ik} and the

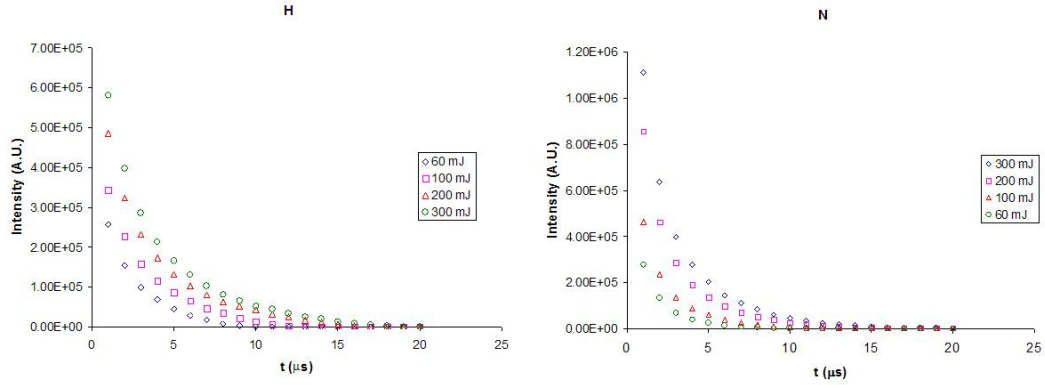


Figure 2.25: *Intensity of the 656 nm H line and 745 nm N line as a function of time for different laser pulse energies.*

energy difference between the quantum levels involved in the transition). Generally, spectroscopic measurements are carried out during the early stages of the plasma expansion. For many atomic lines the lifetime is of the same order of magnitude as t_a , the timescale of the weak shock wave. Figure 2.26 shows the intensity of the 656 nm H line normalized by the signal at 1 μs .

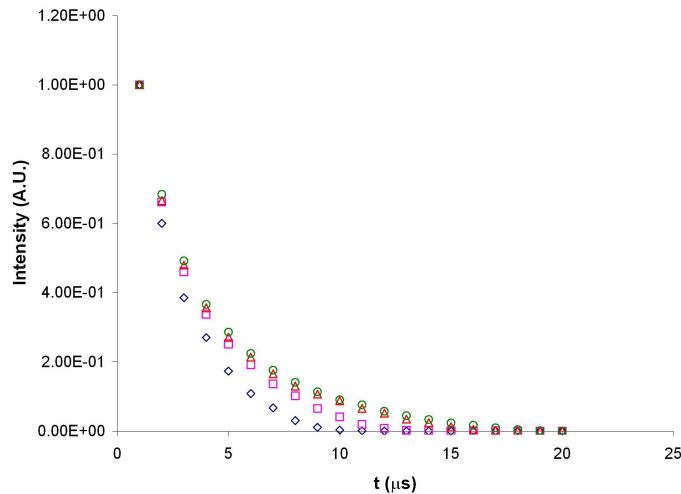


Figure 2.26: *Normalized intensity of the 656 nm H line as a function of time for different laser pulse energies.*

Even when normalized, the lifetime of the emission increases as the energy release increases. This is attributed due to the different temperature and different cooling rate of the plasmas. However, the intensities presented in Figure 2.25 do not scale with t_a . The spontaneous emission from a laser plasma has two characteristic times: the reciprocal of Einstein spontaneous emission coefficient, $1/A_{ik}$ (s), and the acoustic time, t_a , of the shock wave. Before the onset of instability, the cooling rate of the plasma as a function of the deposited energy scales with t_a (as discussed in sections 2.4.1-2.4.3). Hence the parameter $1/A_{ik}$ is related to radiation decay by spontaneous emission (see [54]) while t_a is related to the temperature decay rate. The lifetime of an atomic line depends on both the temperature history of the plasma and the spontaneous decay of excited states. Indeed, for a 100 mJ laser pulse the acoustic time is $t_a = 33 \mu s$ and $1/A_{ik}$ for the 745 nm N line is on the order of 100 μs (data from the NIST atomic spectra database [56]). The two characteristic times have similar orders of magnitude. Quantitative description of atomic line emission requires an accurate modelling of many plasma parameters [57] [58] [59] [60] and cannot be solved with the simple approach discussed here. However, the concepts outlined in this section are important for the correct quantification of spectroscopic measurements as discussed in Chapter 3.

2.7 Conclusions

Four different regimes are attained during the breakdown of focused laser pulses in air. Each regime is characterized by different length and time scales (or by the lack

of them).

- The energy-release timescale is defined by the duration of the laser pulse. The corresponding length scale r_0 , is given by Equation 2.7. In this phase the rapidly expanding plasma can be described as a strong shock that produces an optically thick absorption zone. The laser pulse is absorbed in this thin layer, resulting in a Laser Supported Wave travelling along the beam direction, towards the laser. The gas behind the wave expands adiabatically, resulting in a lower plasma temperature near the center. At the end of the laser pulse the volume of the plasma is found to be proportional to r_0 . The plasma volume defines the region where the known energy E is stored, and thus the maximum internal energy of the fluid.
- The rapidly expanding gas sends a strong shock wave into the cold gas, transferring energy to layers of fluid outside the initial plasma core. For the experimental conditions analyzed in this paper, the continuous radiation produced by Bremsstrahlung fades in a time of the order of $\sim 10t_0$. The shock that leaves the plasma can be described as a strong shock without a characteristic length or time scale. However, for pulse energies commonly used in laboratory measurements, the strong shock region is small and can become comparable with the dimensions of the plasma core. For this reason the Taylor-Sedov theory cannot be used to derive accurate estimates of the distribution of temperature and velocity from experimental observations.
- When the ambient pressure becomes comparable with the pressure behind

the shock, the characteristic length and time scales are given by Equations 2.20. An expansion wave develops behind the shock and a region of back flow appears. The shock soon becomes too weak to create significant temperature gradients in the fluid and the region behind the wave appears clear in the shadowgraphs. At this stage the propagation of the wave can be described by the model of a weak blast wave propagating in air. However, due to real gas effects occurring during the first stages of the expansion, the energy apparently coupled into the shock is only a fraction of the laser pulse energy. Once this is taken into account, the model can be used to accurately predict the position of the shock wave in time, for laser pulses in the range between 40 and 550 mJ.

- At infinity the shock wave becomes a sound wave. Due to viscous effects behind the shock wave, most of the laser pulse energy is irreversibly converted into heat in a region with radius $r = 0.5r_a$. The model of a point explosion describes well the experimental observations and can be used to derive accurately the final energy and temperature distribution. In particular, for air, almost the 90% of the laser pulse energy remains confined within a radius $r < 0.5r_a$. Instability rapidly develops in the fluid, and the resulting turbulence dissipates the energy in a time on the order of milliseconds (for the laser pulse energies investigated in this paper). At this stage viscosity and heat conduction become important and have to be taken into account in the formulation of the governing equations.

Atomic emission lines appear less than one μs after the breakdown and last, for the laser pulse energies used in these experiments, few tens of μs . The lifetime of the atomic emission is comparable with the timescale of the weak blast wave, when the expansion wave develops behind the shock wave. For the laser pulse energies normally used for spectroscopy, the spontaneous emission fade before the onset of instability in the fluid.

The models presented in this Chapter could be improved by performing numerical simulations. Computational models can be developed to describe the hydrodynamics of the laser breakdown starting from the beginning of the laser pulse. The results could eventually be coupled to radiation models to simulate emission spectra. However, the scaling laws described here are important as they outline a convenient formulation of the problem. In particular, the length scales r_0 , t_0 , r_a and t_a should be used to present results from experiments or models in a non-dimensional form. Furthermore, the scaling symmetries described in this Chapter provide an excellent way to validate numerical results. In particular, computational models should predict similar values for experimental constants such as β , \mathbb{V} and σ and fit the plots presented in Figures 2.6-2.7 and Figure 2.17, as well as describing the structures observed at latest stages of the expansion (Figures 2.21 and 2.20). The results of these studies may have important applications in the field of laser spectroscopy and nuclear fusion.

Chapter 3

Spectroscopic Measurements of Hydrocarbons

3.1 Optical Measurements of Gas Composition

Chapter 2 was devoted to the description of the laser-induced plasma temporal evolution. Motivation for that work was to investigate the physics phenomena that lead to the emission of spectral lines. In the second part of this dissertation, the concepts developed earlier in this work are applied to gas composition measurements. In particular, LIBS will be used to measure the fuel-to-air ratio in a mixture of air and hydrocarbons. It will be shown that quantification and repeatability of spectroscopic measurements depends critically on understanding the influence that experimental parameters, such as laser pulse energy and detector timing, have on atomic emission. As already discussed in the first Chapter, the mole fraction of a combustible mixture is one of the key parameters that controls combustion efficiency

and pollutant emissions. In combustion research, the mole fraction of a mixture is often defined in function of the stoichiometric fuel-to-oxidizer ratio, F_s/A_s :

$$\Phi = \frac{F/A}{F_s/A_s}. \quad (3.1)$$

In the remainder of this manuscript, the equivalence ratio, Φ will be used interchangeably with the mole fraction to characterize the composition of a gas.

3.2 Method

A detailed description of the experimental apparatus is given in section A.3 of the Appendix. Gases are mixed in a cross flow arrangement before exiting into room air through a ceramic honeycomb. A curtain flow of argon surrounds the premixed stream to stabilize the flow. A Nd:YAG laser is used to generate the plasma, the pulse energy was varied between 48 and 366 mJ. This introduces sufficient energy to create the plasma such that large fluctuations in plasma temperature (and hence plasma emission) are avoided [61]. The breakdown takes place approximately 2 mm above the center of the burner. The spatial resolution of the measurement can be estimated from the characteristic dimension of the plasma, a few mm as discussed in the previous Chapter. The emission is collected at right angles with respect to the laser beam, and the plasma light is coupled into a spectrometer. The ICCD camera mounted to the spectrometer is controlled by a triggering signal from the laser Q-switch. The time-resolved measurements are characterized by two parameters: the delay time with respect to the triggering signal (delay) and the aperture

time of the camera's electronic shutter (gate width).

Approximately $1 \mu s$ after the plasma initiation (and in the absence of radiationless transitions, see discussion in Section 3.6), the intensity of a single atomic line can be described by equation 2.29. One important consequence from Equation 2.29 is that the intensity of a given line changes with time as the plasma cools. Each atomic line has an optimal temporal detection window determined by the elemental ionization energy and the excitation energy of the specific transition under consideration. This optimum changes with the characteristics of the plasma, in particular the temperature, which at a given time is a function of the laser pulse energy. A possible method to normalize for pulse-to-pulse variations in the laser energy is to normalize the peak intensities by the continuum background emission [2]. Similar results can be obtained taking the ratio of two emission lines and, to the extent that a set of lines have similar energies and transition probabilities, line ratios are often more repeatable than absolute line intensities.

A typical averaged LIBS spectrum of a mixture of air and hydrocarbons (from engine exhaust) in the 700 to 790 nm spectral region is shown in Figure 3.1. This spectral region contains strong atomic lines of C, N, and O. Three peaks of N at 741, 743, and 746 nm (a triplet generated by the fine splitting of the $2s^2 2p^2(^3P)3s - 2s^2 2p^2(^3P)3p$ transition), and a peak of O at 777 nm (also a triplet that cannot be resolved with the spectrometer used in the experiments) at 777 nm are clearly visible. C appears in the spectrum in two different forms: an atomic peak at 711 nm comprised of several overlapped lines, and a broad CN molecular emission from several vibrational transitions (degraded to the red) in the

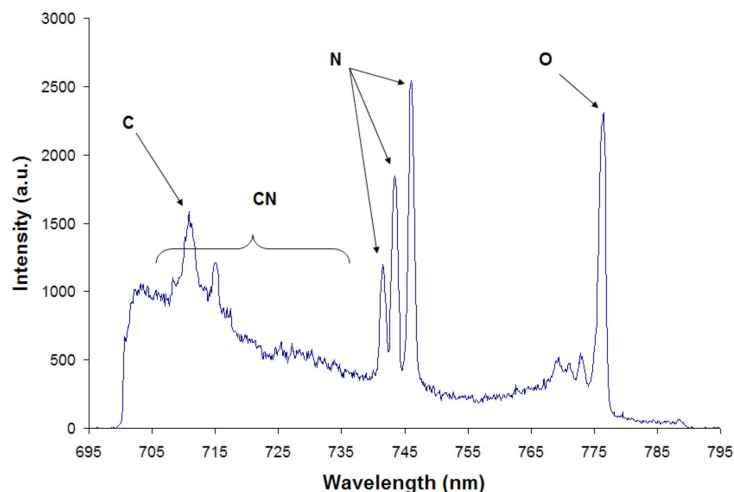


Figure 3.1: *LIBS spectrum of a mixture of air and hydrocarbons in the region between 690 and 790 nm.*

$A^2\Pi - X^2\Sigma$ electronic transition in the range from 708 to 734. The CN emission arises from recombination of C and N generated in the plasma into electronically excited CN^* . Additionally, weaker CN bands have band heads at 725.9 nm and at 743.7 nm, the latter band head underlying the nitrogen peaks. At lower wavelengths, the $B^2\Sigma - X^2\Sigma$ CN band, degraded to the violet (with band heads at 359, 388, and 421 nm) represents the brightest emission in the entire spectral region between the ultraviolet to the near infrared.

To obtain the intensities of particular spectral lines, a linear baseline is fit to the peak. This baseline is subtracted from the integral of the peak to correct for the presence of background radiation. From Equation 2.29, as the intensity of each spectral line is proportional to the number of corresponding atoms in the plasma volume, to first order (in the absence of interferences) relative concentrations of elements can be determined by taking the ratio of the integrals of corresponding

elemental peaks. It is important to note that this way of defining the spectral intensity is somewhat arbitrary. In particular, as shown in Figure 3.1, the background signal is much stronger in the region of the 711 nm C peak than in the region of the N and O peaks. For consistency, the algorithm used to compute the spectral intensity is unchanged throughout the measurements, i.e., the peaks are always defined in the same way.

3.3 Spectroscopic Measurements of the Equivalence Ratio

Figure 3.2 shows the comparison between 300 single shot measurements taken in each of three different mixtures of air and propane: 0% (pure air), 1% propane by volume, and 2% propane by volume. Each data point represents the ratio of the signal from the 711 nm carbon line to that of the combined 746 nm N line and 777 nm O line, as obtained from individual laser pulses. The delay and gate for these measurements were 3 and 15 μs respectively, and the laser pulse energy was 86 mJ. The relative standard deviation is between 2.7% and 3% of the mean value for each of the three data series and the variation of the data about the mean value follows a Gaussian distribution, typical of a Poisson process. The offset reported in the ratio on the y axis in Figure 3.2 for pure air is a result of the data processing. The spectra show that the intensity of the 711 nm C peak does go to zero in pure air, but a large background is still present.

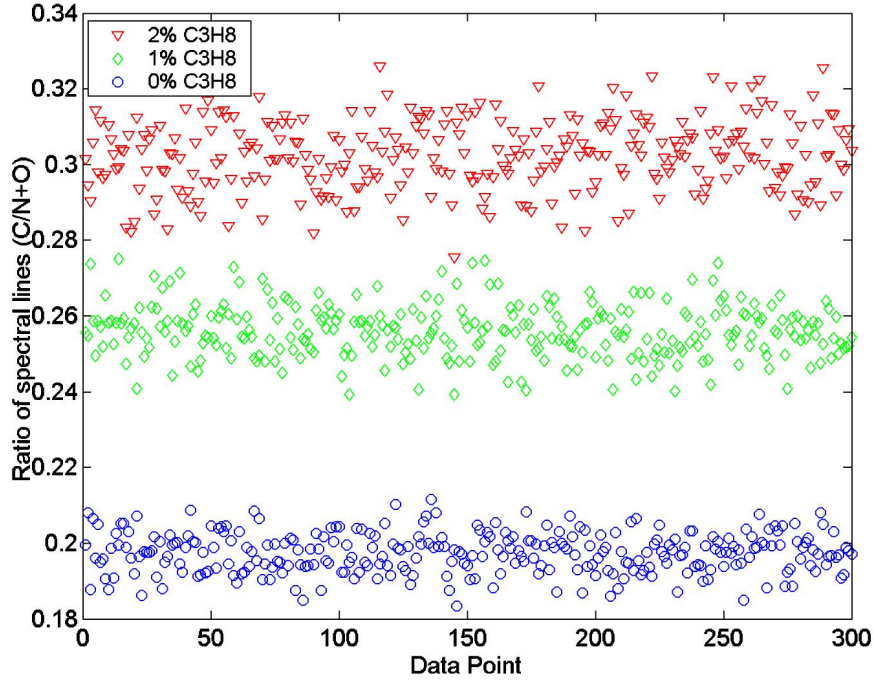


Figure 3.2: *Ratio of the integrated spectral peak area of the 711 nm C to the combined signal from the 746 nm N line and 777 O line obtained in different mixtures of propane and air: 0% C_3H_8 (circles), 1% C_3H_8 (diamonds), and 2% (triangles). All measurements were taken with a delay and gate of 3 and 15 μs respectively.*

The background is most probably due to the effect of the CN band (CN is highly luminous and the signal from the 400 ppm of CO_2 present in air might still be visible) or to the overlap of some other molecular band. Since the origin of the background is not investigated in this here, it is not appropriate to subtract the signal due to background radiation. In order to better explain the effect of laser power on the background (see section 3.3.3) the measurements are presented un-normalized. As shown in the next sections the presence of the offset in the y axis does not compromise the technique. The spectrum presented in Figure 3.1 presents

many features that can be related to the equivalence ratio. For example the absolute intensity of the C, N or O lines, or any combination of them, can be used to obtain a measure of the fuel/oxidizer concentration. As above the combination of C/N + O, provides the best signal to noise ratio and is be used throughout this Chapter unless specified. The single-shot data in Figure 3.2 were acquired at 10 Hz. Hardware limitations control the repetition rate of the measurement. The actual time required for acquisition of a single measurement is only slightly more than the sum of the delay and gate width of the detector, i.e. 18 μs or less in these measurements. Hence LIBS could be employed in high speed flows where fluctuating velocities are on the order of meters per second or faster.

The data in Figure 3.2 illustrate the potential of LIBS to yield quantitative information on the composition of an unburned mixture of air and hydrocarbons. To investigate the potential of LIBS in combustion applications it is necessary to investigate the behavior of each atomic line as concentrations of fuel and oxidizer are varied over a wide range.

3.3.1 LIBS Measurements in a Combustible Mixture

Measurements in a flame, or in a combustible fuel-air mixture, can be obtained in a similar manner to the data presented in Figure 3.2; the background luminosity of a flame and atomic chemiluminescence are negligible compared with plasma emission in these time-gated measurements. However, LIBS measurements in combustible mixtures have some obvious drawbacks. In particular, the typical pulse energies

needed to form a breakdown using a nominally 10 ns Nd:YAG pulse are sufficient to ignite flammable hydrocarbon/air mixtures. The first measurement is not affected by ignition since the time required for data acquisition (μs) is much smaller than the time scales required for ignition, but repeated measurements under similar conditions in flammable premixtures would require extinguishment between laser pulses or sufficient time between measurements (on the order of a fraction of the second for the present measurements) for a flame to regain equilibrium following the expansion caused by the plasma. These considerations depend on the application, in particular on the flow velocity, equivalence ratio, and plasma energy. For the 10 Hz measurements performed in combustible mixtures in this work, a significant effect on the flame structure was not observed.

For some in-flame measurements, beam steering was observed to interfere with plasma formation. The index of refraction of a gas depends on temperature, and thus as rays of the focusing laser beam encounter the flame, they are diffracted according to Snell's law. The gradient of the index of refraction is expected to be roughly normal to the flame surface, which is non-uniform. The steering of each portion of the beam is thus different, potentially defocusing the beam and/or moving the focus. Practically, the effects of such aberration depend strongly on local conditions and may be observed by plotting the fraction of laser energy transmitted through the plasma as a function of the mixture composition in a particular flow geometry. In the absence of such aberration, approximately 90% of the laser energy is absorbed during the breakdown event and the remainder is transmitted [32].

Figure 3.3 shows the percentage of transmitted energy for a 117 mJ laser

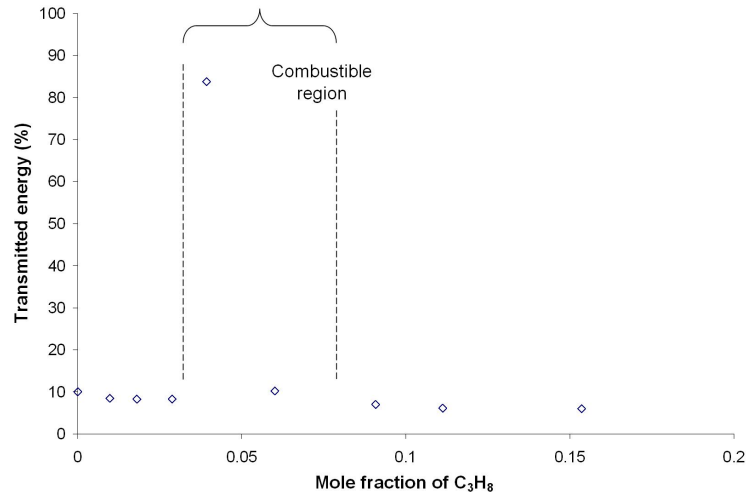


Figure 3.3: *Transmitted laser pulse energy as a function of propane concentration.*

pulse as a function of the mole fraction of propane in air. The energy absorbed in the plasma is close to 90%, in accord with the data reported in literature [32] [34], except for the data point in a nearly stoichiometric propane and air flame, in which the transmitted energy is almost 72%. Neglecting this aberrant point, a slight dependence of the absorbed energy on gas composition is observed in Figure 3.3, consistent with results published in literature that suggest the deposited energy depends slightly on the gas composition [33].

Figure 3.3 illustrates that for these experimental conditions, optical aberration is only important for mixtures near stoichiometric. The decrease in absorbed energy is not observed in a rich flame (0.06 mole fraction of propane in air), and was also not noticed in other experimental settings, in particular during measurements in a turbulent flow of hot exhaust gas from an engine ($T > 600$ K). The problems associated with optical aberration in flames can be avoided by increasing the laser power such that the absorbed energy always exceeds the effective breakdown thresh-

old. For example, in the near-stoichiometric flame through which 72% of the laser pulse was transmitted, the pulse energy corresponding to breakdown (in air or in rich mixtures) is increased from approximately 54 mJ to 94.5 mJ. Measurements of the absorbed energy at a given detector delay and gate allows quantification.

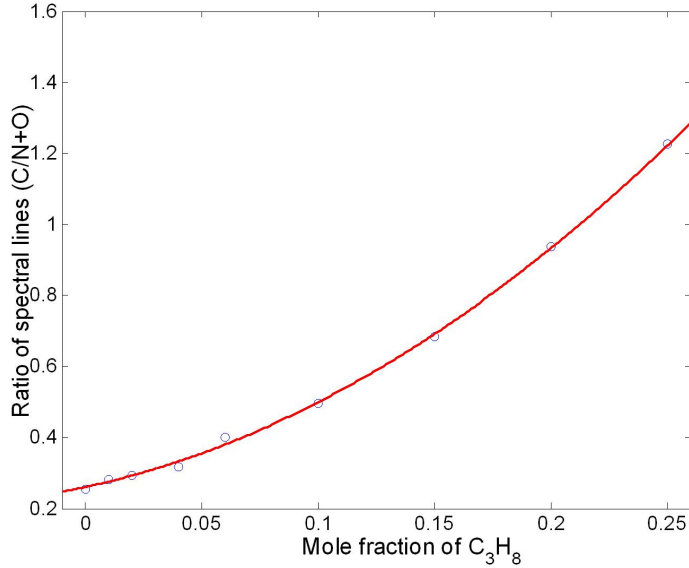


Figure 3.4: *Averaged LIBS signal as a function of the mole fraction of propane, delay 1 μ s, gate 5 μ s.*

Figure 3.4 shows the LIBS ratio of the 711 nm C line to the combined of N and O lines at 745 and 777 nm respectively, over a wide range of mole fractions of propane in air. These measurements were taken with a delay of 1 μ s and a gate width of 5 μ s, and a constant energy (90 ± 5 mJ) deposited in the plasma. The variation in absorbed energy due to gas composition is modest (< 2 mJ) and is ignored (see discussion in the next Section). Each data point in Figure 3.4 is an average of 300 laser shots; given the Poisson distribution of the single shot data (Figure 3.2) it is expected that the standard deviation of the averaged data scales as $\frac{1}{\sqrt{N}}$, where

N is the number of averaged measurements, and the estimated standard deviation for the average of 300 shots is less than the 0.2% of the mean value. Other sources of systematic error (e.g. rotometer values) may be significant and could explain some fluctuations in the data, but are not included here. As observed in Figure 5, with this choice of delay and gate, the LIBS ratio of C/(N+O) describing mixture fraction of C₃H₈ between 0 and 0.25 can be fit with good accuracy ($R^2 < 0.99$) with a second order polynomial.

Figure 3.4 illustrates quantitative concentration measurements with LIBS using an experimental calibration. A detailed calibration curve is required for each specific application. Determination of laser absorption on a shot-to-shot basis was necessary to compare measurements taken in cold gases to some of those taken in flames due to the fluctuating absorption of the laser. In the case of turbulent flame measurements multiple energy-dependent calibrations would be required, and measurements of the absorbed energy with each shot would allow proper quantification for a measured laser absorption. In general, depending on the absorbed energy, detector timing and range of concentrations, the relation between the LIBS signal and concentration may be nonlinear, and the choice of experimental parameters depends on the actual application. The influence of experimental parameters, in particular laser pulse energy, detector timing, and the chemical matrix, on the LIBS measurements is the subject of the remainder of this Chapter.

3.3.2 Effect of laser pulse energy on atomic emission

As already discussed, the instantaneous intensity of the atomic emission depends on the plasma temperature. Plasma volume, temperature and cooling rate depend strongly on the energy coupled in the breakdown. Therefore, the absolute intensity of an atomic peak depends on the fraction of the laser pulse energy that is actually absorbed in the plasma. For each value of the fuel-to-air ratio, and for each choice of delay and gate, increasing the laser energy increases the emission of N, O and C.

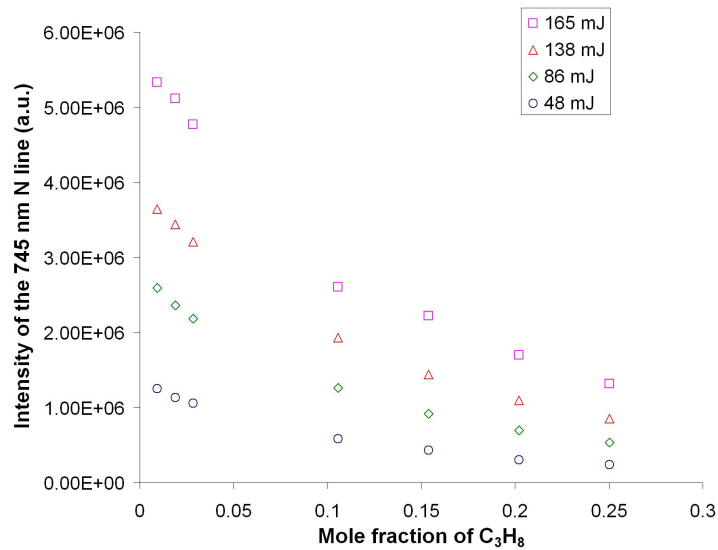


Figure 3.5: *Absolute intensity of the 745 nm N line as a function of laser pulse energy for different concentrations of propane in air, with delay and gate each 1 μ s.*

Figure 3.5 shows the intensity of the 745 nm N line as a function of the concentration of propane for several values of pulse energy ranging from 48 to 165 mJ. Each data point is derived from a single 10-shot average spectrum taken with a delay and gate of 1 and 5 μ s, respectively. Based on statistics of the data in Figure 3.2, the fluctuations due to shot to shot instabilities are on the order of 1% of the

mean value for a 10 shot average. As illustrated, line intensity decreases almost linearly with increasing concentration of fuel, and the behavior is similar for each pulse energy. Therefore, it should be possible to produce a calibration curve similar to Figure 3.4 for each laser pulse energy.

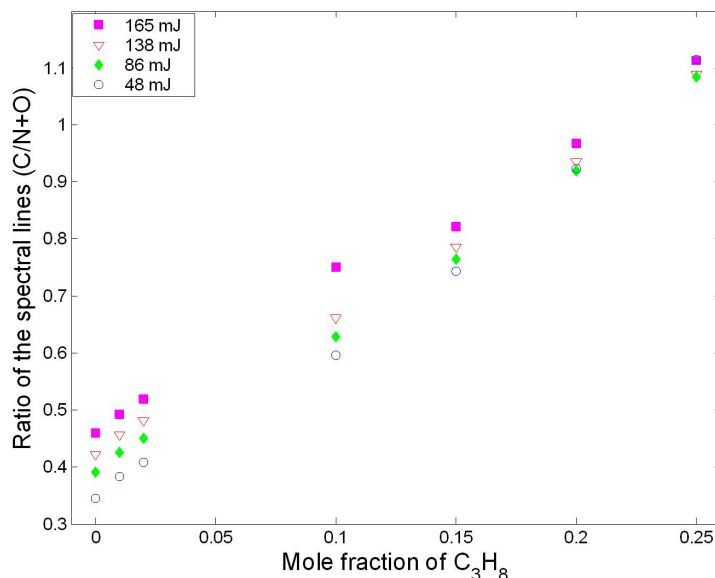


Figure 3.6: *Ratio of atomic lines (C/N+O) as a function of laser pulse energy for different concentrations of propane in air, with delay and gate each $1\mu s$ respectively.*

Figure 3.6 shows the ratio of the 711 nm C line to the combined signal of the 745 nm N and 777 nm O lines. In a given measurement there are three measurands, C, N and O, which in principle allows the solution of up to three variables (although in this case N and O are directly related and thus not independent). Provided that calibration curves (or suitable interpolations) are known for each value of the laser pulse energy, two lines (C and one of the others) can be used to solve for pulse energy and hydrocarbon concentration. It is interesting to note that the intensity of the signal reported in Figure 3.6 for pure air (0% mole fraction of propane)

depends on laser power, because the intensity of the background depends on laser power. In these experiments the background was subtracted by fitting a baseline under the peaks. The baseline was determined by averaging a few points at fixed locations on each side of the spectral feature. This simple approach, unchanged for the different measurements, does not fully compensate for the effect of laser power on the background (which changes, for example, the peak width). Therefore, the computed spectral intensity seems to change as a function of the laser energy. Again, this phenomenon does not present a significant problem once the effect of the experimental parameters is known in detail.

3.3.3 Lifetime of the atomic emission as a function of laser pulse energy

The discussion in the preceding section illustrates the effect of laser power as a function of hydrocarbon concentration. Figure 3.5 shows that nitrogen emission intensity decreases with concentration of propane. Moreover, the ratio of the C to the N and O lines shown in Figure 3.6 is dependent on the laser pulse energy. An increase in the effective lifetime of the emission with increasing laser pulse energy is one of the primary reasons for this variation. As discussed in Section 2.6.2, the lifetime of the 745 nm N line increases as the energy coupled into the plasma increases (Figure 2.25). The 711 nm C line and the CN molecular emission have similar behavior, but decay more slowly than the N and O lines, which have almost identical temporal behavior.

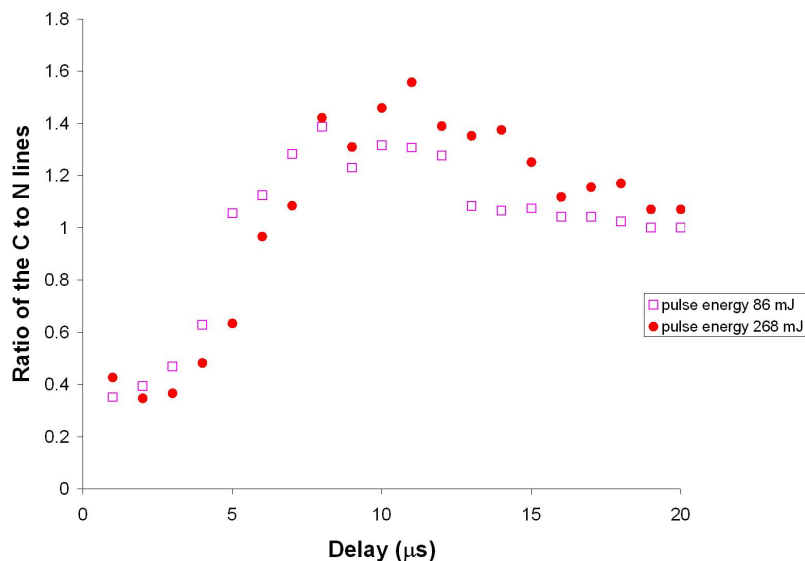


Figure 3.7: *Ratio of the normalized C to N spectral lines as a function of time for two different laser powers (86 mJ squares and 268 mJ circles), with a 0.1 propane mole fraction for both measurements. Each point is obtained averaging 10 laser shots*

Figure 3.7 shows the ratio of the 711 nm C line to the 745 nm N line alone (each atomic line has his own characteristic lifetime, for simplicity the behavior of only two lines is compared) at two different pulse energies for 0.1 mole fraction of propane in air, acquired with a gate width of 1 μs . At first the ratio increases in time, because the N line decays faster than the C line. The C to N ratio reaches a maximum during the later stages of the plasma, when the C emission is actually stronger than those of N. At these timings the absolute intensity of the atomic lines has decreased more than ten times from their maximum value, and the fluctuations in the data are due to low signal to noise ratio. Eventually the ratio approaches unity as the plasma cools and both lines disappear in the background noise. With increasing laser energies the curves shift in the direction of increasing time. There are two main implications

of the observed behavior for LIBS measurements of hydrocarbons:

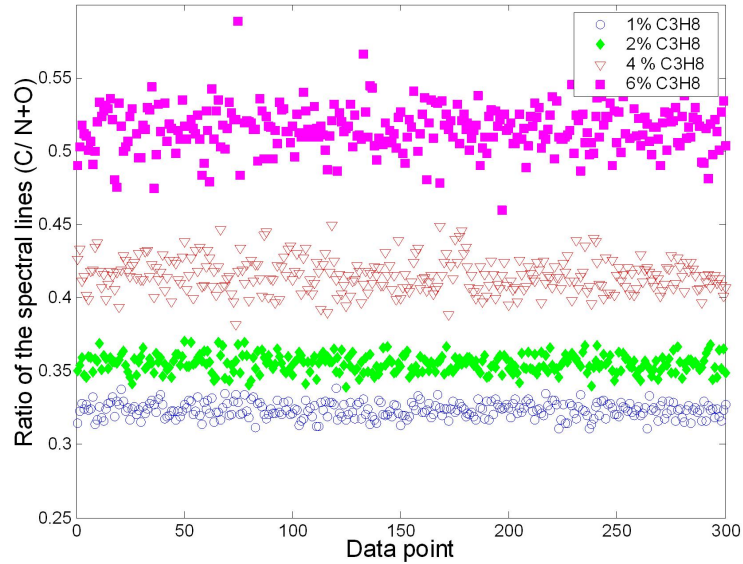


Figure 3.8: Comparison of LIBS measurements taken in a flame (squares) with measurements taken in a cold mixture (circles, diamonds and triangles), taken with a delay and gate of 1 and 5 μ s, respectively.

- First, performing measurements at shorter times (shorter delay and gate) captures less C emission, eventually reducing the sensitivity at very short times. Figure 3.8 shows single shot data obtained in lean and burning mixtures of propane in air, taken with a delay and gate of 1 and 5 μ s respectively. The ratio of atomic lines C/(N+O) shown on the y-axis is different than that reported for the same concentration in Figure 3.2 (delay and gate 3 and 15 μ s respectively) as it depends on the detector timing. Comparison and analysis of Fig. 3.2 and Fig. 3.8 shows that the single shot measurements at the given concentrations are less resolved on the C/(N+O) axis with shorter detector

timings, reducing the sensitivity of the measurement.

- The second issue arises when directly comparing measurements obtained with different laser powers. If the pulse energy is changed, but the delay and gate are kept constant, the temporal profile of the atomic lines shifts with respect to the data acquisition window. This produces nonlinear variations in the relative intensities of the atomic lines, generating errors in the measurements.

Using a short delay and gate combination minimizes this variation for the C/N or C/(N+O) ratio, and may be useful in hydrocarbon mixtures with relatively wide concentration fluctuations, where the absorbed energy may vary and measurements of absorbed energy may not be possible. As discussed, another approach is to use energy-dependent calibrations and measurements of the absorbed energy. In general delay, gate and laser power have to be optimized for each application.

3.3.4 Quenching of atomic emission via radiationless transitions

The measured lifetime of the atomic lines of N and O varies as a function of the concentration of propane. Figure 3.9 shows the lifetime of the 745 nm N line in two different mixtures of propane and air (pure air and 0.1 mole fraction of propane), with each data point representing the average of 10 laser shots, collected with a gate width of 1 μ s at the delay shown on the x-axis. The atomic lines appear weaker and decay more quickly in a rich mixture of propane. The observed decay cannot be explained, on the basis of Equation 2.29, by a reduced concentration of N atoms

in the plasma volume. Rather, the decay is similar to the quenching of atomic emission due to radiationless decay observed in other emission techniques such as Laser Induced Fluorescence [54].

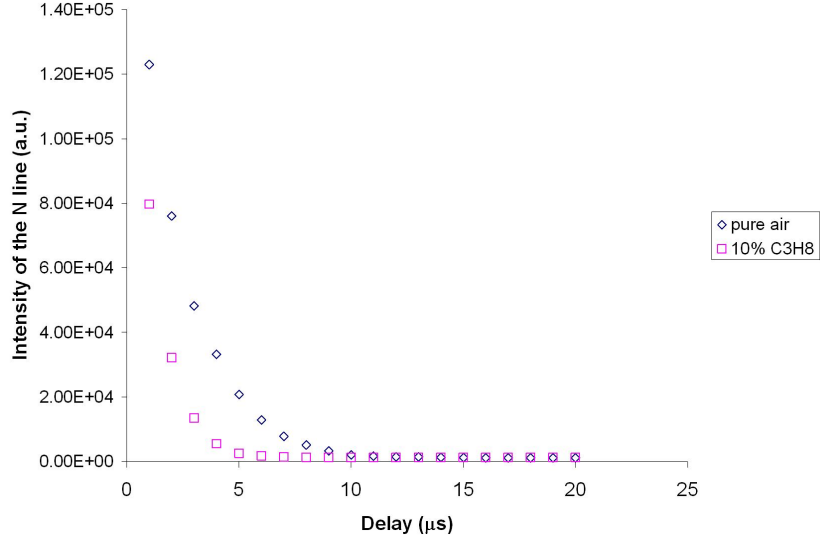


Figure 3.9: *Effect of the concentration of propane on the lifetime of the N atomic emission.*

The quantum level E_i of an atom can be depopulated not only by spontaneous emission, but also by collision-induced radiationless transition [54]. In this case the energy is transferred to another atom (or molecule) upon collision without the emission of a photon. The probability of collisional quenching depends on the concentration of collision partners, the collisional cross section, and the mean velocity of the molecules. Following the approach of Section 2.6.1 the collision probability can be written as:

$$\frac{dP_{ik}^{coll}}{dt} = \bar{v} N_b \sigma_{ik}^{coll} \quad (3.2)$$

where N_b is the number of collision partners per unit volume (m^{-3}), b , \bar{v} the mean molecular velocity and σ_{ik}^{coll} the collisional cross section. In presence of collisional quenching the total number of transitions per second, from the upper state i becomes (see equation 2.28):

$$\frac{dn_i}{dt} = n \left(\frac{g_i}{Z(T)} e^{-E_i/kT} A_{ik} W_q + \bar{v} N_b \sigma_{ik}^{coll} \right). \quad (3.3)$$

Comparing equation 2.28 and 3.3 appears that, in the presence of collisional quenching, the intensity of the emission line (given by Equation 2.29) at any time, and the atomic lifetime decreases. As discussed in section 2.6.2, since $T = T(t)$, $\bar{v} = \overline{v(t)}$ and possibly $N_b = N_b(t)$, Equation 3.3 cannot be used to obtain quantitative estimates of the emission lifetime.

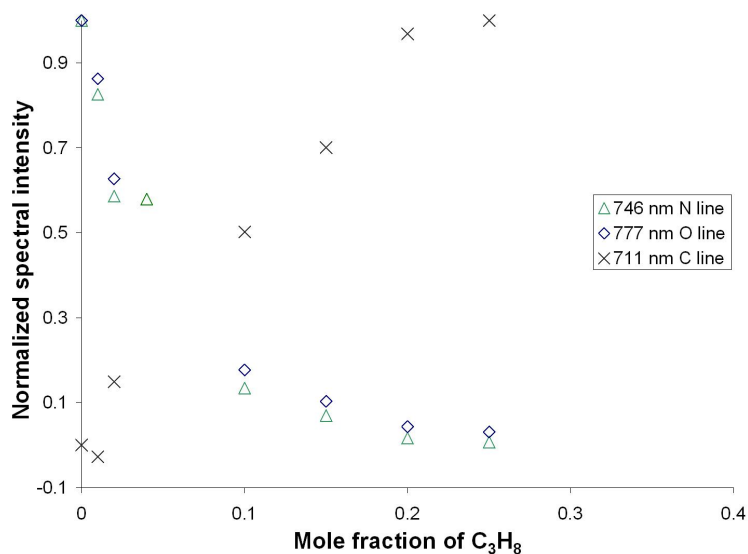


Figure 3.10: Normalized intensity of the N (746 nm) O (777 nm) and C (711 nm) lines as a function of the concentration of propane, with delay of 3 s and gate of 15 μ s.

Figure 3.10 illustrates the normalized intensity of the 711 nm C, 745 nm N and 777 nm O atomic lines as a function of the concentration of propane in air. Data were taken with a delay of 3 μs and a gate of 15 μs , each data point corresponds to the average of 300 shots. The carbon signal appears to saturate at higher concentrations of propane, while the behavior of the N and O lines is highly nonlinear. When the mole fraction of propane exceeds 0.3 the atomic emission of N and O are completely quenched at the given detector timings, and a shorter delay is required to detect a signal from N or O.

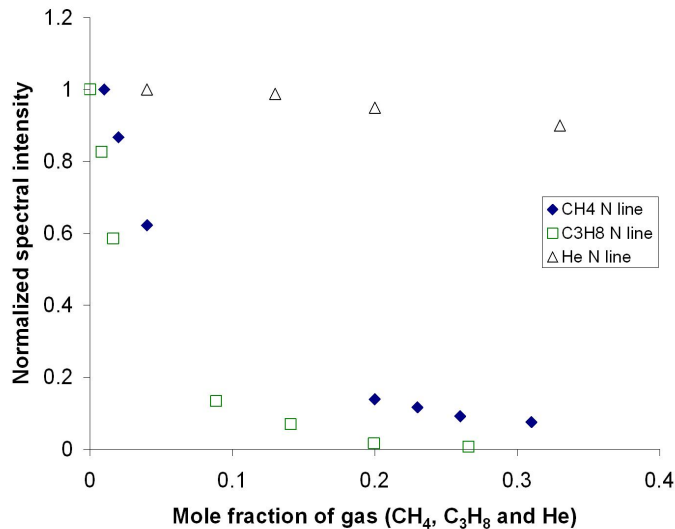


Figure 3.11: *Normalized intensity of the N (746 nm) line as a function of the concentration of propane. Comparison between methane, propane and helium, with delay of 3 μs and gate of 15 μs .*

Figure 3.11 compares the intensity of the 745 nm N line at 3 μs delay and 15 μs gate as function of the mole fraction of diluent for binary mixtures of propane, methane and helium in air. While the behavior remains linear for increasing mole

fraction of He, similar quenching is observed for propane and methane, with increasing decay associated with C_3H_8 , which has more carbon atoms and a higher C/H ratio than methane. The experimental data suggests that C, or a recombination molecule of carbon, act as collisional partner for N and O.

Applications of LIBS in combustion systems would likely require the measurements in mixed hydrocarbons and/or mixtures of reactants and products. While the measurements presented in Figures 3.9 and 3.10 suggest that C plays a major role in the behavior of the atomic emission, hydrogen also has an effect on the LIBS signal. Comparisons with CH_4 and CO_2 diluents in air are useful, as both molecules have the same number of carbon atoms so the substitution of CH_4 for CO_2 represents significant hydrogen addition, and O_2 is in high concentration in both cases, although the concentration of O_2 is not the same in the two mixtures.

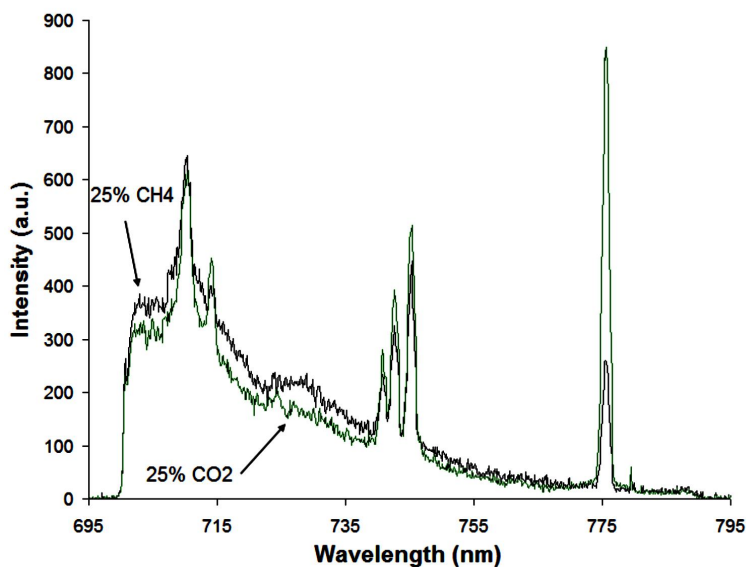


Figure 3.12: *Comparison of the emission spectra of methane and carbon dioxide.*

Figure 3.12 compares two spectra acquired with delay and gate of 3 and 15 μs ,

obtained in binary mixture of 25% carbon dioxide or methane in air. The molecular emission of CN is considerably higher in the spectra obtained with methane, while the N emission is lower. Further experiments have shown that the addition of even relatively small quantities of H₂ (1-2 % by volume) to a mixture of carbon dioxide and air increases the CN emission perceptibly. However, such increase is small enough that the effect water vapor in ambient air can be neglected in most applications. A possible explanation is that the presence of hydrogen changes the relative concentrations of the molecules that recombine in the cooling plasma; this would also change concentrations of the emitting and quenching species, thereby also changing the intensity of the N lines.

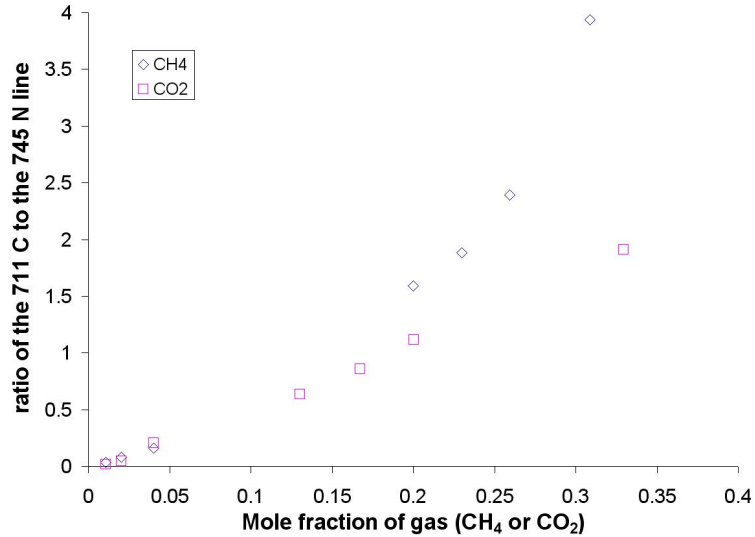


Figure 3.13: *Ratio of the C to N lines as a function of the mole fraction of methane and carbon dioxide in air, taken with a delay of 3 μ s and gate of 15 μ s.*

Figure 3.13 illustrates the ratio of the C to N line as function of mole fraction in mixtures of methane and carbon dioxide in air, taken with a delay and gate of 3

and $15 \mu s$. Each data point is the average of 300 laser shots. For methane this ratio is nonlinear, while the relationship remains linear over a wide range of mole fraction for carbon dioxide. Propane is similar to methane, but cannot readily be compared on Figure 3.13 since the total concentration of carbon atoms is different. These experiments show that chemical composition, and in particular the abundance of C and H, plays a major role in LIBS emission of mixtures of air and hydrocarbons. Although more research is required on this topic, it is expected that hydrocarbons with similar chemistry would share similar behavior.

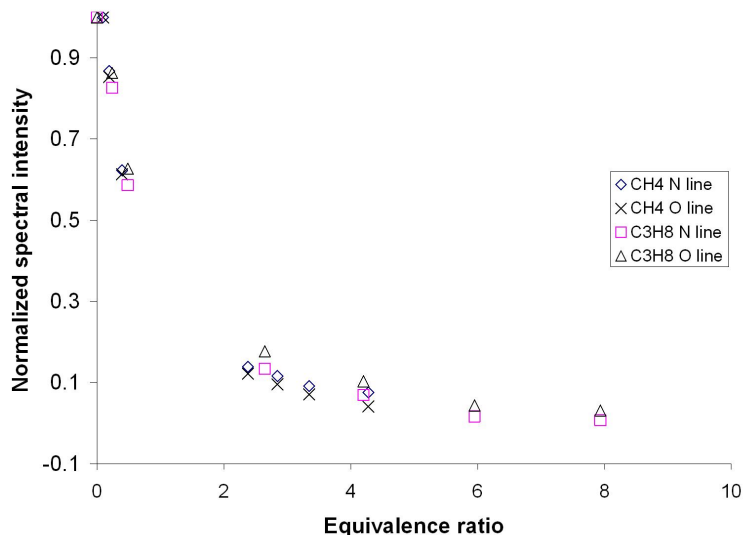


Figure 3.14: *Normalized intensity of the N and O spectral lines plotted as a function of the equivalence ratio for methane and propane.*

Figure 3.14 shows the intensity of the 745 nm N and 777 nm O lines of propane and methane plotted as a function of the equivalence ratio. The plot is similar to that presented in Figure 3.11, but the data collapse onto a single curve when plotted as a function of the equivalence ratio, illustrating the similarities as function

of atomic composition. A detailed model of the molecular quenching (that includes the transient effects arising during the plasma decay) could possibly explain the observations and be used to further generalize the results outlined in this Chapter.

3.4 Conclusions

The results presented in this Chapter illustrate the use of LIBS as a diagnostic technique for combustion systems. While limitations exist, there are several combustion applications that could benefit from this new diagnostic tool. Applications under development include real time measurements on automobile engines and measurements of the mixing of air and helium in supersonic flows (with applications to fuel injection in hypersonic and supersonic flows). In the field of combustion, LIBS can be used to investigate mixing in turbulent flames or to study ignition of turbulent reacting flows (in this case the laser would be used both as an ignition source and as a diagnostic tool). Given the high signal to noise ratio of the LIBS technique and the robustness of the measurement in reactant, products and flames, measurement of mixture fraction in turbulent flames could probably be accomplished using the methods outlined in this paper.

The measurements presented have covered several issues that are important for implementation of LIBS as a combustion diagnostic:

- Practical considerations on the performance of measurements in hot, reacting flows have been addressed. The LIBS technique can be readily used in reactants, in products, and even in flames. Measurements obtained in widely

different regimes can be easily compared, highlighting a rather unique property of LIBS as a diagnostic. The role of energy deposition in the plasma for calibration under variable conditions was illustrated.

- The influence of some key experimental parameters, such as delay, gate and laser power, on the intensity of atomic emission lines was illustrated. An understanding of the effect that these parameters have on the lifetime of the atomic emission is important for optimization of the technique in a variety of operating conditions. Each application will likely require an individual optimization, due to variations in configuration, laser plasma characteristic, and gas composition.
- Finally, emission quenching has been qualitatively described as a function of the concentration of C and H. In particular the similarities between two different hydrocarbons and the role of C and H have been highlighted. A better understanding of the basic mechanisms governing the atomic emission of hydrocarbons may be exploited to further generalize the technique. For example, it appears possible to derive a common calibration valid for mixed hydrocarbons, or to gather information on the molecular structure of hydrocarbons (for example the abundance of C and H atoms) from a single LIBS spectra.

While LIBS is an established spectroscopic technique in many fields, the measurements presented are among the first applications of LIBS to combustion problems; further research is expected to yield to considerable improvements in the technique.

Chapter 4

Real Time Measurement of the Fuel-to-Air ratio

4.1 Measurements on a Reciprocating Engine

The results presented Chapter 3 show how LIBS can be used to perform quantitative measurements of hydrocarbons. Most of the nonlinear effects related to the dependence of atomic emission on the experimental conditions can be overcome with a suitable calibration. The measurements are spatially and temporally resolved and are possible in products, reactants or flames without the knowledge of other additional parameters. The spectral emission signatures from the plasma are generally bright, providing high signal to noise ratio that can possibly translate into good accuracy. Measurements can be obtained from a single pulse of the laser, avoiding time integration of the measurements. These reasons make LIBS attractive for some applications. However, in order to identify applications of actual interest, it is

necessary to demonstrate LIBS measurements in a real combustion system.

In this Chapter real-time measurements of the equivalence ratio in a reciprocating engine are presented. The experiments were performed at the Propulsion Laboratory of United States Naval Academy in Annapolis during several test sessions in 2002 and 2003.

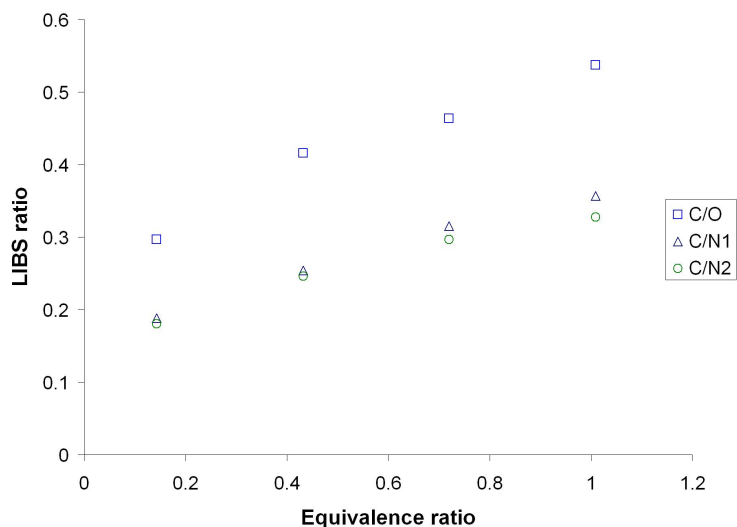


Figure 4.1: *Ratio of the intensity of the spectral lines from exhaust gas as a function of the engine equivalence ratio. N1 and N2 are the two most intense lines of the 745 nm N triplet.*

Figure 4.1 shows LIBS measurements of car engine exhaust. Cold exhaust gas was sampled from the tailpipe of an engine, while the engine was run at different equivalence ratios under a constant load. The composition of the exhaust gas was controlled with feedback from a Universal Exhaust Gas Oxygen (UEGO) analyzer. A few hundred spectra were collected for each setting of the engine and the average signal was used to produce the plot presented in Figure 4.1. In the range of equiv-

alence ratios normally achieved by a car engine , $\Phi = 0.8 - 1.2$, there is almost a linear relationship between the ratio of spectral lines and the measured fuel-to-air ratio. It was this first experiment that demonstrated the possibility to use LIBS to measure combustible mixtures [62]. In this Chapter the most relevant results from the engine tests are presented.

4.2 Engine Setup

In order to demonstrate LIBS measurement in conditions similar to those that might be encountered in applications of actual interest, an experiment is arranged to analyze hot engine exhaust in real time. The experimental apparatus is described in more detail in the Appendix. Briefly, an eddy current dynamometer loads a GM four cylinder engine. A computerized test system controls the injectors of the engine and measures the performances including speed torque and intake air flow. An optical cell is mounted on the exhaust manifold close to the exhaust valve of one cylinder. The optical cell consists of two thick fused silica window mounted at right angles on a steel frame. This design provides optical access to the exhaust gas coming from one of the cylinders at a position where gas temperature and velocity are comparable to those obtained inside a cylinder. An Nd:YAG laser is used to generate the plasma inside the cell. Atomic emission is collected at right angles and coupled into an optical fiber. The fiber sends the light to a spectrometer which disperses the light onto an ICCD camera that records the spectrum. A UEGO analyzer is placed in the optical cell to measure the fuel-to-air ratio near plasma location. The

equivalence ratio of the engine is varied by changing the injector timing. The laser is synchronized with the engine to always fire at the same position during the cycle.

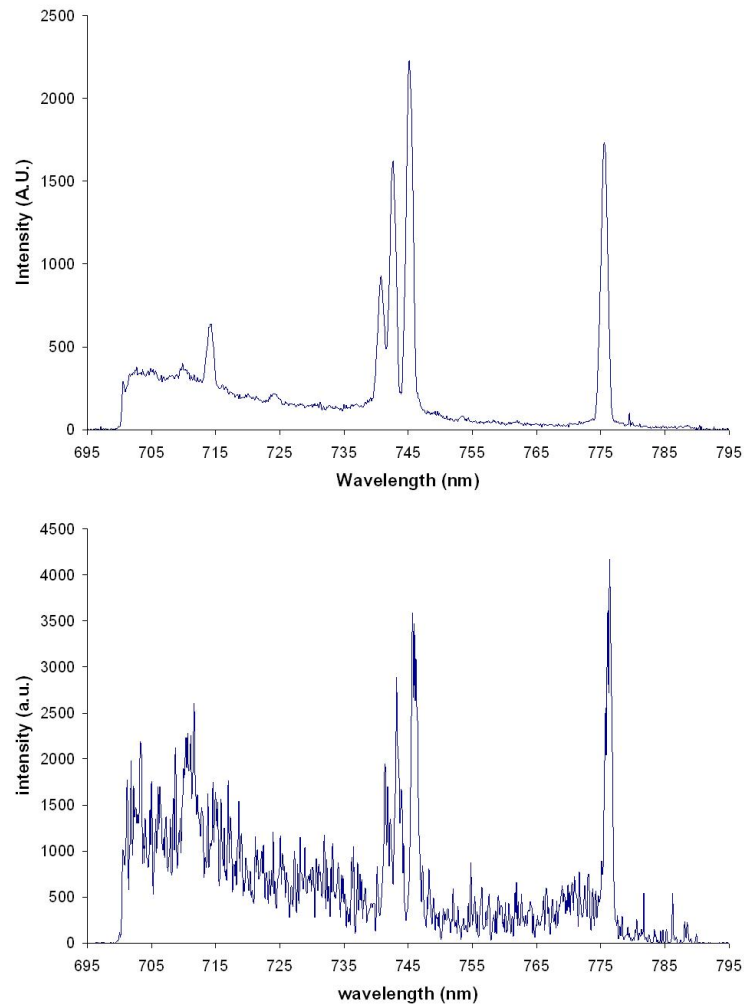


Figure 4.2: *Comparison of the single shot spectra obtained in a laboratory set up (above) and from the engine (below).*

Figure 4.2 compares the spectrum obtained in a laboratory set up (from the experiments presented in Chapter 3) with the signal obtained from the engine. Both spectra were obtained from a single pulse of the laser in different mixtures of air and hydrocarbons. In both cases, camera delay and gate are $3 \mu\text{s}$ and $15 \mu\text{s}$ respectively.

The different values on the y-axis are due to different settings of the camera intensifier. Clearly, the signal to noise ratio is considerably reduced in the measurements obtained from the engine. Nonetheless, the spectral lines of nitrogen, oxygen and carbon are clearly visible and can be used to determine the equivalence ratio.

4.3 Real Time Exhaust Gas Measurements

Figure 4.2 suggests that detection of spectral lines is not compromised by the high temperatures and the high velocity, unsteady flow field in the exhaust manifold. This conforms with expectations, since the plasma temperature (several thousands Kelvin, as discussed in Chapter 2) is much higher than those normally encountered in combustion applications, and the time required for the measurements ($18 \mu s$ in the present set of experiments) is negligibly short compared to the time scales of the fluid phenomena involved. Moreover it seems to be possible to obtain measurements through the thick optics required to sustain the stress caused by engine operation. In particular, once the manifold has warmed up and the water that initially condenses on the windows is evaporated, the instruments seem to perform satisfactorily for a time sufficiently long to perform the experiments.

Figure 4.3 shows the ratio of the 745 nm N and 777 nm O lines to the 711 nm carbon line plotted as function of the equivalence ratio (as measured by the reference UEGO sensor). The intensity of the atomic lines is calculated as described in Chapter 3 and each data point is obtained averaging together the signal from 80 single shot spectra. Similarly to the measurements obtained in a cold exhaust

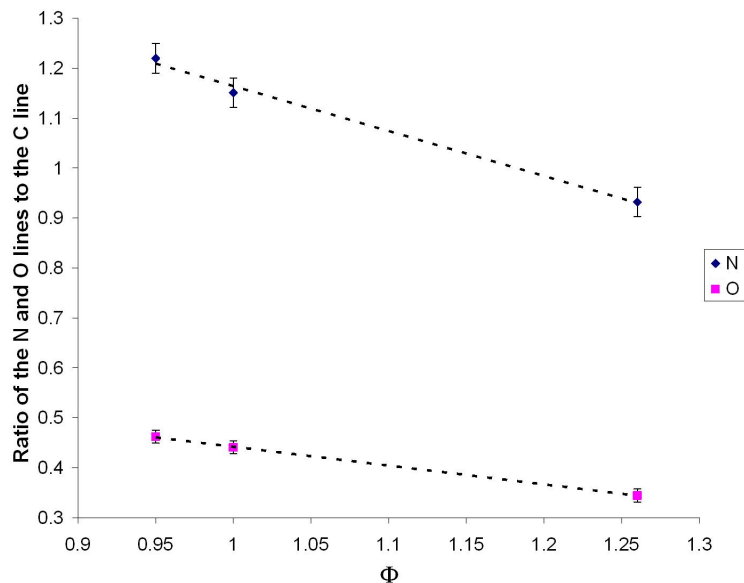


Figure 4.3: *Ratio of the 745 nm N and 777 nm O lines to the 711 nm C line as a function of the equivalence ratio.*

(and presented in Figure 4.1) there is almost a linear relation between the ratio of spectral intensities and the equivalence ratio of the mixture. Figure 4.3 represents a calibration curve to relate the LIBS signal to the equivalence ratio. As the error bars on Figure 4.3 show, averaging together multiple measurements allows discrimination between ± 0.05 changes in the equivalence ratio for averaged measurements.

Averaged measurements similar to those presented in Figure 4.3, can have some possible applications, but for engine research it is interesting to analyze single shot measurements. If single shot measurements could be similarly analyzed, the associated temporal resolution, which is only limited practically by laser repetition rate, could provide cycle-to-cycle equivalence ratio data from individual engine cylinders. Figure 4.4 compares the ratio of the 711 nm C to 745 nm N line obtained

from a single shot of the laser. The 160 data points were obtained at two different equivalence ratios: $\Phi = 0.95$ and $\Phi = 1.25$. This plot is similar to those obtained in a laboratory setup for mixtures of air and propane and shown in Figures 3.2 and 3.8. While a clear separation between the two equivalence ratios is visible in Figure 4.4, there is considerable scatter in the data, primarily related to the signal-to-noise ratio in these single-shot measurements. Likely causes can be found in the opti-

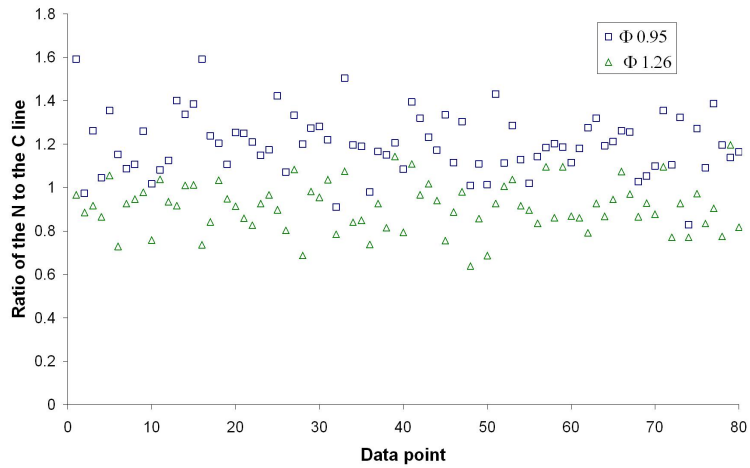


Figure 4.4: *Single shot LIBS spectrum from the engine exhaust. $\Phi = 0.95$ solid diamonds and $\Phi = 1.25$ empty squares.*

cal losses due to soot, water vapor and transmission through the optical elements. Local temperature gradients can cause variations in the refractive index of the air that affects the focusing of the laser beam. As discussed in Section 3.3.1, this could influence both the size and the position of the plasma relative to the collection optics, eventually affecting the intensity of the detected lines. Finally the non-optimal repetition rate imposed by the engine (the laser is designed to fire stably at 10 Hz) may affect the stability of the laser pulse. Shot-to-shot variation in the pulse power

would affect the plasma temperature and eventually the intensity of the atomic lines (as discussed in Chapter 2). These issues could be addressed and minimized by improvements in the experimental set up. For example it is possible to measure the relative energy of each laser pulse and relate the energy to fluctuations in the signal. Before considering modifications to the experimental apparatus, it is interesting to investigate the possibility reduce the noise by manipulating the data.

4.4 Chemometric Analysis of LIBS Spectra

There are many spectral features apparent in either of the spectra shown in Figure 4.2 that could be related to the equivalence ratio, for example the intensity of the atomic lines or suitable ratios of atomic lines. The variables used in the present Chapter and in Chapter 3 are the combinations that give the best signal to noise ratio for a particular set of measurements. An example of different variables that could be evaluated for each spectrum and related to the abundance of fuel in air is shown in Table 4.1. Among these variables, the ratio of the 711 nm C line to the 745 nm N line, used in Figures 4.3 and 4.4, gives the best results as a predictor of Φ , but it is likely that each of the 10 variables shown in Table 4.1 contains some information. Moreover the 10 variables are not independent, but are interrelated. It is expected that it is possible to find a linear combination of these variables that has the best correlation with the local equivalence ratio. Principal component analysis (PCA) was used to determine the optimum combination of these 10 variables for prediction of Φ (see for example [63] for an introduction to principal component

Table 4.1: *Combinations of several spectral features from Figure 4.2 that could be related to the equivalence ratio: C = 711 nm C line, O = 777 nm O line, NI and NII = first and second lines (in order of intensity) of the 745 nm N triplet, CN = CN molecular band.*

Variable	Definition	Variable	Definition
x_1	N I+ N II + O	x_6	C/N I
x_2	N I	x_7	C/O
x_3	O	x_8	C/(N I + O)
x_4	C	x_9	C/(N I + N II + O)
x_5	CN	x_{10}	CN/O

analysis).

A Matlab routine is used to calculate the 10 variables shown in Table 1 for each spectrum in a set of data, for example the 160 spectra shown in Figure 4.4. There are at most 10 independent (or orthogonal) linear combinations of these variables. A principal components algorithm built into Matlab, based on multivariate analysis, is used to calculate the linear combination of these variables that expresses the most variance among the data; this combination is called the first principal component. The second principal component is computed such that it is orthogonal to the first and expresses as much of the remaining variance in the data as possible, and so on. Since Φ is the only parameter that is changed during the experiments it is expected that the variance in the data is all related to Φ . Moreover, since the variables are not independent, the first few principal components should contain most of the variance

and are likely to be the best linear combinations to relate spectral features with Φ .

The output of the software is the 10-by-10 matrix \mathbf{A} that transforms the variables in Table 4.1 into the new set of principal components according to the relation:

$$y = Ax^T \quad (4.1)$$

where \mathbf{x} is the row vector containing the 10 initial variables and \mathbf{y} is a vector containing the numerical value of the principal components. It is then possible to plot the first few Principal Components and verify how they relate to Φ . The new coordinate system groups the variance in the first few variables, so that the data can be plotted and analyzed conveniently. Figure 4.5 shows the set of data from Figure

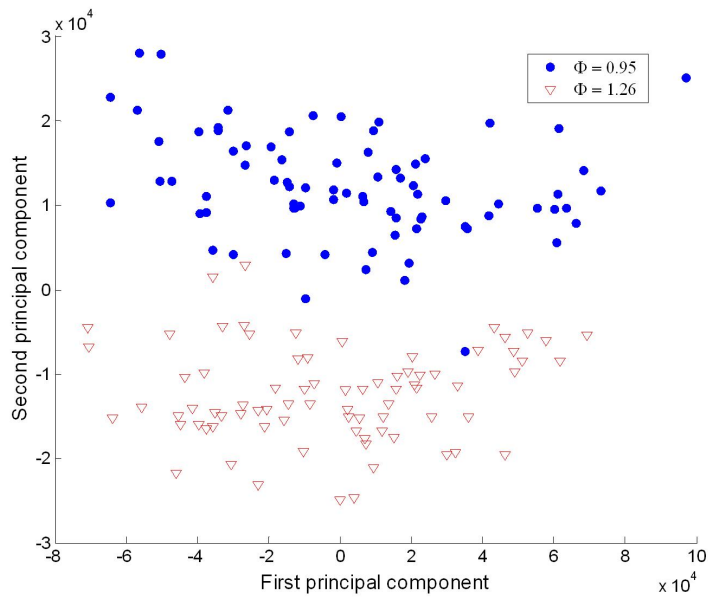


Figure 4.5: *Single shot LIBS measurements plotted in function of the Principal Components (from the same data presented in Figure 4.4).*

4.4 plotted as a function of the first two principal components. The data series

now appear more fully separated, indicating that PCA succeeded in recognizing Φ as a latent property in the data. When compared with the plot in Figure 4.4 it appears evident that PCA significantly reduces the scatter in the data, improving the determination of Φ from LIBS spectra. For example, it is possible to estimate the increased accuracy of the technique by the number of non-overlapping points in Figures 4.4 and 4.5. The number of spectra for which the equivalence ratio can be correctly resolved increases 23% using PCA, from 72% of the total in Figure 4.4, to 95% in Figure 4.5. For this set of data, the first two principal components express the 99.3% of the variance in the data. Conveniently, principal component analysis is fully automated and doesn't require post-processing of the data.

PCA was applied to another set of data acquired at a later time than the data in Figures 4.4 and 4.5. Using the same experimental parameters as in the previous experiments, the equivalence ratio was set to 0.85, 1.00 and 1.15. The first graph in Figure 4.6 illustrates the original data, and the second illustrates the data following treatment with PCA. Again, it is evident that PCA significantly improves the resolution of Φ from the original data. The data in Figure 4.6 illustrate the limits of the present experimental set up for engine measurements.

4.5 Conclusions

The results presented in this Chapter demonstrate the use of LIBS as a diagnostic technique to obtain optical measurements of the equivalence ratio in an engine. Spatially and temporally resolved measurements were obtained in the exhaust manifold

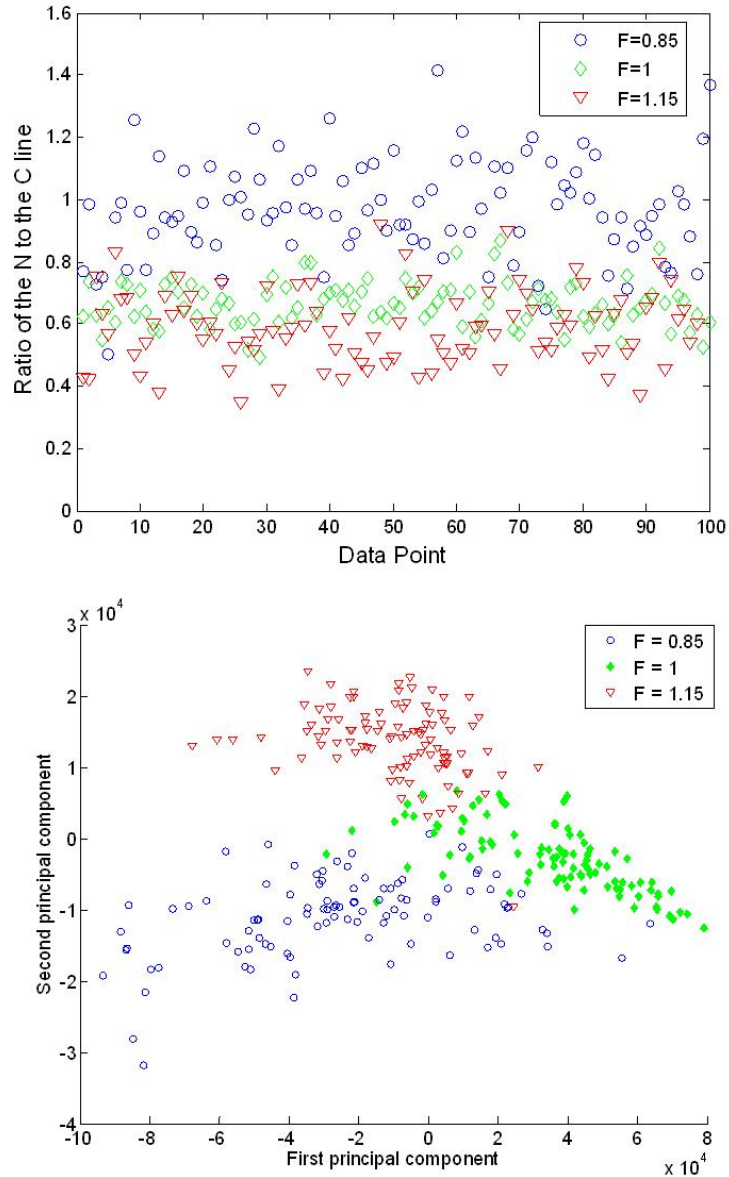


Figure 4.6: *Analysis of spectra obtained in lean ($\Phi = 0.85$), stoichiometric and rich ($\Phi = 1.15$) conditions. Comparison of the original data (above) to data treated with PCA (below).*

of an automotive engine in conditions comparable (for temperature, flow velocity, volume fraction of soot, etc.) to those that would be encountered in situations of actual interest, for example during measurements inside a cylinder or in a combus-

tor. Practical difficulties related with the experiment do not prevent quantitative measurements and it was possible to synchronize the laser with the engine to obtain measurements in a fixed position during the cycle.

The possibility of obtaining single shot measurements is discussed, since such measurements are of primary interest for possible applications. In particular the numerical techniques of principal component analysis can be used to significantly improve the accuracy of the single shot data. Using principal component analysis it was possible to discriminate between single shot measurements obtained in lean ($\Phi = 0.85$), stoichiometric ($\Phi = 1$) and rich ($\Phi = 1.15$) conditions. The implementation of principal component analysis is fully automated and becomes an integral part of the calibration procedure. As a whole, these measurements suggest LIBS measurements of hydrocarbons may become a useful diagnostic technique for practical combustion systems. The measurements presented in this Chapter demonstrate the sensitivity and accuracy that can be achieved with the current setup. Changes to the experimental apparatus will likely be necessary to further improve the technique.

Chapter 5

Future Work

5.1 An Outline for Future Research

This Chapter provides a brief description of some interesting phenomena observed during these experiments that may be worthy of future work. Here the preliminary results that could be used as the starting point of a new research are summarized. The next three sections describe the emission of extreme ultraviolet radiation from a laser-induced plasma and the effect of a spherical shock wave on nanometer-sized particles. Both topics departs from the main body of this dissertation, but might be of some interest in related fields of research.

5.2 Extreme U.V. Emission from the Laser-Induced Plasma

Recently laser plasmas have been proposed as a possible source of x-ray and extreme UV radiation [64]. A new source of high energy radiation could have applications of considerable interest in the fields of photolithography and material processing. As seen in Figure 2.22, the plasma emits radiation at high frequencies shortly after the breakdown. The total energy radiated is, however, only a small fraction of the deposited energy. Figure 5.1 shows the signal measured with a diamond photodiode for different laser pulse energies. The electric potential measured on the y axis is proportional to the plasma emission in the 200-2200 eV range [65] i.e., to radiation in the extreme UV and soft x-ray range. As expected, the emission increases

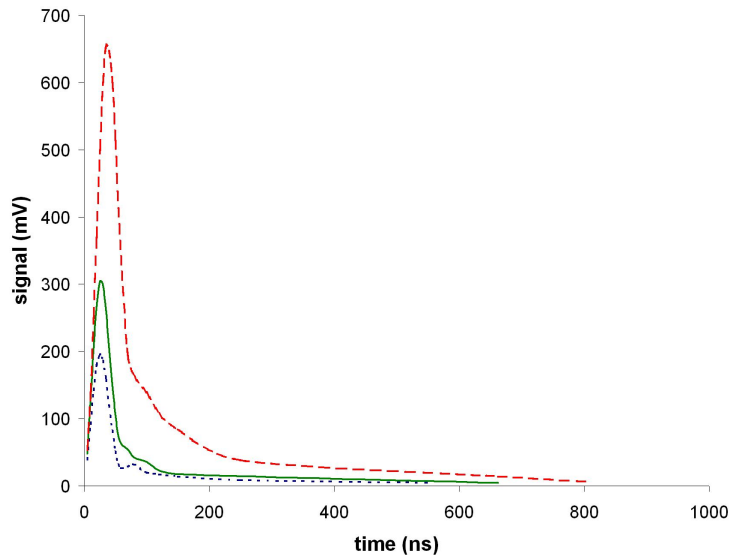


Figure 5.1: X-ray and E.U.V. plasma radiation for different pulse energies. Dotted line: 60 mJ; solid line: 100 mJ; dashed line 200 mJ.

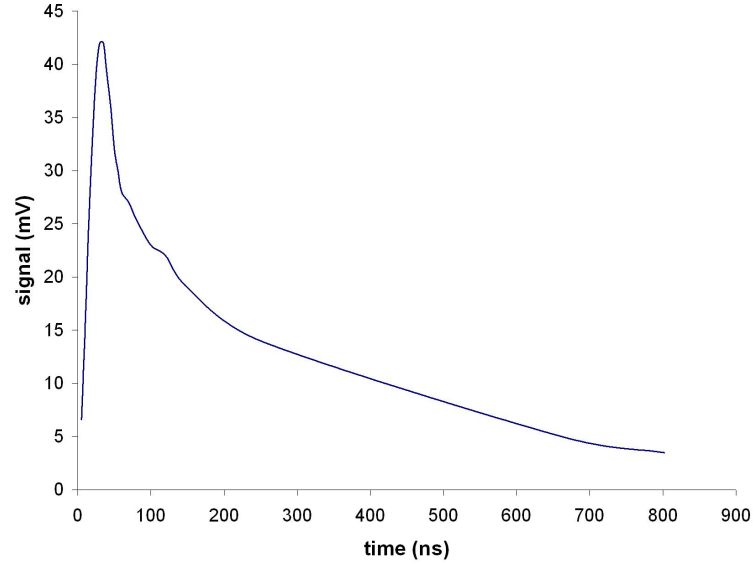


Figure 5.2: *X-ray emission from a laser plasma; laser pulse energy, 300 mJ.*

with increasing laser energy. Radiation intensity reaches a maximum few tens of nanoseconds after the breakdown and rapidly decays afterwards. Regardless of the laser pulse energy, it appears that the emission of radiation occurs in two different stages: an intense burst during the first 100 ns, and a slowly-decaying emission lasting several hundred ns. The reason for this behavior is not known, but it might be related to the structure of the laser supported wave during the very first stages of the expansion.

The exact spectrum of the radiation emitted is not known. In order to gain a qualitative understanding of the spectral distribution, a thin aluminum foil (with a thickness of few hundred μm) is placed in front of the photodiode. Only radiation with a very high frequency (with energy greater than approximately 1 keV) can pass through the foil. Figure 5.2 shows the radiation detected by the shielded photodiode for a 300 mJ laser pulse. The radiation detected is due to soft x-rays and the profile

in time appears similar to that presented in Figure 5.1. More research is needed to identify possible applications and to enhance the intensity of the emitted radiation.

5.3 Shock Wave Effect on a Dense Aerosol

During the LIBS measurements on engine exhaust, presented in Chapter 4, an unexpected phenomenon was observed. In the cold exhaust of the engine a large number of carbonaceous particles, with diameters of a few tens of nm, are formed due to homogeneous nucleation. During the experiments, the particle size distribution was measured in real time with an optical particle counter. Meanwhile, LIBS was used to measure the composition of the gas. A sudden change in particle size was noticed when the LIBS laser was operated.

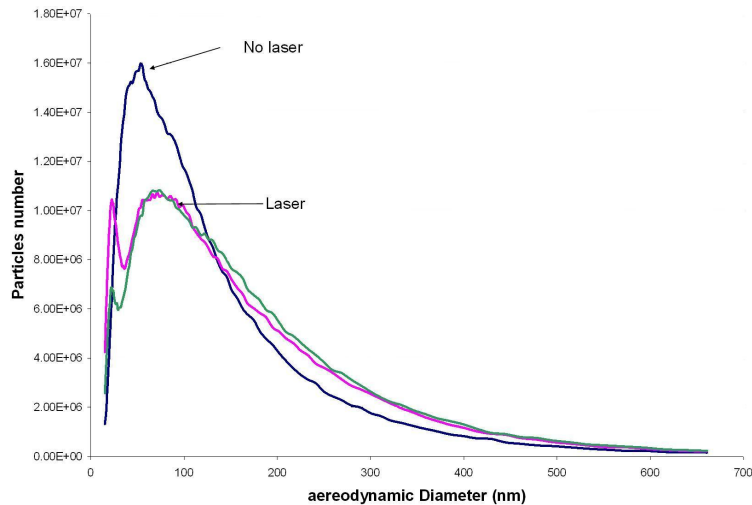


Figure 5.3: *Effect of the shock wave on the particle number distribution of a dense aerosol.*

To investigate the phenomenon the following experiment was performed. An aerosol was generated with an atomizer using solutions of sodium or magnesium. The aerosol flowed through an optical cell where the laser was focused. The cross section of the optical cell (several cm^2) was much bigger than the characteristic dimension of the plasma, thus the effect of the hot plasma on the overall temperature was negligible. The particle size distribution was analyzed using a Scanning Mobility Particles Sizer (SMPS). Figure 5.3 shows the particle size distribution of the aerosol with and without the operation of the pulsed laser. As it can be seen, the number of particles with diameter in the range between 30 and 100 nm is greatly reduced when the laser is operated. Meanwhile the number of particles with diameter greater than 150 nm is increased.

This phenomenon is attributed to the shock wave generated by the plasma discharge. The laser-generated shock wave transfers momentum to the particles. The velocity of the particles depends on the diameter; therefore particles of different sizes will acquire a relative velocity and may collide together. Upon collision, surface forces cause the particle to stick together. The overall effect is that the number of smaller particles is reduced while new larger particles are created. A similar phenomenon, well documented in literature, is the agglomeration of particles due to standing or travelling sound waves [66] [67]. Compared to the sonic case, the particle motion in weak shock waves has been studied much less. Some relevant papers on the subject are quoted in references [68], [69], [70], [72], [73], [74]. In particular Goldshtein and co-workers demonstrated experimentally the displacement of small particles and aerosol agglomeration, caused by a planar shock wave [68], [69].

In Figure 5.3 it is also observed that a peak of particles with diameter around 25 nm appears when the laser is operated. This peak is likely caused by re-suspension of particles from the walls of the optical cell. The smaller particles, with a relatively large diffusion coefficient, deposit on the walls of the cell by diffusion. When the laser is operated, the vibrations induced by the shock wave re-suspend the particles, increasing the number of small particles. Using this mechanism, Vanderwood and co-workers proposed the use of shock waves to clean silicon surfaces of nanoparticles, [75], [76].

5.3.1 Drag of a nanometer-sized particle in a spherical shock wave

To understand the dynamic effect of the shock wave on an aerosol, it is necessary to describe the behavior of a single particle in the flow field caused by the laser spark. The results presented in Chapter 2 show how fluid velocity in time can be determined accurately from the results published in literature. The trajectory of a particle through the shock wave can be determined once the particle's drag is known. The simpler model to describe the motion of a solid particle is to assume an uniform, spherical particle in a Stokes flow. With these assumptions the acceleration on a particle is given by Stokes law:

$$\frac{dv}{dt} = \frac{18\mu}{\rho_p d^2} (u - v) \quad (5.1)$$

where v is the velocity of the particle, u the velocity of the fluid, μ the viscosity of the fluid, ρ_p the particle density and d the particle diameter. Stokes equation is

valid only in the assumption of viscous flow. That is with $Re_r < 1$ where Re_r is the relative Reynolds number based on the relative particle velocity, $u - v$ and the particle diameter, d :

$$Re_r = \frac{\rho_0 d |u - v|}{\mu_0} \quad (5.2)$$

If the particle diameter becomes comparable with mean free path of the fluid molecules, the gas cannot be assumed to be a fluid with continuum properties. In particular, the fluid velocity with respect to the particle cannot be assumed to vanish at the particle surface. The Knudsen number, Kn , is defined as:

$$Kn = \frac{\lambda}{d} \quad (5.3)$$

where λ is the mean free path of the molecules. For values of the Knudsen number greater than 10^{-3} rarefaction effects become important [77]. A common correction for the particle acceleration is to consider:

$$\frac{dv}{dt} = \frac{18\mu}{C\rho_p d^2} (u - v) \quad (5.4)$$

where C is the Cunningham correction factor defined as:

$$C = 1 + Kn(1.257 + 0.4e^{-1.1/Kn}) \quad (5.5)$$

For higher values of the relative Reynolds number, the inertia of the particle becomes important while, for high values of the relative mach number, M_r (defined as the ratio of the relative particle velocity, $u-v$, to the speed of sound), compressibility effects become important [77]. Equation 5.4 is usually assumed to be valid for $Re_r < 1$ and $M_r < 0.6$ and can easily be integrated to obtain the particle trajectory.

5.3.2 Particle trajectory in a spherical shock wave

Equation 5.4 approximately describes the behavior of a solid particle of a few hundred nanometers in diameter, in a viscous flow. The trajectory through a shock wave can be found considering a particle initially at rest at a short distance from the breakdown. Assuming spherical symmetry, the flow field as a function of time and space is determined interpolating the tables given in [31] and [47] (considering also the results discussed in Section 2.4.3 to obtain the correct flow field for a given laser pulse energy). Then, Equation 5.4 is integrated twice to compute the particle trajectory in the radial direction. A computer code was written in *Matlab*[®] to perform these tasks.

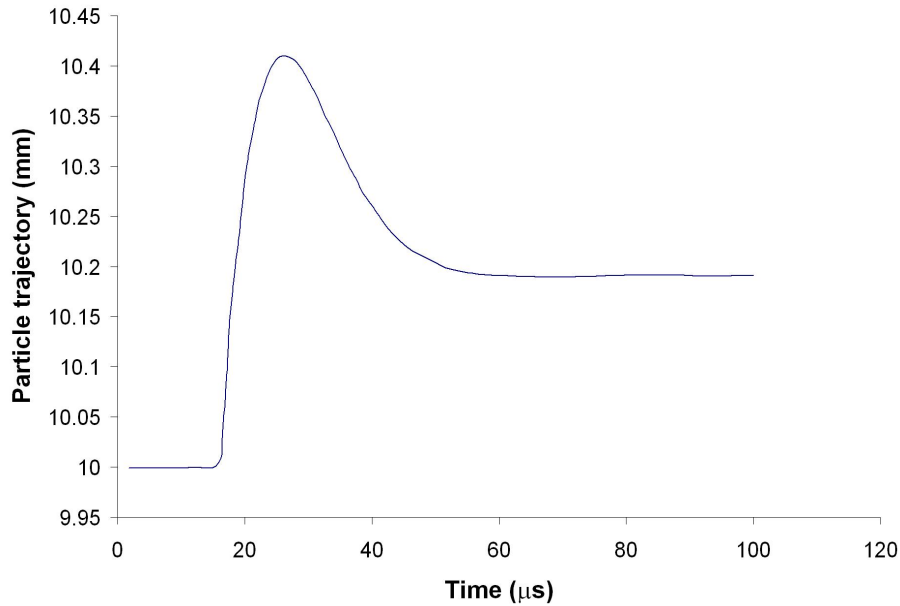


Figure 5.4: *Displacement of a 100 nm particle (with density 1000 kg/m³) initially placed at 10 mm from the breakdown point of a 300 mJ laser pulse.*

Figure 5.4 shows the radial displacement, $r = r(t)$, of a 100 nm particle with

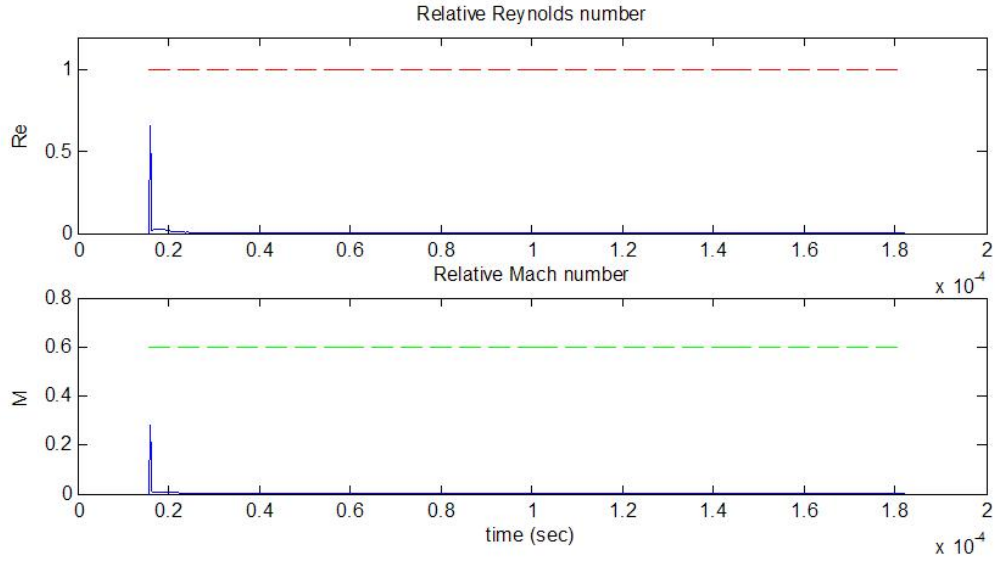


Figure 5.5: *Relative Reynolds and Mach numbers for a 100 nm particle as a function of time. The dotted lines show the limit of validity of Equation 5.4.*

density of 1000 kg/m^3 , initially placed at 10 mm from the breakdown point of a 300 mJ laser pulse. This set of initial conditions could represent a solid particle suspended in air. First, the particle is pushed outwards by the expanding blast wave, then it is moved back towards the center by the back-flow in the expansion wave. The displacements caused by the shock wave are on the order of thousands of particle diameters. The simulations suggest that, after the shock wave has passed, there is a net positive displacement of the particles, that is, the particles are pushed away from the breakdown point. However, the net displacement is small when compared to the size of the turbulent region generated during the last stages of the breakdown (see section 2.5). For this reason, the shock wave is not expected to have an influence on the local concentration of an aerosol, but could have an effect on particle collision rates.

The results of the simulations are consistent with the structure of the shock

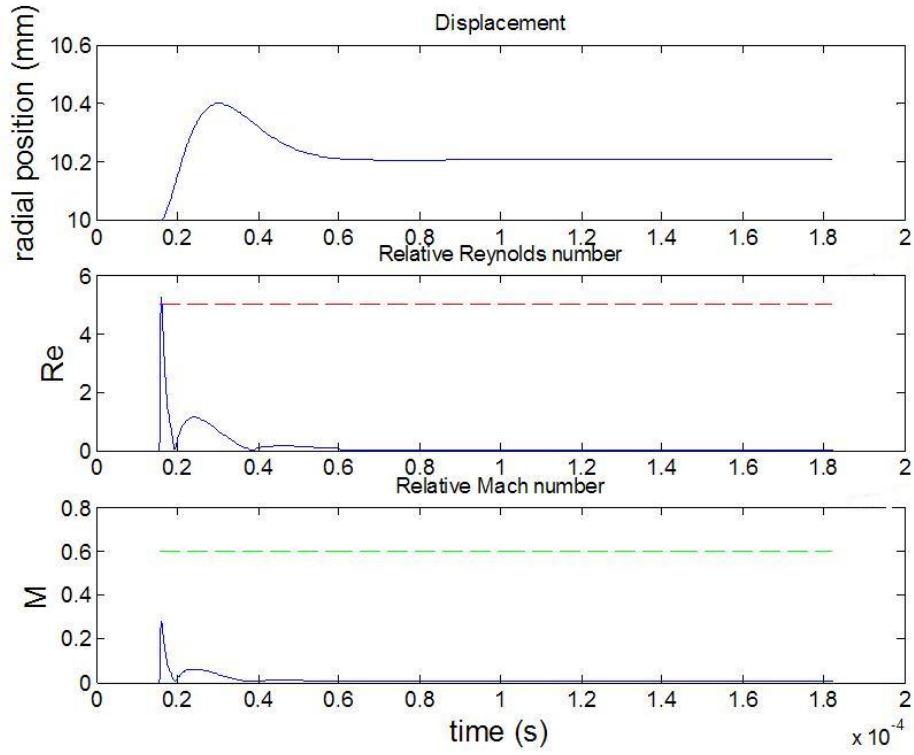


Figure 5.6: *Displacement, relative Reynolds and Mach numbers for an 800 nm particle as a function of time.*

wave, but have not been verified experimentally. Figure 5.5 shows the relative Reynolds and Mach numbers for the particle in Figure 5.4 through the shock wave, as a function of time: it appears that the values remain within the range of validity of Equation 5.4. If this results could be validated experimentally (for example using Particle Image Velocimetry) it would be possible to use the simulations to compute the relative velocity of particles with different sizes. Figure 5.6 shows the displacement and the relative Reynolds and Mach numbers for a 800 nm particle (in the same conditions as those described for Figures 5.4 and 5.5).

5.3.3 Implications for Aerosol Measurements

If the relative velocity of particles is known, then a kinetic model for the collision of particles, similar to that presented in [78], can be developed to describe the agglomeration of an aerosol. Consider a polydisperse aerosol, initially composed of a number N_0 of particles divided in k groups according to the diameter. Let n_i be the number of particles with diameter d_i , and v_i their velocity. In the time Δt , a single particle d_i will travel a distance $\Delta t v_i$. Assuming that the particles with diameter d_j have lower velocity, d_i will collide with all the particles d_j that happen to be in a cylinder with base $\frac{\pi(d_i+d_j)^2}{4}$ and height $\Delta t(v_i - v_j)$. The number of collisions for the single particle d_i with particles d_j is:

$$c_j = \int_V \int_0^\infty \frac{\pi(d_i + d_j)^2}{4} (v_i - v_j) n_j dt dV \quad (5.6)$$

where V is the volume of the aerosol. For n_i particles d_i the total number of collision is:

$$c_{ij} = n_i \int_V \int_0^\infty \frac{\pi(d_i + d_j)^2}{4} (v_i - v_j) n_j dt dV \quad (5.7)$$

Assuming perfectly sticking particles (although this is just an approximation), then when two particles with diameters d_i and d_j collide together they form a particle with diameter $(d_i + d_j) = d_{i+j}$. It is then possible to model the evolution of the particle population. The rate of formation of particles with diameter d_q will be:

$$n'_q = \frac{1}{2} \sum_{i+j=q} c_{ij} \quad (5.8)$$

where the summation $i + j = q$ is intended over those particle that would yield a particle d_q upon collision. The coefficient $1/2$ is inserted not to count each collision

twice. Any collision of a particle d_q decreases n_q . Therefore the rate of change of particles d_q is:

$$n'_q = \frac{1}{2} \sum_{i+j=q} c_{ij} - \sum_{i=1}^k c_{iq} \quad (5.9)$$

Knowing the relative velocity of different particles as a function of space and time, allows to solve Equation 5.7 calculating the number of collisions. Then, the particle population evolution is completely determined. It is noticed that the agglomeration of an aerosol can be investigated experimentally with experiments similar to that presented in Figure 5.3. Therefore, a model for particle dynamics could provide insight on quantities that are hard to measure such as drag of nanometer-sized particles or the probability of particles to stick together upon collision.

Chapter 6

Conclusions

6.1 Summary of the Present Work

In this dissertation, possible new applications of Laser Induced Breakdown Spectroscopy are investigated. The work is divided into two distinct parts. In the first, an experimental and theoretical study of the basic physics governing the laser-induced breakdown is carried out. In the second part, atomic emission lines from the plasma are used to perform gas composition measurements. In order to obtain reliable spectroscopic measurements, a detailed knowledge of the laser-induced plasma is needed. Thus, the two parts of the research are deeply connected.

6.2 Experimental Study of Laser Plasmas

Laser plasmas are formed when the energy from relatively powerful laser pulses (typically a few hundreds of mJ in a ~ 10 ns pulse) is absorbed by ionized gas. Af-

ter the initial breakdown, the plasma can be described as an inviscid, compressible fluid. The laser energy is absorbed by a layer of ionized gas that is compressed by a strong shock wave, to reach high temperatures and high densities. The absorbed energy creates the shock. The mechanism is similar to ordinary detonations, where a shock wave ignites an explosive releasing chemical energy. In order to understand the plasma evolution, it is necessary to investigate the fate of the energy deposited in the fluid. Experimental measurements suggest that only a small fraction of the energy is dissipated in the form of radiation. The greatest part of the energy is spent to increase the internal energy of the fluid, which rapidly expands. Dimensional analysis of the problem allows the derivation of scaling laws that determine the dimensions of the plasma, at the end of the 10 ns laser pulse, as a function of laser pulse energy. The volume of the plasma defines the region where a known amount of energy is stored. Thus, it is possible, using thermodynamic relations between internal energy and temperature, to estimate the plasma temperature. The theoretical estimates are found to be in good agreement with the values measured experimentally.

After the end of the laser pulse, the free expansion of the fluid can be described using the theory of point explosions. Originally developed to study nuclear explosions, the theory of point explosions describes the shock wave produced by the laser breakdown (where the energy release is tens of orders of magnitude smaller). The position of the shock wave in time is measured experimentally and compared to the theory. This allows to accurately determine the evolution of the flow field during the first few tens of μs , as well as the final energy distribution. Most of the energy is

irreversibly converted into heat and remains deposited within few tens of mm from the breakdown point. The small region of hot gas rapidly develops instabilities and turbulent convection dissipates the remaining energy.

The plasma emits intense radiation for few hundred nanoseconds following the breakdown. The continuum bremsstrahlung radiation from the plasma rapidly fades as the fluid expands. After less than a μs after the laser pulse, atomic emission lines emerge from the background. The emission lasts a few tens of μs , during which the shock wave detaches from the central, hot gas region, and fades well before the onset of instability (for the laser pulse energies investigated in this study). The lifetime of the atomic emission is determined by the overlap of two phenomena: the spontaneous decay of fluorescence and the hydrodynamic evolution of the gas.

The model of shock propagation developed is in good agreement with the experimental observations, and allows for quantitative estimates of the fluid properties. The approximate relations derived in this dissertation could be considerably improved by means of numerical simulations. For example, computer models should be capable of describing the plasma from the absorption of the laser pulse, to the final emission spectra. Nevertheless, the approach used in this dissertation describes a convenient non-dimensional formulation of the problem. These experimental results, when reported in non-dimensional form, could be used to validate numerical results.

6.3 Measurements of Hydrocarbons

In the second part of the research, spectroscopic emission is used to measure the composition of mixtures of air and hydrocarbons. The 700 – 800 nm spectral region contains atomic emission of C, N and O, allowing the estimation of the mole fraction of fuel and oxidizer. LIBS measurements can be carried out in reactants, products and even flames. Nonlinear effects, due to the high temperature gradients present in the flame, can be corrected during calibration. There is a monotonic relation between intensity of the spectral lines and mole fraction of fuel in a gas over a wide range of concentrations. Measurements can be obtained with a single pulse of the laser and are spatially and temporally resolved.

In order to optimize the technique, the dependence of the measurements on the main experimental parameters is studied. In particular, the effect of laser pulse energy and detector timing are investigated. The energy of the laser pulse determines the volume and temperature of the plasma. This influences both the intensity and the lifetime of atomic emission. The timing of the camera determines the temporal interval over which spectroscopic emission are integrated to generate the signal. The camera timing can be optimized to obtain the best signal to noise ratio for a particular experiment.

It is noticed experimentally that high concentrations of C decrease the intensity and lifetime of the N and O atomic emission lines drastically. This phenomenon cannot be explained by the reduced concentration of N and O atoms in the plasma volume. The reduced atomic emission lifetime is consistent with a collisional quench-

ing model, where the excited quantum levels are depopulated by collisions with other atoms. Likely C, or a recombination molecule containing C (for example CN, formed in the cooling plasma), acts as an effective collision partner for N and O atoms. Experimental measurements suggest that emission spectra is also affected by the concentration of H. The behavior observed appears to be similar for different hydrocarbons. The experimental calibration of the technique will thus depend on the chemical composition of the hydrocarbon investigated. Further research is needed to better understand the role of the chemical matrix on emission spectra.

In order to identify possible applications of the technique, LIBS is used to analyze exhaust gas from a reciprocating engine. It is demonstrated there is a linear correlation between the intensity of spectroscopic emission and the fuel to air ratio. The measurements are performed in the hot exhaust gas, few centimeters from the exhaust valve of one cylinder. The conditions of temperature and fluid velocity are comparable to those encountered in the combustion chamber of an engine. Compared to the measurements obtained in a laboratory set up, the signal-to-noise ratio in the engine measurements is considerably reduced. It is demonstrated that the statistical technique of principal component analysis can be used effectively to increase the sensitivity of the measurements. It was then possible to discriminate between measurements obtained in lean ($\Phi = 0.85$), stoichiometric, and rich conditions ($\Phi = 1.15$). These measurements define the limits of sensitivity that can be achieved with LIBS, in the present configuration.

Appendix A

Experimental Setup

A.1 Measurement of the Radiated Energy

As shown in Figure [A.1](#), the plasma is generated by Nd:YAG, Spectra Physics Pro 250 laser, Q-switched with 10 Hz repetition rate. The pulse duration is 10 ns FWHM. The pulse energy is accurately controlled using an optical attenuator consisting of 1/2 retardation waveplate and a polarizing cubic beam splitter. The energy of the beam is measured using an Ophir PB50BB pyroelectric energy meter. The laser is focused by a 75 mm focal length fused silica lens and the radiated energy is measured with an Ophir 10A-P volume absorber energy meter. The radiation detector has a flat response in the range between 190 and 1500 nm and is initially positioned at 19 mm from the focus of the lens. The position is accurately controlled with a micrometric translation stage. Since the volume absorber detector is sensitive to the vibrations produced by the shock wave, it is protected with a fused silica window. All the measurements are corrected for losses through the optical components.

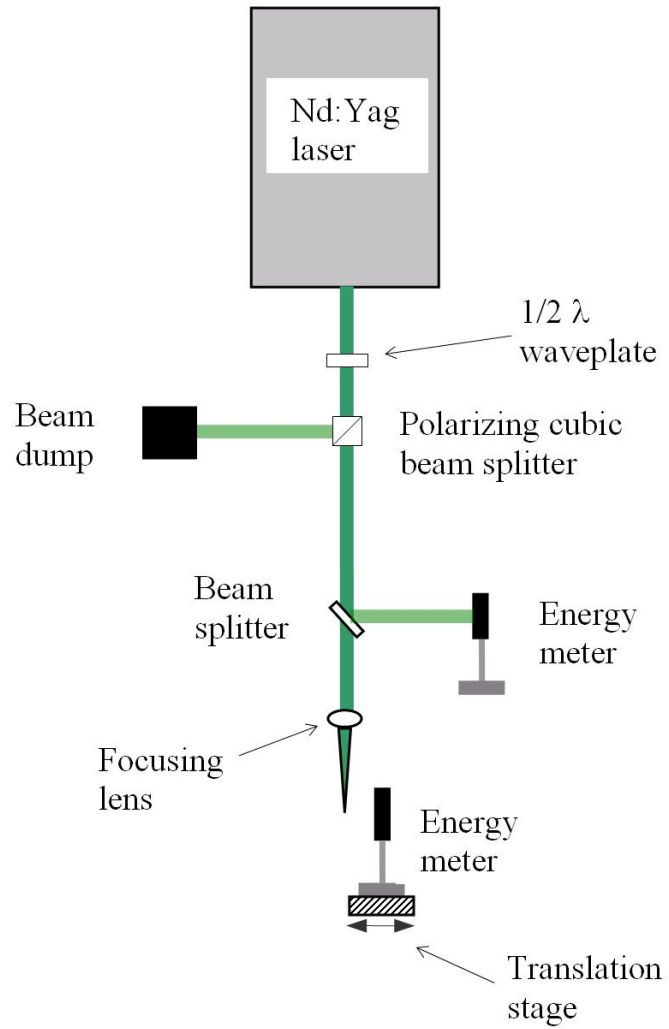


Figure A.1: *Measurement of the radiated energy: experimental setup.*

A.2 Shadowgraphy Setup

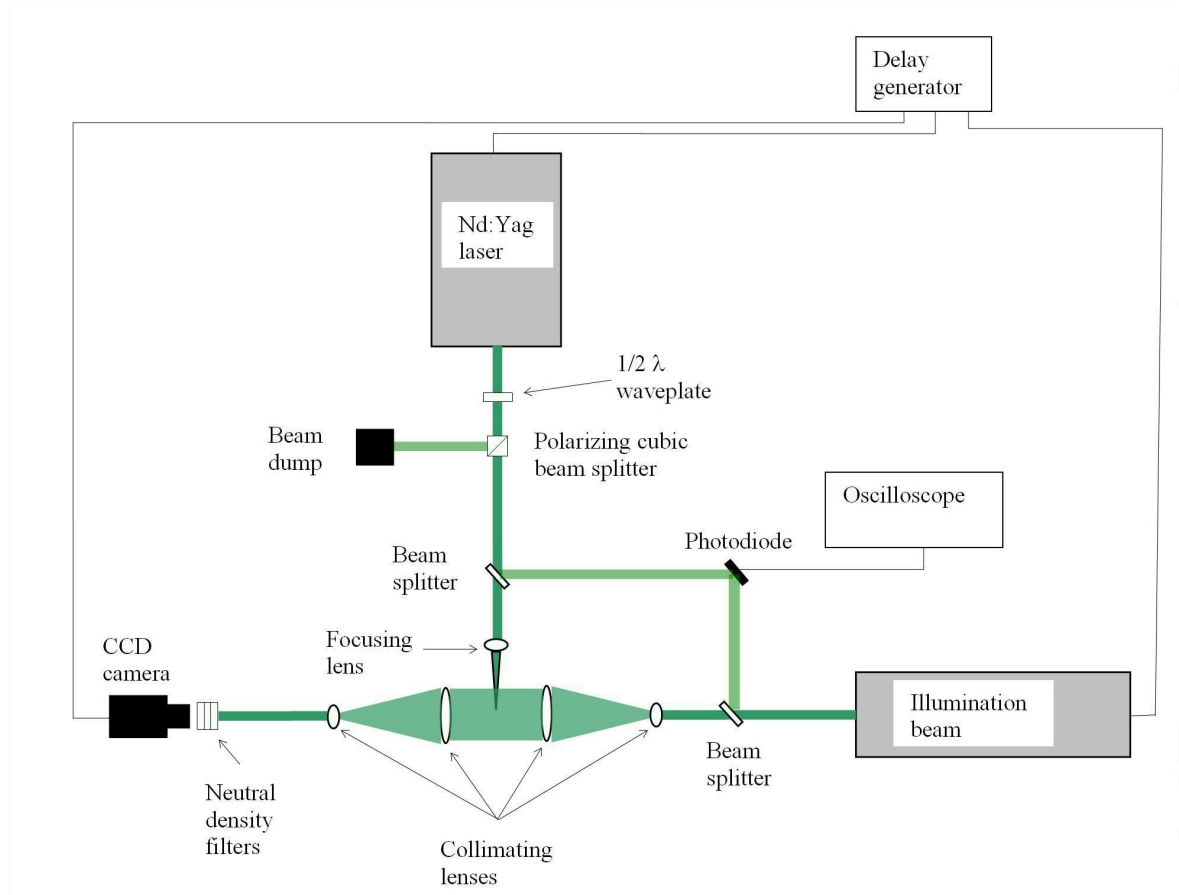


Figure A.2: *Setup for shadowgraphy.*

Illustrated in Figure A.2, a Nd:YAG lab 150 Spectra Physics laser, with a 10 ns FWHM pulse width, is used to illuminate the plasma at right angles. The laser beam is expanded to a diameter of 50 mm by a matching pair of collimating lenses and subsequently imaged on a SONY XCD-SX900, CCD camera. The beam intensity is attenuated using a set of neutral density filters. The lasers and the camera are synchronized using a Berkeley Nucleonics Delay Generator. On a pulse-to-pulse basis, the timing between the two lasers is assumed accurate within ± 10

ns. Over a longer period of time the delay between the two lasers may drift a few hundred of ns. To reduce this uncertainty to few tens of ns, the delay between the laser pulses is checked periodically with a 100 ps rise-time photodiode connected to a fast oscilloscope.

A.3 Spectroscopic measurements of the equivalence ratio

As shown in Figure A.3, gases metered using rotometers are mixed in a cross flow arrangement before traveling 0.5 m through a 25 mm ID tube. A fine mesh honeycomb stabilizes a premixed flame over the burner during measurements in combustible mixtures.

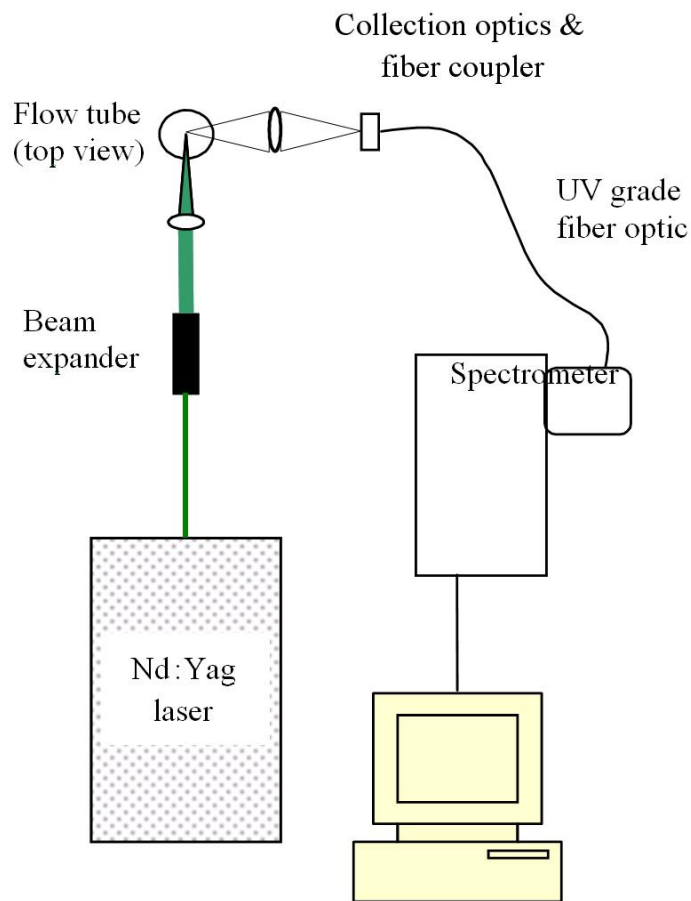


Figure A.3: *Setup for gas composition measurements.*

The air flow was set at 10 l/min for all of the experiments, while fuel, diluent

CO₂, or He were varied to set the mixture fraction. A curtain flow of argon surrounds the premixed stream to stabilize the flow. 10 Hz pulses of 1064 nm light from a Spectra Physics Quanta Ray Pro 230, Q-switched Nd:Yag laser were used to generate the plasma. The beam is focused using a 12.5 cm focal length fused silica convex lens. The breakdown takes place approximately 2 mm above the center of a 25 mm ID tube. A pair of 12.5 cm focal length fused silica lens collects and collimates the emission at right angles to the laser beam, and couples the plasma light into a UV-grade optical fiber. The fiber transmits the light to a 0.3-m Acton SpectraPro 300i spectrometer, where the signal is spectrally resolved and imaged onto a Roper Scientific PI-Max gated ICCD camera. The effective dispersion of the system with the 600 groove-mm grating employed in these measurements is approximately 0.125 nm/pixel. The ICCD camera is fully binned in the vertical (non-dispersion) direction. The system is coupled to a personal computer for data acquisition. The laser pulse energy was measured with an Ophir pyroelectric energy meter, controlled by personal computer and capable of recording measurements at the laser repetition rate of 10 Hz.

A.4 Engine experiments

As shown in Figure A.4, the test engine is a General Motors LD-9 dual overhead cam four-cylinder engine. This engine, originally known as the GM Quad 4, has four valves per cylinder, a direct-fire ignition system, and port fuel injection. In this investigation, the ignition and fuel injection are controlled with an Intelligent Controls IC 5460 computer controller, which directly controls the fuel injectors and sends low-level ignition signals to an Intelligent Controls IC 5580 ignition relay system to fire the ignition coils.

A Borghi and Saveri FE-300-S eddy current dynamometer loads the engine, under control of a SuperFlow Pro Console test system, which also acquires engine performance data. The measured performance data included speed, torque, relative intake air flow, exhaust sample temperature and a reference equivalence ratio. A number of other standard temperatures and pressures are recorded.

The reference fuel to air ratio is measured using an ECM 2400G UEGO-based Wide-Range Air-Fuel Ratio Analyzer. A hot-wire mass-air-flow sensor output provides the relative mass air-flow measurement. An optical cell was mounted on the exhaust manifold, roughly 15 cm from the exhaust valve of one of the cylinder. The cell consists of two fused silica windows, 50 mm in diameter and 12 mm thick, mounted at right angles on a cubic steel frame. The 532 nm pulse from a CFR 400 Big Sky Nd:YAG laser was used to generate the plasma. The beam is focused using a 12.5 cm focal length fused silica convex lens. The breakdown takes place approximately in the center of the optical cell. A triggering signal from the engine

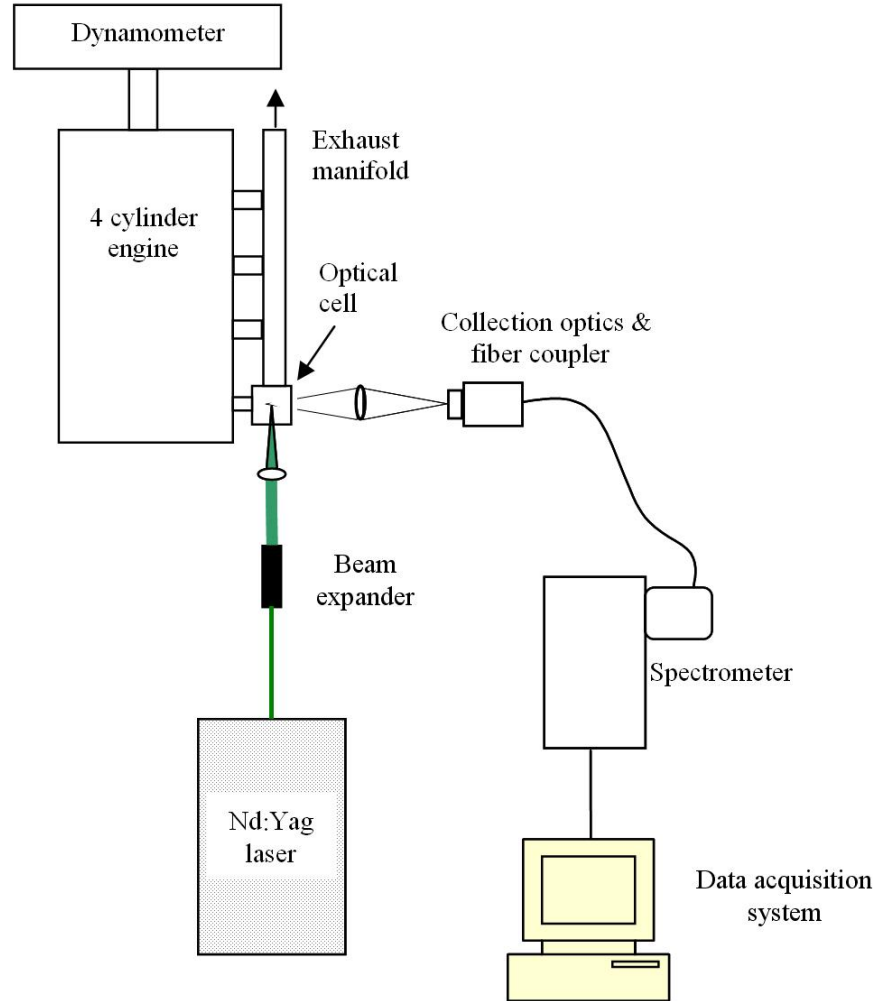


Figure A.4: *Setup for measurements on the engine.*

is used to synchronize the laser so that every measurement is taken in a specified position during the engine cycle. For simplicity the speed of the engine was regulated to provide a signal close to 10 Hz, the default laser repetition rate set by the manufacturer. A 12.5 cm focal length fused silica lens collects and collimates the emission at right angles to the laser beam, and couples the plasma light into a UV-grade optical fiber. The fiber transmits the light to a 0.3-m Acton SpectraPro 300i spectrometer, where the signal is spectrally resolved and imaged onto a Roper

Scientific PI-Max gated ICCD camera. The effective dispersion of the system with the 600 groove-mm grating employed in these measurements is approximately 0.125 nm / pixel. The camera is controlled by a triggering signal from the laser Q-switch. The ICCD is fully binned in the vertical (non-dispersion) direction.

Bibliography

- [1] L.J. Radziemski: *Microchem. J.*, Vol 50 pp. 218, 1994.
- [2] I. Schechter: *Rev. Anal. Chem.*, Vol 16 (3), pp. 173, 1997.
- [3] K. Song, Y.-I. Lee and J. Sneddon: *Appl. Spect. Rev.*, Vol 32 (3), pp. 183, 1997.
- [4] J. Sneddon and Y.-I. Lee:
- [5] R. Dibble, A. Masri and R. Bilger: *Comb. Flame*, Vol 67, pp. 189, 1987.
- [6] M. Schutte, H. Finke, G. Grunfeld, S. Kruger, P. Andresen, B. Stiebels, B. Block, H. Meyer and W. Hentschel: *SAE Transactions, Journal of Fuels and Lubricants*, Vol 109, pp. 942, 2000.
- [7] S. Einecke, C. Schultz and V. Sick; *Appl. Phys. B.*, Vol 71, pp. 717, 2000.
- [8] K. Kohse-Hoeinghaus and J.B. Jeffries: *Applied Combustion Diagnostics*, 2002.
Anal. Lett., Vol. 32 (11), pp. 2143, 1999.
- [9] D. W. Hahn, W. L. Flower, K. R. Hencken: *Appl. Spectrosc.*, Vol 51, pp. 1836, 1997.

- [10] B. Fisher, H. Johnsen, S. G. Buckley, D. Hahn: *Appl. Spectrosc.*, Vol 55, pp. 1312, 2001.
- [11] S. G. Buckley: *Env. Eng Sci.*, Vol. 22 (2), pp. 195, 2005.
- [12] T.X. Phuoc and F.P. White: *Fuel*, Vol 81, pp. 1761, 2002.
- [13] V. Sturm and R. Noll: *Appl. Opt.*, Vol 42. (30), pp. 6221, 2003.
- [14] L. J. Radziemski, D. A. Cremers: *Laser-Induced Plasmas and Applications*, Marcel Dekker, 1989.
- [15] Yu. P. Razier: *Laser Induced Discharge Phenomena*, Consultants Bureau, New York, 1977.
- [16] D. C. Smith, R. G. Meyerand: in *Principles of Laser Plasmas*, Wiley, 1976.
- [17] C. Grey-Morgan: *Rep. Prog. Phys.*, Vol 38, pp. 621, 1975.
- [18] J. F. Ready: *Effects of High-Power Laser Radiation*, Academic Press, 1971.
- [19] Yu. P. Razier: *Soviet Phys JETP*, Vol. 48, pp. 1508, 1965.
- [20] Ya. B. Zel'dovich, Yu. P. Razier: *Physics of Shock Waves and High Temperature Hydrodynamic Phenomena*, Dover Publications, 2002.
- [21] R. G. Root, A. N. Pirri. P. K. S. Wu, H. Gelman: *Phisycal Science Inc. Rep. PSI TR-170*, 1979
- [22] N. H. Kemp, R. G. Root: *J. Energy*, Vol 3, pp. 40, 1979.

- [23] R. G. Root, A. N. Pirri: AIAA paper 79-1489, 1979.
- [24] R. G. Root, A. N. Pirri, P. K. S. Wu: AIAA J., Vol 16, pp. 1296, 1978.
- [25] V. I. Bergel'son, T. V. Losera, I. V. Nemchinov, T. I. Orlova:
Sov. J. Plasma. Phys. , Vol 1, pp. 498, 1975.
- [26] A. N. Pirri: Phys. Fluid. , Vol 16, pp. 1435, 1972.
- [27] P. D. Thomas: AIAA J. , Vol 15, pp. 1405, 1977.
- [28] E. K. Dabora: AIAA J. , Vol 10, pp. 1384, 1972.
- [29] N. Ferriter, D. E. Maiden, A. M. Wilson, J. A. Fleck: AIAA J., Vol 15, pp. 1597,
1977.
- [30] G.I. Taylor: Proc. Roy. Soc. (London), Ser. A 201, pp. 175, 1950.
- [31] L. I. Sedov: *Similarity and Dimensional Methods in Mechanics*, Academic
Press, 1959.
- [32] Y., L. Chen, J. W. L. Lewis, C. Parriger: J. Quant. Spectrosc. Radiat. Transfer,
Vol. 67, pp. 91, 1998.
- [33] C. V. Bindhu, S. S. Harilal, M. S. Tillack, F. Najamabadi, A. C. Gaeris: Appl.
Spectrosc., Vol. 58-6, pp. 719, 2004.
- [34] C. V. Bindhu, S. S. Harilal, M. S. Tillack, F. Najamabadi, A. C. Gaeris: J.
Appl. Phys., Vol. 94-12, pp. 7402, 2003.

- [35] G. W. Bluman, S. Kumeni: *Symmetries and Differential Equations (Applied Mathematical Sciences, Vol 81)*, Springer, 1989.
- [36] M. Born, E. Wolf: *Principles of Optics*, Pergamon Press, 1986.
- [37] U. S. Departement of Defense: *The Effects of Atomic Weapons*, McGraw-Hill, 1950.
- [38] G. Birkhoff: *Hydrodynamics: a Study in Logic, Fact and Similitude*, University Press, 1950.
- [39] G. I. Barenblatt: *Similarity, Self-Similarity and Intermediate Asymptotics*, Consultants Bureau, 1979.
- [40] E. S. Taylor: *Dimensional Analysis for Engineers*, Clarendon Press, 1974.
- [41] V. Kurdyumov, A. L. Sánchez, A. Liñán: *J. Fluid mech.*, Vol. 419, pp. 379, 2003.
- [42] H. H. Goldstine, J. Von Neumann: *Comm. on Pure and Appl. Math*, Vol. 8, pp. 327, 1955.
- [43] M. Gatti, V. Palleschi, A. Salvetti, D. P. Singh, M. Vaselli: *Opt. Comm.*, Vol. 69, pp. 141, 1988.
- [44] M. A. Harith, V. Palleschi, A. Salvetti, D. P. Singh, G. Tropiano, M. Vaselli: *Opt. Comm.*, Vol. 71, pp. 76, 1989.
- [45] H. Stein, W. Gretler: *Phys. Fluids*, Vol. 6-6, pp. 2154, 1994.

- [46] I. G. Dors, C. G. Parriger: *Appl. Optics*, Vol. 42-30, pp. 5978, 2003.
- [47] V. P. Korobeinikov, N. S. Mel'nikova, Ye. V. Ryazanov: *Theory of Point Explosion*, U.S. Department of Commerce, office of Technical Services, 1962.
- [48] U. Panne, C. Haisch, M. Clara and R. Niessner: *Spectrochim. Acta*, Part B, Vol 53, pp. 1957, 1998.
- [49] U. Panne, C. Haisch, M. Clara and R. Niessner: *Spectrochim. Acta*, Part B, Vol 53, pp. 1969, 1998.
- [50] L. D. Landau: *Sov. J. Phys.*, Vol 9, pp. 496, 1945.
- [51] D. Ye. Okhotsimskii, Z. P. Vlasova: *Zh. vych. mat.*, Vol 2 (1), pp. 107, 1962.
- [52] O. Barthélemy, J. Margot, S. Laville, F. Vidal, M. Chaker, B. Le Dragoff, T. W. Johnston, M. Sabsabi: *Appl. Spectrosc.*, Vol. 59 (1), pp. 529, 2005.
- [53] H. R. Griem: *Principles of Plasma Spectroscopy*, Cambridge Univ. Press, 1997.
- [54] W. Demtröder: *Laser Spectroscopy*, Springer-verlag, 2002.
- [55] D. V. Fisher, Y. Maron: *Eur. Phys. J. D.*, Vol 14, pp. 349, 2001.
- [56] *NIST online Database of Atomic Spectra*
http://physics.nist.gov/cgi-bin/AtData/main_asd. Last referenced
18/06/2005.
- [57] I. B. Gornushkin, J. M. Anzano, L. A. King, B. W. Smith, N. Omenetto, J. D. Winefordner: *Spectrochimica Acta B*, Vol 54, pp. 491 1999.

- [58] I. B. Gornushkin, L. A. King, B. W. Smith, N. Omenetto, J. D. Winefordner: *Spectrochimica Acta B*, Vol 54, pp. 1207, 1999.
- [59] I. B. Gornushkin, C. L. Stevenson, B. W. Smith, N. Omenetto, J. D. Winefordner: *Spectrochimica Acta B*. Vol 56, pp. 1769, 2001.
- [60] C. Aragón, J. Bengoechea, J. A. Aguilera: *Spectrochimica Acta B*, Vol 56, pp. 619, 2001.
- [61] J.E. Carranza, D.W. Hahn: *Spectrochim. Acta, Part B.*, Vol 57, pp. 779, 2002.
- [62] F. Ferioli, P. V. Puzinauskas and S. G. Buckley: *Appl. Spectrosc.*, Vol 57 (9), pp. 1183, 2003.
- [63] S.D. Brown: *Appl. Spectrosc.*, Vol. 49, 14A, 1995.
- [64] R. de Bruijn, K. Koshelev, F. Bijkerk: *J. Phys. D: Appl. Phys.*, Vol 36, pp. L88, 2003.
- [65] D. R. Kania, L. S. Pan, P. Bell, O. L. Laden, H. Kornblum, P. Pianetta: *J. Appl. Phys.*, Vol 68 (1), pp. 124, 1990.
- [66] W. C. Hinds: *Aerosol Technology : Properties, Behavior, and Measurement of Airborne Particles*, Wiley-Interscience, 1998.
- [67] O. A. Ezekoye, Y. W. Wibowo: *J. of Aerosol Sci.*, Vol. 30, pp. 1117, 1999.
- [68] A. Goldshtein, K. Shuster, P. Vainshtein, M. Fichman, C. Gutfinger: *J. Fluid Mech*, Vol 360, pp. 1, 1998.

- [69] K. Shuster, M. Fichman, A. Goldshtein, C. Gutfinger: *Phys. Fluids*, Vol 14 (5), pp. 1802, 2002.
- [70] S. Temkin, *Phys. Fluids*: Vol 13, pp 1639, 1970.
- [71] S. Temkin, *Phys. Fluids*: Vol 6, pp. 2294, 1994.
- [72] J. J. Strecker, P. Roth: *J. Aerosol Sci*, Vol 20 (8), pp. 1035, 1989.
- [73] S. Temkin, S. S. Kim: *J. Fluid Mech*, Vol 96, pp 133, 1980.
- [74] S. Temkin, G. Ecker: *J. Fluid Mech*, Vol 202, pp. 467, 1989.
- [75] R. Vanderwood, C. Cetinkaya: *J. Adesh. Sci. Technol*, Vol 17 (1), pp. 91, 2003.
- [76] R. Vanderwood, C. Cetinkaya, M. Rowell: *J. Adesh. Sci. Technol*, Vol 16 (9), pp. 1201, 2002.
- [77] C. Crowe, M. Sommerfeld, Y. Tsuji: *Multiphase Flows with Droplets and Particles*, CRC Press, 1998.
- [78] S. K. Friedlander: *Smoke, Dust and Haze*, Oxford University Press, 2000.